STATISTICAL PHYSICS OF BULK AND CONFINED IONIC LIQUIDS

Alpha Albert Lee

St Catherine's College

A thesis submitted to the University of Oxford
for the degree of Doctorate of Philosophy

June 2015

PREFACE

The research described in this thesis was performed in the Mathematical Institute, University of Oxford between October 2013 and June 2015 and was supervised by Professor Alain Goriely and Dr Dominic Vella. No part of this thesis has been submitted for any qualification other than for the degree of Doctor of Philosophy at the University of Oxford.

I have benefited from fruitful discussions with Dr Susan Perkin of University of Oxford about the physical chemistry of ionic liquids, Dr Svyatoslav Kondrat of Forschungszentrum Jülich about nanoporous supercapacitors and electrokinetics, and Professor John Wettlaufer about non-equilibrium Casimir effects. The numerical minimisation of the mean-field free energy described in Section 5.3 was performed jointly by myself and Dr Kondrat, and Dr Kondrat performed the Monte Carlo simulations in Section 5.3. I am responsible all other original work reported in this thesis.

The work described in this thesis is believed to be original, except where reference is made to the work of others. In particular, the results of Chapter 2 constitute review material.

Oxford, June 2015

ACKNOWLEDGEMENTS

I would like to express my deep gratitude to Professor Alain Goriely and Dr Dominic Vella, my supervisors, for their mentorship, advice, and nuggets of wisdom. Over the last two years, they have encouraged me to develop my own DPhil project and research direction, and supported me to work on a project this is not directly related their main research focus. I am eternally grateful for their support on this journey (and bravery for taking on a chemistry graduate!).

Deep thanks to Dr Susan Perkin for motivating me to work on confined ionic liquids. My work have benefited tremendously from Susan's insights in the chemical physics of ionic liquids. The meticulous experiments performed by her group formed the basis of my theoretical study.

I am very fortunate to have the help and mentorship of various people during my DPhil: I would like to thank Professor John Wettlaufer for our discussions about statistical physics and Casimir forces. The work on non-equilibrium Casimir forces was done in collaboration with him. Dr Svyatoslav Kondrat performed Monte Carlo simulation for charge storage in nanoporous supercapacitors, and critically read my derivation of the continuum electrokinetic equations.

Special thanks to Professor Daan Frenkel — his course at the Park City Mathematical Institute on "Entropy, Probability and Packing" is the most inspiring course I have had on statistical physics. I am especially grateful for the opportunity to work with him to compile the lecture notes for that course.

I owe a deep debt of gratitude to my mentors down memory lane. Many thanks to Dr Poh, my teacher at secondary school; Professor Craig, my mentor and tutor at Imperial College; and Professor Hore, who taught me how to do theoretical research in chemistry.

The financial support from the Engineering and Physical Sciences Research Council and St Catherine's College, Oxford is gratefully acknowledged.

On a personal note, deep thanks to all my friends for their support and companion over the years: you all know who you are!! You made my life in Oxford enjoyable.

Last but certainly not the least, I thank my parents for their unending love.

ABSTRACT

Room temperature ionic liquids are molten salts at ambient temperature. This thesis is concerned with the structure of room temperature ionic liquids both in the bulk and in confinement. A particular theme is the rich statistical physics of such systems, which is primarily due to strong Coulomb correlations.

We begin by examining the structure of ionic liquids in the bulk. One of the most important questions in understanding the structure of ionic liquids is whether ions are truly "free" and mobile (a concentrated ionic solution), or are rather bundled up as ion pairs (a dilute solution of free ions dissolved in a sea of ion pairs). We propose a mathematical model for the thermodynamics and kinetics of ion pairing in ionic liquids. Our model reveals that roughly 2/3 of ions are free, whilst those ion pairs that do exist are short-lived. We conclude that ionic liquids ought to be considered to be concentrated, rather than dilute, electrolytes.

We then examine the structure of ionic liquids confined between charged surfaces. Motivated by surface force balance experiments, we use a 1D Coulomb gas model to study ionic liquids confined between charged mica surfaces. We show that the disjoining pressure–surface separation curve depends on the fugacity (the bulk cohesive energy) of the ionic liquid, and the electrostatic interaction energy of ions at closest approach. The model shows good qualitative agreement with experimental data, with all parameters independently estimated without fitting.

We then turn our attention to a single layer of ionic liquid ions confined between metal surfaces, and develop a mean field model for equilibrium charge storage in a nanoporous supercapacitor. The development of nanoporous supercapacitors is hindered by the perceived tradeoff between capacitance, power delivery and reversible charging — a trilemma. Our model identifies the affinity of ions to the pore wall as a key parameter that controls charging behaviour. From this, we elucidate a region of "ionophilicity" in which the capacitance-power-hysteresis trilemma can be avoided.

The non-equilibrium physics of ion transport in ionic liquids is then considered. We derive a novel system of continuum electrokinetic equations for ionic liquids that is based

on coarse graining a simple exclusion process defined on a lattice. The resulting dynamical equations are written as a gradient flow with a degenerate mobility function. This form of the mobility function gives rise to novel charging behaviours that are qualitatively different to those known in electrolytic solutions.

Finally, we consider active non-equilibrium fluids, in which energy is continuously consumed from the surrounding environment. Those systems are inherently far from thermodynamic equilibrium. By developing a top-down description for non-equilibrium systems with the fluctuation spectrum as the central quantity, we show that the form of the disjoining force may reveal crucial elements of the microscopic physics. Our framework explains the long-ranged force observed in recent molecular dynamics simulation of active Brownian particles.

Contents

Chapter 1

Introduction

> Science may be described as the art of systematic oversimplification.
>
> *(Karl Popper)*

1.1 Motivation

Common experience suggests that ionic salts usually exist in a solid, crystalline state at room temperature. Coulomb interactions between ions are strong (much larger than the thermal energy $k_B T$) and long ranged, making the melting temperature of even monovalent salts far above room temperature (*e.g.* table salt melts at 801 °C).

However, careful consideration of the thermodynamics of melting suggests that the well-ordered crystalline lattice could be disrupted by geometrically anisotropic ions. Similarly, the strong Coulomb interactions might be weakened if the ions are large and polarisable. Being large means that the surface charge density is low and also that the electrostatic interaction energy at closest approach is relatively small. Molecular polarisability provides another mechanism to screen out electrostatic interactions (Krossing et al., 2006). Clearly, these complications do not apply to an atomic salt, which is therefore likely to be solid at room temperature. However, molecular salts, for which the cations and anions are typically large organic molecules can, because of these complications, be liquid at room temperature (see Figure 1.1 for a comparison between ionic liquids and atomic salts).

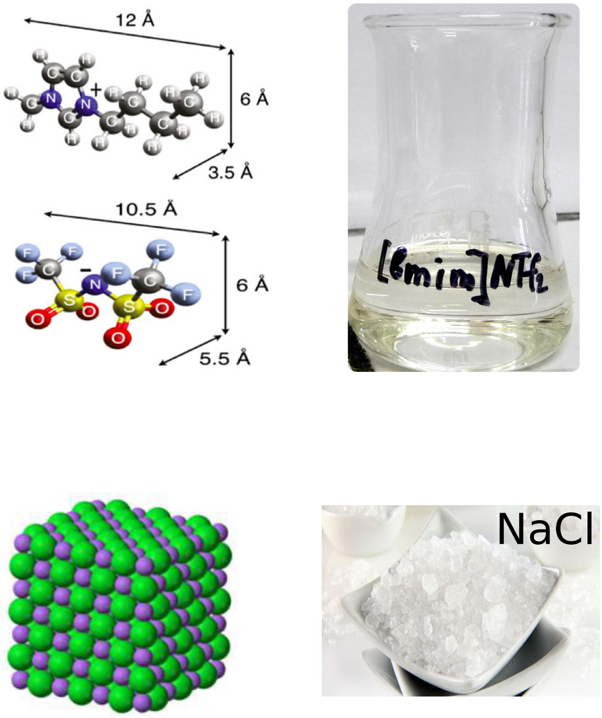

Figure 1.1: *At room temperature, table salt is a solid whilst the ionic liquid* [BMIm][NTf$_2$] *is a liquid. The ions that make up ionic liquids are large and asymmetric — smearing out the charge of the ion and preventing it from readily crystallising into a lattice. The figures are taken from: Top left: (Gebbie et al., 2013a); Top right: (Wikipedia, 2014); Bottom left: (Guardian, 2014); Bottom right: (about.com, 2014).*

As early as 1914, the ionic compound ethylammonium nitrate was discovered to be a liquid at room temperature (Walden, 1914). Largely forgotten in the literature until the 1990s, ionic liquids now find themselves at the centre of many modern chemical and technological applications. Ionic liquids are non-volatile, and generally non-toxic and chemically inert. By virtue of being charged yet relatively aliphatic (hydrocarbon-like) and lipophilic (oil-loving), ionic liquids can dissolve a wide range of organic and inorganic materials. This property makes them the ideal solvents for many "green" chemical processes (Welton, 1999; Hallett and Welton, 2011). Industrially, ionic liquids are currently being explored as solvents for dissolving cellulose (Wang et al., 2012) and capturing carbon dioxide (Zhang et al., 2012). The solvation properties of ionic liquids lead to a natural question: are the ions in ionic liquids truly "free" and mobile, or rather "bound" in ion pairs (a dilute solution of free ions dissolved in ion pairs)? Are ionic liquids analogous to polar solvents?

Not only are ionic liquids excellent solvents for chemical synthesis, they are also good electrolytes that can withstand a large potential difference without being chemically oxidised or reduced. Whilst water has a electrochemical stability window of 1.2 V (Wessells et al., 2010), ionic liquids have a much wider stability window of 2-3 V, and some can even withstand up to 5-6 V (Ohno, 2011). This property renders them attractive candidate electrolytes for applications in which a large potential difference is applied. In particular, capacitors with ionic liquids as electrolytes have received significant attention due to their potential ability to bridge the gap between battery and dielectric capacitors. Conventional batteries have large energy densities but suffer from slow power delivery, whilst conventional dielectric capacitors enjoy fast power delivery but have small energy densities. Ionic liquid-based capacitors have been experimentally shown to enjoy the best of both worlds, and therefore offer the potential to be a versatile circuit element.

Following the success of ionic liquid capacitors, field-effect transistors with ionic liquids as gate dielectrics are currently under development (Fujimoto and Awaga, 2013). In field-effect transistors, large electric fields are needed near the semiconductor interface to control the conductivity, which is paramount to transistance (Ueno et al., 2008). It is difficult to create large electric fields in conventional dielectrics as the electric field is only inversely proportional to the separation between the electrodes (see Figure 1.2). However, if ionic liquids are used as the electrolyte, the ions concentrate themselves near the oppositely charged semiconductor interface. The semiconductor-ionic liquid interface now acts effectively as a parallel plate capacitor, with one plate being the semiconductor and the other being the layer of ionic liquid counterions (see Figure 1.2). As a result, the large capacitance means that a large electric field is created near the semiconductor surface (Ueno et al., 2008).

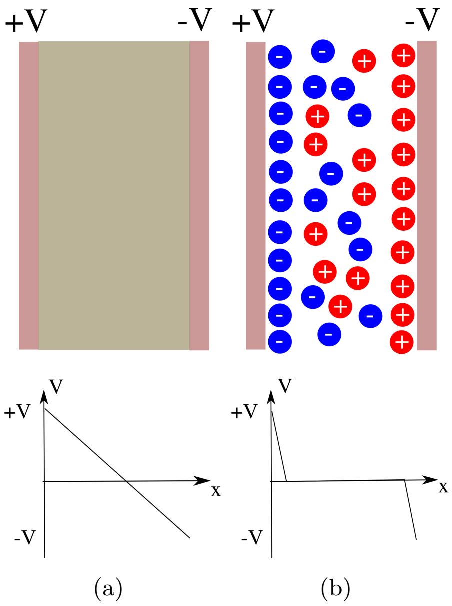

Figure 1.2: *(a) In a conventional dielectric material, the electric field is inversely proportional to the electrode separation as the voltage drop is linear. (b) Ionic liquids ions are attracted to oppositely charged surfaces to compensate the electrode surface charge. This arrangement of ions screens the electric field, and so the potential drop occurs over the molecular scale. Therefore the interfacial electrical capacitance is large, and a large electric field is created near the interface.*

Despite experimental advances, many important questions that underpin further development of nanotechnological devices based on ionic liquids near electrified interfaces remain open: What is the structure of ions near a charged interface? How do we optimise charge storage in ionic liquid capacitors? What determines the kinetics of charge storage and power delivery?

Ionic liquids are also attractive candidates as novel lubricants (Minami, 2009; Bermúdez et al., 2009). The chemical resilience of ionic liquids (*e.g.* low chemical reactivity) means that, compared to conventional synthetic oils, they are able to safely withstand the elevated temperatures and pressures associated with high friction (Minami et al., 2007). Another significant advantage of ionic liquids is the large variety of anions and cations that can be used: the chemistry of ionic liquid synthesis makes it easy to "mix-and-match" cations and anions. This property means that ionic liquids may be tuned for a particular application, with the cations and anions playing their own roles. For example, the hexaflurophosphate (PF_6) anion adsorbs to steel surfaces to form a protective film, whereas the hydrocarbon alkyl chains attached to the imadizolium cation provide smooth sliding properties because the polymer-like chains are flexible (Qu et al., 2009).

At the nanoscale, confined ionic liquids display a very rich tribological response. Recently the Perkin group (Perkin et al., 2010; Smith et al., 2013) has shown that ionic liquids

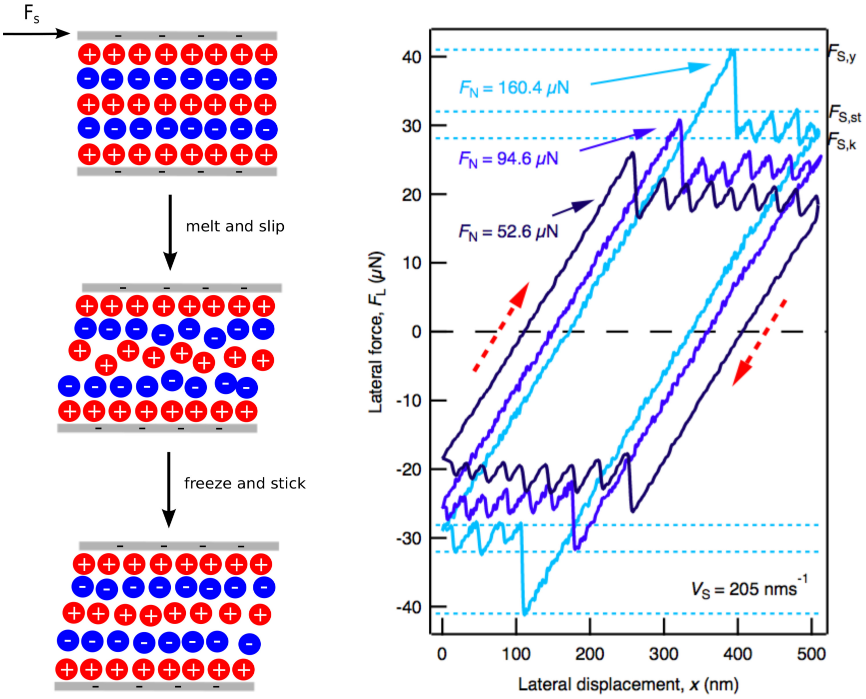

Figure 1.3: *Stick slip due to shear induced melting. The left panel shows a cartoon of the proposed mechanism. The right panel shows experimental data from Smith et al. (2013), where the ionic liquid* [BMIm][NTf$_2$] *is used and the normal force applied is* $160.4\ \mu N$*. We note that there are 7 layers of ions confined between the mica surface in the experiment — for visual clarity the schematic sketch only shows 5 layers.*

confined between negatively charged mica surfaces display interesting stick-slip behaviour, with the friction coefficient increasing as the mica-mica separation decreases. Thus the important question is: how do ions arrange themselves when an ionic liquid is strongly geometrically confined by charged surfaces? Do ions arrange themselves in a regular manner near a charged interface with alternating layers of counterions and co-ions?

This thesis is concerned with providing a framework for answering the important question discussed above. We tackle those question by considering a number of physically instructive model problems.

1.2 Structure of the Thesis

In this thesis we study the statistical physics of ionic liquids in bulk and in nanoconfinement. We study a collection of problems in this area, focusing particularly on the role of long-ranged Coulomb interactions.

Chapter 2 reviews the statistical field theory of ions near charged interfaces. This study allows us to derive rigorously the oft-used Poisson-Boltzmann theory as the mean-field, saddle point approximation of an exact path integral. By solving the Poisson-Boltzmann equation in simple geometries and comparing with recent experiments, we demonstrate how and why the Poisson-Boltzmann theory often fails spectacularly when applied to ionic liquids.

Chapter 3 is devoted to understanding the bulk structure of ionic liquids. Going beyond the Poisson-Boltzmann picture, we introduce explicit ion-pairs into the model, and ask the question: are ions in ionic liquids truly free, or are they bundled up as dipolar ion pairs? By considering the association equilibrium between free ions and ion pairs, we show that roughly 2/3 of ions are free, and those ion pairs that do exist have lifetimes of the same order of magnitude as the timescale for translational diffusion. Thus ionic liquids must be considered to be concentrated electrolytes. This analysis clarifies a major controversy in the recent literature about the interpretation of surface force balance data, and suggest a physical model for predicting the dielectric constant of ionic liquids.

In Chapter 4 we develop a statistical mechanical model to understand the disjoining pressure required to confine ionic liquids between charged mica surfaces. Recent measurements using surface force balances show that the disjoining pressure is an oscillatory function of surface separation. By considering a 1D Coulomb gas model with excluded volume, we are able to qualitatively interpret the experimental data. The match between model and experiments confirms that ionic liquids arrange themselves in a regular manner near a charged interface with alternating layers of counterions and co-ions. In addition, our model highlights the importance of two dimensionless parameters: the fugacity (*i.e.* the bulk cohesive energy) of the ionic liquid, and the electrostatic interaction energy of ions at closest approach, in determining how the disjoining pressure exerted on the walls depends on the geometrical confinement. This reveals that the thermodynamics of ionic liquids in geometric confinement is intimately coupled to the thermodynamics of bulk ionic liquids.

Chapter 5 focuses on the more practical question of energy storage using confined ionic liquids. Seminal experiments by Chmiola et al. (2006) show that significant capacitance can be achieved by using nanoporous electrodes with pore size of the same order of magnitude as the ion size. Subsequent theories and experiments suggest that: (1) Capacitance increases as the pore width decreases (Lin et al., 2009); (2) Charging is slower when the pore size decreases (Kondrat and Kornyshev, 2013; Kondrat et al., 2014); and (3) Charge storage proceeds via a first order adsorption phase transition (Kiyohara et al., 2011; Kondrat and Kornyshev, 2011; Kiyohara et al., 2012). Thus, at first sight, there is a trilemma between optimising capacitance and power delivery whilst avoiding hysteresis. We challenge this view of a ‘trilemma’ by developing a mean-field model for a confined 2D layer of ionic liquid ions that takes into account the modification of the Coulomb interaction potential due to electrons from the metallic electrodes, as well as the entropy of packing ions. The model reveals that the thermodynamics of bulk ionic liquids, as well as ion-pore van der Waals interactions, are important parameters in determining the charge storage properties. In particular, we identify a parameter regime in which the capacitance-power-hysteresis trilemma can be resolved.

Having explored the equilibrium properties of bulk and confined ionic liquids, the remainder of the thesis concerns the non-equilibrium response of strongly-correlated liquids. Previous theoretical approaches for ion transport in an ionic liquid treats steric interactions as a perturbation of the dynamics. While this assumption is reasonable for dilute systems such as an electrolyte solution or colloid suspension, this physical picture is not valid for ionic liquids (since in Chapter 3 we showed that ionic liquids are concentrated ionic melts). In Chapter 6, we develop a model for electrokinetic transport by systematically coarse-graining a simple exclusion process defined on a lattice. The resulting dynamical equations can be written as a gradient flow with a degenerate mobility function. This form of the mobility function gives rise to charging behaviours that are qualitatively different to the ones known in electrolytic solutions, and importantly the accumulated charge in the double layer is no longer a monotonic function of time. The predictions of our model is consistent with the results of recent simulations.

Chapter 7 generalises the scope of our work to treat another class of non-equilibrium systems: *active* fluids. The defining feature of active fluids is that they continuously consume energy from the surrounding environment and thus are far from thermodynamic equilibrium, even in steady state. The recent simulations performed by Ni et al. (2015) showed that the disjoining pressure between hard walls immersed in a bath of active Brownian particles shows oscillations that indicate a large degree of correlation and structure. Following the intuition underpinning Chapter 4, we use the disjoining pressure as a tool to probe the physics underlying the system. However, unlike ionic liquids, the system can no longer be described using equilibrium statistical mechanics. Instead, we develop a universal framework for non-equilibrium systems using the fluctuation spectra as the fundamental quantity. Our framework affords us a top-down view of non-equilibrium systems, and compares well with the simulations by Ni et al. (2015).

Finally, in Chapter 8, we summarise our findings and discuss some avenues for future research in this area. We identify several key experiments and simulations that could be peformed to verify our theoretical findings.

Chapter 2

Statistical Physics of Ions Near Charged Interfaces

Synopsis

The classical mean-field Poisson-Boltzmann theory is often used as a theoretical tool to model electrolytes and ionic liquids near charged interfaces. In this Chapter, we review the field theoretic treatment of Coulombic systems. From statistical field theory, we can derive the Poisson-Boltzmann theory as the saddle point approximation of the full path integral. This derivation illustrates the range of validity, as well as the pitfalls, of the Poisson-Boltzmann theory, and motivates the model problems that will be considered in subsequent Chapters.

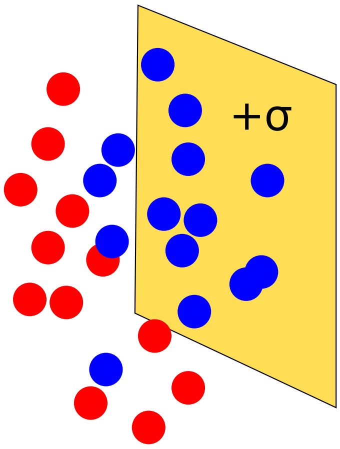

Figure 2.1: *Schematic sketch of the system: Cations (red) and anions (blue) near a surface of charge density σ.*

2.1 Field Theoretical Derivation

A key problem that underpins nanotechological applications of ionic liquids is understanding the structure and thermodynamics of ions near a charged surface. Whilst the statistical thermodynamics of a weakly interacting gas is well developed, the physics of strongly interacting systems is relatively poorly understood. The Coulomb interactions between ions are strong and long–ranged: the interaction energy at contact between typical ionic liquid ions (monovalent ions with a diameter of 10nm in a medium of dielectric constant $\epsilon = 2$) is 28 $k_B T$, and the interaction only decays inversely with separation.

To understand the behaviour of ions near a charged surface, we follow the derivation presented by Netz and Orland (2003) to obtain the exact partition function as a path integral. This approach will enable us to derive the most common simplification known as the Poisson-Boltzmann equation. Consider N_+ cations and N_- anions, both monovalent, interacting with an arbitrary charge distribution $\sigma(\mathbf{r})$ (see Figure 2.1 for a schematic illustration of the problem). Introducing the ion density operator

$$\hat{\rho}_\pm = \sum_{j=1}^{N_\pm} \delta(\mathbf{r} - \mathbf{r}_j^\pm), \tag{2.1}$$

where $\mathbf{r}_j^\pm$ denotes the position of the j^{th} cation/anion, we can write the partition function in the canonical ensemble as

$$
\begin{aligned}
Z_{N_+,N_-} &= \frac{\exp\left[\frac{l_B}{2}(N_+ + N_-)v(0)\right]}{N_+!N_-!}\int\prod_{j=1}^{N_+}\frac{\mathrm{d}\mathbf{r}_j^+}{\lambda_T^3}\int\prod_{j=1}^{N_-}\frac{\mathrm{d}\mathbf{r}_j^-}{\lambda_T^3} \\
&\quad \exp\left\{-\frac{l_B}{2}\int\mathrm{d}\mathbf{r}\int\mathrm{d}\mathbf{r}'[\hat{\rho}_+(\mathbf{r})-\hat{\rho}_-(\mathbf{r})-\sigma(\mathbf{r})]v(\mathbf{r}-\mathbf{r}')[\hat{\rho}_+(\mathbf{r}')-\hat{\rho}_-(\mathbf{r}')-\sigma(\mathbf{r}')]\right\},
\end{aligned}
\tag{2.2}
$$

where $v(\mathbf{r}-\mathbf{r}') = 1/|\mathbf{r}-\mathbf{r}'|$ is the Coulomb interaction kernel, $l_B = q^2/(\epsilon k_B T)$ is the Bjerrum length, λ_T is the thermal wavelength (due to integrating over the momentum degrees of freedom), and the second factor in the exponential, $l_B v(0)/2$, is the self-energy term. The Bjerrum length is the separation at which the Coulomb interaction between two charges equals the thermal energy scale $k_B T$, and is an important lengthscale in the physics of ionic liquids. Note that the self-energy $v(0)$ is formally divergent; however, the statistical physics of the system is invariant to a constant multiplicative factor of the path integral and as such we can subsume it into the fugacity as shown below (physically, the root of a divergent term in the path integral is due to the fact that we ignored excluded volume interactions, which we will discuss below). The density operators, $\hat{\rho}_\pm$, are difficult to manipulate. It is convenient to rewrite the partition function in terms of a functional integral over a continuous density field ρ. To do this, we introduce the functional delta distribution,

$$
\begin{aligned}
Z_{N_+,N_-} &= \frac{A}{N_+!N_-!}\int\mathfrak{D}\rho_+\mathfrak{D}\rho_-\int\prod_{j=1}^{N_+}\frac{\mathrm{d}\mathbf{r}_j^+}{\lambda_T^3}\int\prod_{j=1}^{N_-}\frac{\mathrm{d}\mathbf{r}_j^-}{\lambda_T^3} \\
&\quad \exp\left\{-\frac{l_B}{2}\int\mathrm{d}\mathbf{r}\int\mathrm{d}\mathbf{r}'[\rho_+(\mathbf{r})-\rho_-(\mathbf{r})-\sigma(\mathbf{r})]v(\mathbf{r}-\mathbf{r}')\right. \\
&\quad \left.[\rho_+(\mathbf{r}')-\rho_-(\mathbf{r}')-\sigma(\mathbf{r}')]\right\}\delta[\rho_+-\hat{\rho}_+]\delta[\rho_--\hat{\rho}_-],
\end{aligned}
\tag{2.3}
$$

where we have subsumed the self-energy term into the constant A, and $\int\mathfrak{D}$ denotes a functional integral. The functional integral is a generalisation of the Riemann integral. Rather then summing a function, $f(x)$, over a continuous range of values of x, the notation $\int G[f]\,\mathfrak{D}f$ denotes the sum of a functional, $G[f]$, over all possible functions f in a function space.

To make further progress, we will derive a useful property of the functional delta distribution by considering first a function f discretised on a lattice $\{\mathbf{r}_i\}$. As the functional delta distribution is defined in analogy to the conventional delta function

$$I[g] = \int \delta[f-g] I[f] \, \mathfrak{D}f, \quad \forall I, \tag{2.4}$$

it is simply the product of conventional delta functions on each lattice point

$$\delta[f] = \prod_i \delta(f(\mathbf{r}_i)). \tag{2.5}$$

Hence

$$\delta[f] = \prod_i \int \mathrm{d}k_i e^{ik_i f(\mathbf{r}_i)} \tag{2.6}$$

$$= \int \left(\prod_i \mathrm{d}k_i \right) e^{i \sum_i k_i f(\mathbf{r}_i)}. \tag{2.7}$$

Passing to the continuum limit, the functional delta distribution can be written as a functional Fourier transform

$$\delta[f] = \int e^{i \int \mathrm{d}\mathbf{r} \, k(\mathbf{r}) f(\mathbf{r})} \, \mathfrak{D}k \tag{2.8}$$

where we identified $\prod_i \mathrm{d}k_i$ as the functional integral measure $\mathfrak{D}k$ in the continuum limit. Therefore, we can write the functional delta function in Equation (2.3) as

$$\delta[\rho_\pm - \hat{\rho}_\pm] = \int \mathfrak{D}\psi_\pm \exp\left\{ i \int \mathrm{d}\mathbf{r} \; \psi_\pm(\rho_\pm - \hat{\rho}_\pm) \right\}. \tag{2.9}$$

Substituting Equation (2.9) into (2.3), we arrive at

$$\begin{aligned} Z_{N_+,N_-} \quad = \quad & \frac{A}{N_+! N_-!} \int \mathfrak{D}\rho_+ \mathfrak{D}\rho_- \mathfrak{D}\psi_+ \mathfrak{D}\psi_- \\ & \exp\Bigg\{ -\frac{l_B}{2} \int \mathrm{d}\mathbf{r} \int \mathrm{d}\mathbf{r}' [\rho_+(\mathbf{r}) - \rho_-(\mathbf{r}) - \sigma(\mathbf{r})] v(\mathbf{r}-\mathbf{r}') \\ & [\rho_+(\mathbf{r}') - \rho_-(\mathbf{r}') - \sigma(\mathbf{r}')] + i \int \mathrm{dr} \, [\rho_+(\mathbf{r})\psi_+(\mathbf{r}) + \rho_-(\mathbf{r})\psi_-(\mathbf{r})] \Bigg\} \\ & \times \int \prod_{j=1}^{N_+} \frac{\mathrm{d}\mathbf{r}_j^+}{\lambda_T^3} e^{-i \int \mathrm{d}\mathbf{r} \hat{\rho}_+(\mathbf{r}) \psi_+(\mathbf{r})} \int \prod_{j=1}^{N_-} \frac{\mathrm{d}\mathbf{r}_j^-}{\lambda_T^3} e^{-i \int \mathrm{d}\mathbf{r} \hat{\rho}_-(\mathbf{r}) \psi_-(\mathbf{r})}. \end{aligned} \tag{2.10}$$

Recalling the definition of $\hat{\rho}_\pm$, the remaining integration over position degrees of freedom can be evaluated exactly to give

$$\int \prod_{j=1}^{N_\pm} \frac{\mathrm{d}\mathbf{r}_j^\pm}{\lambda_T^3} e^{-i\int \mathrm{d}\mathbf{r}\hat{\rho}_\pm(\mathbf{r})\psi_\pm(\mathbf{r})} = \left[\int \frac{\mathrm{d}\mathbf{r}}{\lambda_T^3} e^{-i\psi_\pm(\mathbf{r})}\right]^{N_\pm}. \tag{2.11}$$

The partition function can be transformed into the grand canonical ensemble by defining the grand potential

$$\Lambda = \sum_{N_+,N_-=0}^{\infty} \lambda^{N_++N_-} Z_{N_+,N_-} \tag{2.12}$$

where λ is the fugacity, assumed to be the same for both cation and anions. Noting the power series expansion for the exponential function $e^x = \sum_{n=0}^{\infty} x^n/n!$, we obtain

$$\Lambda = \int \mathfrak{D}\rho_+\mathfrak{D}\rho_-\mathfrak{D}\psi_+\mathfrak{D}\psi_- e^{-H[\rho_+,\rho_-,\psi_+,\psi_-]}, \tag{2.13}$$

where the effective Hamiltonian reads

$$\begin{aligned} H[\rho_+,\rho_-,\psi_+,\psi_-] \quad &= \frac{l_B}{2}\int \mathrm{d}\mathbf{r} \int \mathrm{d}\mathbf{r}'[\rho_+(\mathbf{r}) - \rho_-(\mathbf{r}) - \sigma(\mathbf{r})]v(\mathbf{r}-\mathbf{r}')[\rho_+(\mathbf{r}') - \rho_-(\mathbf{r}') - \sigma(\mathbf{r}')] \\ &-i\int \mathrm{d}\mathbf{r}[\rho_+(\mathbf{r})\psi_+(\mathbf{r}) + \rho_-(\mathbf{r})\psi_-(\mathbf{r})] \\ &-\tilde{\lambda}\int \mathrm{d}\mathbf{r}\left[e^{-i\psi_+(\mathbf{r})} + e^{-i\psi_-(\mathbf{r})}\right], \end{aligned} \tag{2.14}$$

with $\tilde{\lambda} = \lambda e^{q^2 l_B v(0)/2}/\lambda_T^3$.

Up to this point, we have made no approximation — Equation (2.13) is formally exact. However, the functional integral is analytically and numerically intractable, as it effectively consists of four infinite dimensional integrals over the entire function space. To make some progress, we invoke the so-called saddle-point approximation of statistical physics, where we posit that the thermodynamic properties of the system are determined by the extremum of the functional integrand, *i.e.*

$$\frac{\delta H}{\delta \psi_\pm} = 0, \quad \frac{\delta H}{\delta \rho_\pm} = 0. \tag{2.15}$$

The variational derivative with respect to $\psi_\pm$ yields

$$\psi_\pm = i\log\left(\frac{\rho_\pm(\mathbf{r})}{\tilde{\lambda}}\right), \tag{2.16}$$

and the variational derivative with respect to $\rho_\pm$ yields

$$\pm l_B \int \mathrm{d}\mathbf{r}'\left[v(\mathbf{r}-\mathbf{r}')(\rho_+(\mathbf{r}') - \rho_-(\mathbf{r}') + \sigma(\mathbf{r}'))\right] + \log\frac{\rho_\pm}{\tilde{\lambda}} = 0. \tag{2.17}$$

The fugacity $\tilde{\lambda}$ is related to the bulk concentration by noting that in the bulk solution, the first term in Equation (2.17) vanishes and we must therefore have $\tilde{\lambda} = \rho_0$, the concentration of ions in the bulk (thermodynamic reservoir). Observing that $\nabla^2 v(\mathbf{r} - \mathbf{r}') = -\delta(\mathbf{r} - \mathbf{r}')$, by properties of the Green's function, we can rewrite the nonlocal integral equation in terms of an auxiliary field u, yielding

$$u(\mathbf{r}) + \log \frac{\rho_\pm}{\rho_0} = 0, \tag{2.18}$$

with

$$\nabla^2 u = -\kappa^2(\rho_+(\mathbf{r}) - \rho_-(\mathbf{r}))/\rho_0 - 4\pi l_B \sigma(\mathbf{r}). \tag{2.19}$$

where $\kappa = \sqrt{4\pi\rho_0 l_B}$ is the inverse Debye length. Substituting Equation (2.18) into (2.17), we arrive at the Poisson-Boltzmann equation

$$\nabla^2 u = \kappa^2 \sinh u - 4\pi l_B \sigma(\mathbf{r}). \tag{2.20}$$

Equation (2.20) may obviously be interpretated as the Poisson's equation with $u = eV/(k_B T)$ being the dimensionless electric potential, and the charge density determined by the Boltzmann distribution.

This field theoretic derivation highlights two major pitfalls of the Poisson-Boltzmann theory:

- The Poisson–Boltzmann equation completely neglects thermodynamic fluctuations. In trying to simplify the path integral (2.13), we have made a “leap of faith” that all thermodynamic properties are dominated by the saddle point. Contributions from configurations close to but not at the saddle point could give rise to highly non-trivial behaviour; we will see examples in the remainder of this thesis of such behaviour.
- We have neglected hard core repulsion between ions. In fact, the fugacity $\tilde{\lambda}$ is formally divergent since the self-energy $v(0)$ is infinite. Here, we have implicitly employed renormalisation arguments to “renormalise” the divergent Coulomb potential by redefining the fugacity. Physically, hard core repulsion can give rise to rich behaviour, as exemplified by ion packing.

2.2 Predictions of the Poisson-Boltzmann Theory

We will now illustrate the predictions of the Poisson-Boltzmann formalism by solving (2.20) for a spherical ion immersed in a background electrolyte, and electrolytes confined between parallel electrodes. These model problems motivate Chapters 3 and 4 of the thesis. To make these problems analytically tractable, we will use the small potential approximation to linearise the $\sinh u$ term in (2.20), arriving at the linearised Poisson–Boltzmann equation

$$\nabla^2 u - \kappa^2 u = -4\pi l_B \sigma(\mathbf{r}). \tag{2.21}$$

We note that the linearisation is a relatively mild approximation since the nonlinear Poisson-Boltzmann equation is, in any case, no longer a good model for large potentials where hard core exclusion and electrostatic correlations become important.

2.2.1 Screening of a Spherical Ion

We consider the (radially symmetric) electric potential around a spherical ion immersed in a bath of electrolyte (see Figure 2.2 for a sketch). Modelling the ion as a charged spherical shell, Equation (2.21) reads

$$\frac{1}{r^2}\frac{\mathrm{d}}{\mathrm{d}r}\left(r^2\frac{\mathrm{d}u}{\mathrm{d}r}\right) - \kappa^2 u = -4\pi l_B \Sigma\delta(r-a),\ r > a, \tag{2.22}$$

where Σ is the surface charge density of the ion (divided by the fundamental charge e), and a is the radius of the exclusion sphere (*i.e.* the diameter of the spherical ion). The solution of Equation (2.22) for a monovalent positive ion, subjected to the far field condition $u \to 0$ as $r \to \infty$ and the jump condition $u'(a) = -l_B/a^2$ (as $\Sigma = 1/(4\pi a^2)$) is given by the well-known Debye-Hückel solution

$$u(r) = \frac{l_B}{r}\frac{e^{\kappa(a-r)}}{1+\kappa a}, \quad r > a. \tag{2.23}$$

Equation (2.23) shows that the presence of free ions turns the electrostatic interaction from algebraic to exponential decay with a screening length κ^{-1}.

Heuristically, the physics of the screening length can be understood via a simple thought experiment: Consider a homogeneous neutral salt solution with average ion density ρ. Though the solution is macroscopically homogeneous, the number of charges, $n_\pm$, fluctuates in a small volume r^3. Assuming that these fluctuations are Gaussian, we have $\Delta n_\pm / n_\pm \sim 1/\sqrt{n_\pm}$ thus $\Delta n_\pm \sim \sqrt{n_\pm}$. Noting that the self energy of a charged sphere of radius r is given by $E_{\text{self}} \propto k_B T l_B / r$, the fluctuation energy scales as (for small r)

$$E_{\text{fluc}} \propto k_B T \frac{l_B}{r}[(n_\pm + \Delta n_\pm)^2 - n_\pm^2] \overset{r\to 0}{\sim} k_B T \frac{l_B}{r}(\Delta n_\pm)^2 \sim k_B T \frac{l_B}{r} n_\pm = k_B T l_B \rho r^2. \tag{2.24}$$

As the fluctuations are driven by thermal energy, we have

$$E_{\text{fluc}} \sim k_B T \implies r \sim \frac{1}{\sqrt{l_B \rho}}, \tag{2.25}$$

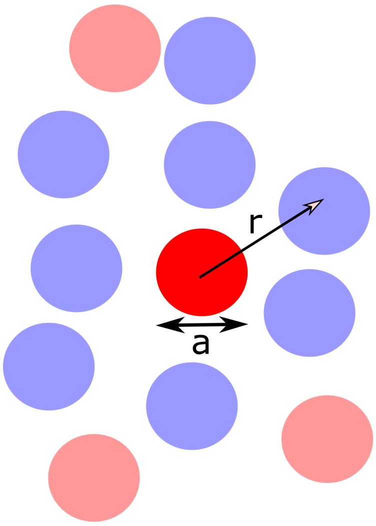

Figure 2.2: *The electric potential around an ion immersed in a bath of electrolyte.*

which is the Debye length up to constant factors. This heuristic argument shows that the Debye length is the characteristic lengthscale of microscopic charge density fluctuations. Beyond the Debye length, fluctuations are energetically too costly and thus the density is uniform.

Although the Debye picture is physically appealing, it assumes that all ions in solution can participate in electric field screening. However, oppositely charged ions attract each other (even when the interactions are screened). It therefore seems intuitively reasonable that some ions may be bundled up as *dipolar* ion pairs which do not contribute to Debye screening. Therefore, even an ionic liquid is not necessarily a concentrated electrolyte. We will return to this issue in Chapter 3.

2.2.2 Disjoining Pressure between Two Charged Surfaces

A large portion of this thesis will be concerned with the behaviour of ionic liquids in confined systems. To extend the Poisson-Boltzmann picture to a confined ionic liquid, we consider the disjoining pressure induced by ions between two charged surfaces located at $x = \pm D/2$. In this geometry, Equation (2.21) reads

$$\frac{\mathrm{d}^2 u}{\mathrm{d}x^2} - \kappa^2 u = -4\pi l_B \Sigma \delta(|x| - D/2), \ |x| < D/2. \tag{2.26}$$

We note that Equation (2.26) is a homogeneous ODE with boundary conditions $u'|_{\pm D/2} = \pm 4\pi l_B \Sigma$ (assuming the field is zero outside the surfaces). This ODE can readily be integrated to give

$$u = 4\pi l_B \frac{\Sigma \cosh \kappa x}{\kappa \sinh(\kappa D/2)}. \tag{2.27}$$

A quantity of experimental interest is the disjoining pressure. The pressure can be computed from the concentration profile via the Gibbs-Duhem equation in classical thermodynamics. At constant temperature and surface separation, we have

$$\mathrm{d}\Pi = \rho_+ \mathrm{d}\mu_+ + \rho_- \mathrm{d}\mu_-, \tag{2.28}$$

where $\Pi = p/k_B T$ is the dimensionless pressure. Recalling the definition of chemical potential $\mu_\pm = \delta F/\delta \rho_\pm$, where

$$F = \int \mathrm{d}\mathbf{r} \left\{ u(\mathbf{r})(\rho_+(\mathbf{r}) - \rho_-(\mathbf{r}) - \sigma(\mathbf{r})) + \sum_{\alpha=\pm} \rho_\alpha(\mathbf{r}) \left[\log\left(\frac{\rho_\alpha(\mathbf{r})}{\rho_0} \right) - 1 \right] \right\} \tag{2.29}$$

is the free energy (*c.f.* Equations (2.14) - (2.17)), we have $\mu_\pm = \pm u + \log(\rho_\pm/\rho_0)$. As such

$$\begin{aligned} \mathrm{d}\Pi &= \mathrm{d}u(\rho_+ - \rho_-) + \mathrm{d}(\rho_+ + \rho_-) \\ &= -\kappa^{-2} \mathrm{d}u \frac{\mathrm{d}^2 u}{\mathrm{d}x^2} + \mathrm{d}(\rho_+ + \rho_-) \\ &= -\frac{\rho_0}{2\kappa^2} \mathrm{d}\left(\frac{\mathrm{d}u}{\mathrm{d}x} \right)^2 + \mathrm{d}(\rho_+ + \rho_-), \end{aligned} \tag{2.30}$$

and so, we arrive at

$$\Pi = -\frac{\rho_0}{2\kappa^2} \left(\frac{\mathrm{d}u}{\mathrm{d}x} \right)^2 + (\rho_+ + \rho_- - 2\rho_0). \tag{2.31}$$

In the last step we have used the fact that pressure in the bulk solution is zero to fix the constant of integration. At equilibrium, the pressure at each point must be the same, hence we can evaluate Π at the mid-plane where the electric field vanishes by symmetry ($u' = 0$) and obtain

$$\Pi = \rho_+(0) + \rho_-(0) - 2\rho_0 \tag{2.32}$$

$$\begin{aligned} &\approx \rho_0 u(0)^2 \\ &= \rho_0 \left(4\pi \Sigma l_B \kappa^{-1} \right)^2 \operatorname{csch}^2(\kappa D/2), \end{aligned} \tag{2.33}$$

which is a monotonic function of D. Equation (2.32) shows that the disjoining pressure is effectively an osmotic pressure due to excess ion density at mid-plane. Note in particular that $\Pi > 0$ for all parameter values (see Equation (2.33)).

Figure 2.3 shows the experimentally measured disjoining force ($F_N = \Pi A$, with A the area of the plates) for an ionic liquid confined between two charged plates. Note that the experimental results are starkly different to those predicted by Equation (2.33): Experimentally, the force decays in an oscillatory matter, while (2.33) predicts that it should decay monotonically with D. Rationalising this disrepancy requires a new statistical mechanical framework that takes into account ion-ion correlations and hard core exclusion beyond the mean-field approximation used in the derivation of the Poisson-Boltzmann equation. This is the subject of Chapter 4.

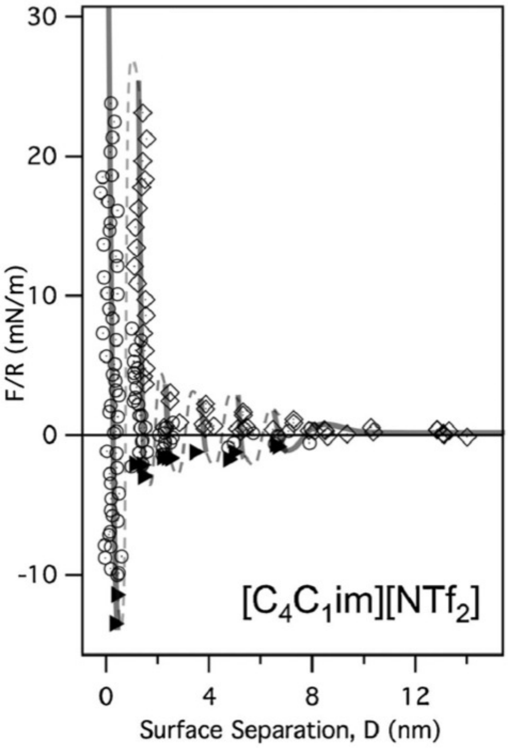

Figure 2.3: *The disjoining force measured across negatively charged mica surfaces using a surface force balance is oscillatory rather than monotonic. R is the radius of curvature of the plates (perfectly flat plates are experimentally difficult to achieve and the mica sheets are mounted on crossed cylinders). The plot is taken from Perkin et al. (2011).*

CHAPTER 3

Structure of Bulk Ionic Liquids

Synopsis

An important question for our understanding of the structure of ionic liquids is whether ions are truly "free" and mobile (a concentrated ionic solution), or are rather "bound" in ion pairs (a dilute solution of free ions dissolved in ion pairs). Recent surface force balance experiments from different groups give conflicting answers to this question. We propose a simple model for the thermodynamics and kinetics of ion pairing in ionic liquids taking into account screened ion-ion, dipole-dipole and dipole-ion interactions in the mean field limit. The results of this model suggest that almost two thirds of the ions are mobile, and that ion pairs have a relatively short lifetime comparable to the timescale of translational diffusion. We therefore conclude that ionic liquids are best considered to be concentrated electrolytes.

A paper based on some of the work described in this Chapter has been published in the *Journal of Physical Chemistry Letters.* (Lee et al., 2015b)

3.1 Introduction

At first sight an ionic liquid might naturally be expected to be a fluid of free ions. However, the presence of strong and long-ranged Coulomb interactions makes the picture more complicated. Recent surface force balance experiments by Gebbie et al. (2013a; 2015) on ionic liquids confined between charged surfaces have measured the double layer forces. They found that their results can be fitted to the linear Debye-Hückel theory (*c.f.* Section 2.2.2) but with a very large Debye screening length, of $O(10\mathrm{nm})$. Since a large Debye length generally corresponds to a dilute electrolyte solution, they concluded that the concentration of ions is low. As an ionic liquid is nothing but a sea of ions, for the concentration of free ions to be low, the majority of ions in solution must therefore be bound as cation-anion pairs that behave effectively as dipoles. From these experimental observations, Gebbie et al. (2013a) suggested that ionic liquids behave as dilute electrolytes. We note that the experimental data reported by Gebbie et al. (2013a) is qualitatively very different to the data obtained by Perkin et al. (2011) (*c.f.* Figure 2.3) as well as other previous experimental studies; we will discuss this in Section 3.4.

The above picture of ionic liquids triggered extensive discussions in the literature (Perkin et al., 2013; Gebbie et al., 2013b). A key theoretical argument for the dilute electrolyte picture is the apparently large association constant. Gebbie et al. (2013a) suggested that the equilibrium constant for association may be estimated as

$$K = \exp\left(-\frac{\Delta E_d}{\epsilon k_B T}\right) \tag{3.1}$$

with the dissociation energy of ion pairs $\Delta E_d = 315.26\ \mathrm{kJmol}^{-1}$ taken from quantum electronic structure calculations by Hunt et al. (2007) for an ion pair in vacuum, and $\epsilon = 11.6$, the low frequency dielectric constant measured by Weingärtner (2008) using dielectric spectroscopy. However, several assumptions have been made to arrive at this estimate. The value of ΔE_d used is the theoretical gas phase dissociation energy, which is likely to be an overestimate because it neglects the electrostatic screening due to the presence of other free ions (Lynden-Bell, 2010). Furthermore, dividing the interaction energy by the dielectric constant, as measured from dielectric spectroscopy, is unlikely to be able to account for the electrostatic interaction between the ions (Schröder et al., 2008; Lynden-Bell, 2010). Therefore, Equation (3.1) can only be expected to hold when the concentration of free ions is low, since it implicitly assumes that the typical interaction energy between a bound ion and a neighbouring free charge is significantly less than the thermal energy (Fowler and Guggenheim, 1949). Given this caveat, it is perhaps unsurprising that Gebbie et al. (2013a) arrived at the conclusion that ionic liquids are dilute electrolytes.

In this Chapter, we attempt to remove some of the above assumptions. The key questions that we would like to answer are: Are ion pairs abundant in solution? If so, are they long-lived species, or transient intermediates? To estimate the abundance and the lifetime of ion pairs in ionic liquids, we develop a simple theory of ion pairing that accounts for both screened electrostatic interactions and a dielectric constant that is self-consistently calculated from the concentration of ion-pair dipoles.

We note that the notion of association equilibrium is artificial: In reality, the liquid is a sea of ions interacting via a Coulomb potential, and the notion of an "ion pair" is redundant if we have a complete statistical mechanical theory. Nonetheless the idea of ion pairing is an extremely useful mental picture and provides intuition for chemical and physical analogies with dilute/concentrated electrolytes. From a theoretical point of view, the idea of ion pairing can be seen as a tool to account for ion-ion correlations beyond mean-field (Poisson-Boltzmann) approximation. Indeed, this modification to the linearised Poisson Boltzmann theory has been used successfully to model criticality in a Coulomb fluid (Levin and Fisher, 1996).

3.2 Thermodynamics of Ion Association

We take as our staring point the physical picture of Gebbie et al. (2013a), *i.e.* a dipolar background containing free ions. However, we avoid making any a priori assumption about the concentration of these free ions.

In such an ionic liquid, ions interact with one another but are screened by other free ions, and a background dielectric medium that consists of dipolar ion pairs. At the same time, dipoles (ion pairs) interact with one another, and the dipole-dipole interactions are screened by the presence of free ions and other dipoles (see Fig. 3.1 for a schematic of the system).

In the sections below, we will construct a theory of ion association based on the law of mass action, and relate the fraction of free ions to the ion-ion interaction energy. The ion-ion interaction energy depends on the dielectric constant, which accounts for dipole-dipole interactions in a sea of ions. We will construct a theory for the dielectric constant based on mean-field effective medium approximation. This approach will allow us to formulate a closed system with the ion diameter and geometrical packing fraction as inputs, and the proportion of free ion as output.

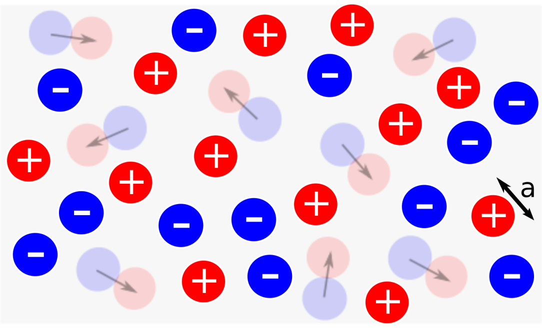

Figure 3.1: *An ionic liquid is modelled as a mixture of free ions (coloured spheres) and bounded ion pair dipoles (dumbbells). The free ions provide a characteristic Debye screening length* κ^{-1} *while the dipoles provide a background dielectric constant* ϵ.

3.2.1 From Interaction to Association

To determine the fraction of free ions, α, we consider a "chemical" equilibrium between free ions and ion pairs,

$$\text{cation } + \text{ anion} \rightleftharpoons \text{ dipoles}. \tag{3.2}$$

The law of mass action gives the equilibrium constant

$$K \equiv \frac{\rho_d}{\rho_+\rho_-} = 2\frac{1-\alpha}{\rho\alpha^2}, \tag{3.3}$$

where ρ_d, ρ_+ and ρ_- are the densities of dipoles, cations and anions, respectively, and ρ is the total density of ions (where one dipole is counted as two ions). By mass balance and electroneutrality, the cation and anion densities are $\rho_+ = \rho_- = \alpha\rho/2$, while the ion pair density $\rho_d = (1-\alpha)\rho/2$. Determining α is the central goal of our analysis; ionic liquids would be dilute electrolytes if $\alpha \ll 1$.

Intuitively, K is related to the ion-ion interaction energy $v(r)$ — strong ion-ion interactions should favour ion pairing. However, the relation between K and the interaction potential $v(r)$ has been a subject of debate in the literature. Part of the problem lies in the inherently fuzzy distinction between molecular association and intermolecular interactions: when should one consider two oppositely charged ions "paired"? One popular definition proposed by Bjerrum neglects Debye screening, and considers the concentration of an oppositely charged ions near a reference ion (Robinson and Stokes, 2002). The average local concentration of cations located at distance r away from an anion is given by the Boltzmann distribution

$$\mathfrak{c}(r) = \rho_+ e^{\beta v(r)} = \rho_+ e^{\frac{l_B}{r}}, \tag{3.4}$$

where the Coulombic potential $v(r) = e^2/(\epsilon r)$, and

$$l_B = \frac{e^2}{\epsilon k_B T} \tag{3.5}$$

is the Bjerrum length, the typical distance over which electrostatic interactions between two charges of charge e in a dielectric medium of relative dielectric constant ϵ is compared to thermal energy k_BT. By definition, the probability $P(r)$ of finding a counterion at a distance between r and $r + \mathrm{d}r$ away from the central ion is given by

$$P(r) = 4\pi r^2 \mathfrak{c}(r)\mathrm{d}r. \tag{3.6}$$

Now, Bjerrum reasoned that the fraction $1 - \alpha$ of ions that are associated into ion-pairs is equivalent to the total probability of ion pair formation. Thus

$$1 - \alpha = \rho_+ \int_a^\infty 4\pi r^2 e^{\frac{l_B}{r}} \,\mathrm{d}r. \tag{3.7}$$

Equation (3.7) is problematic since the integral is divergent at ∞! To remedy this, Bjerrum proposed a cut-off distance r_c. In his original formulation, r_c was chosen to be the minimum of $f(r) = 4\pi r^2\mathfrak{c}(r)$, *i.e.* $r_c = 2l_B$. Physically, r_c defines what an ion pair is: an ion pair is a pair of oppositely charged ions separated by at most r_c. However, the choice of r_c is not unique — one may think of other equally plausible ways to cut off the range of integration. One requirement could be $3k_BT/2 \leq q^2/(\epsilon r)$, *i.e.* the average internal kinetic energy should be smaller than the Coulomb energy, and thus $r_c = 3l_B/2$.

To avoid an arbitrary distance criterion for ion pairs, we adopt another view of ion pairs: First, note that ion pairing is driven by an *excess* of counterions around the central ion. The Bjerrum formulation does not separate the excess counterion density due to the presence of an oppositely charged ion from the bulk concentration — this is the reason why the integrand in (3.7) does not vanish as $r \to \infty$. Therefore, the integrand in (3.7) should be replaced by $P_{\text{ex}} = 4\pi r^2 \rho_+ (e^{-\beta u(r)} - 1)$, where $u(r)$ is the *potential of mean force* between two ions. Therefore,

$$1 - \alpha = \rho_+ \int_a^\infty 4\pi r^2 (e^{-\beta u(r)} - 1) \,\mathrm{d}r. \tag{3.8}$$

Bjerrum's assumption that $\beta u(r) = l_B/r$, the bare Coulombic potential, is only correct if there are no other free ions around: The presence of other free ions screens the ion-ion electrostatic interaction. We will calculate $u(r)$ in the next section.

To put Equation (3.8) on a firmer physical footing, we will review another derivation by Woolley (1953), which considers ion-pairs as a correction to ideal gas behaviour and self-consistently relate the virial coefficients to the association constant. Assuming that ion-pair formation is sufficient to account for deviation of the system from ideal gas behaviour, the total pressure of the system is proportional to the number of molecular entities (dipoles or free ions) in a given volume, and thus

$$\beta p = \rho_1 + \rho_d \tag{3.9}$$

where $\rho_1 = \rho_+ + \rho_-$ is the total concentration of free ions. The total particle density of the system, however, is given by

$$\rho = \rho_1 + 2\rho_d, \tag{3.10}$$

thus the compressibility factor, $\chi \equiv \beta p/\rho$, can be written as

$$\chi = \frac{\rho_1 + \rho_d}{\rho_1 + 2\rho_d} = \frac{\rho_1 + K\rho_1^2}{\rho_1 + 2K\rho_1^2}, \tag{3.11}$$

where in the last line we have used the fact that the association constant is given by $K = \rho_d/\rho_1^2$ (*c.f.* Equation 3.3). We can rewrite Equation (3.11) as

$$\chi = \frac{\beta p}{\rho_1}\frac{\mathrm{d}\rho_1}{\mathrm{d}(\beta p)}. \tag{3.12}$$

To determine χ, we require a relationship between ρ_1 and βp. To find this, we rearrange Equation (3.9) and substitute (3.3) for the equilibrium constant. Solving the resulting quadratic equation, we arrive at

$$\rho_1 = \frac{-1 + \sqrt{1 + 4K\beta p}}{2K}. \tag{3.13}$$

Substituting Equation (3.13) into (3.12), we arrive at

$$\chi = \frac{2\beta p K}{1 + 4K\beta p - \sqrt{1 + 4K\beta p}} = 1 - K\beta p + O((K\beta p)^2), \tag{3.14}$$

where considering $\beta K p \ll 1$ is justified as ion-pairing is treated as a perturbative correction to ideal gas behaviour. Comparing Equation (3.14) with the classical virial equation of state $\chi = 1 + B_2\beta p + ...$, we find a relation between the equilibrium constant and the second virial coefficient

$$K = -B_2. \tag{3.15}$$

The second virial coefficient can be expressed in terms of the interaction potential via the classical theory of non-ideal gases (the so-call Mayer-f expansion, see *e.g.* Kardar, 2007), and the resulting expression reads

$$K = 4\pi \int_a^\infty \mathrm{d}r \, \left[r^2 (e^{-\beta u(r)} - 1) \right]. \tag{3.16}$$

We will use Equation (3.16) and (3.3) later to compute α, the fraction of free ions. We note that

$$\rho K = (1-\alpha)(1 + (1-\alpha)^2 + \cdots), \tag{3.17}$$

therefore, as long as $(1-\alpha)^2 \ll 1$, *i.e.* the solution predominantly consists of free ions, deriving the association constant via the viral route, Equation (3.16) is consistent with deriving it via probabilistic route (Equation (3.8)).

3.2.2 Interionic Interactions

A simple model for charge-charge interaction is the linearised Poisson-Boltzmann approach. Assuming that the ions are hard spheres of diameter a that create an exclusion sphere of radius a, the interaction potential $u(r)$ between two monovalent ions with opposite charges $\pm e$ can be obtained by solving the linearised Poisson-Boltzmann equation with a uniform charge density on the surface of the exclusion sphere (Fisher and Levin, 1993). This yields (see Chapter 2 and Equation (2.23))

$$\beta u(r) = -\frac{l_B}{r} \frac{e^{\kappa(a-r)}}{\kappa a + 1}. \tag{3.18}$$

Equation (3.18) is known as the Debye-Hückel law. Here we have introduced the inverse Debye screening length

$$\kappa = \sqrt{4\pi l_B (\rho_+ + \rho_-)} = \sqrt{4\pi l_B \alpha \rho}, \tag{3.19}$$

where ρ is the total number density of ions. The Debye length describes the physics of electric field screening by free ions. The fraction of ions dissociated, α, is the central parameter which provides the answer to whether ionic liquids can be considered dilute electrolyte or not, and will be computed later. (Note that the thermal Bjerrum length l_B which we introduced in Section 3.2.1 is the typical distance over which the electrostatic interaction between two charges of charge e in a dielectric medium of relative dielectric constant ϵ, *without any surrounding ions*, is comparable to the thermal energy $k_B T$.)

To account for the polarisability of ions, we scale charge and take $q = e/\sqrt{\epsilon_\infty}$ for a monovalent ionic liquid (Yu and van Gunsteren, 2005; Leontyev and Stuchebrukhov, 2009), where ϵ_∞ is the optical (high frequency) dielectric constant. Heuristically, this scaling can be derived by noting that the actual Coulomb interaction between two polarisable like charges in the absence of any dipoles is given by $e^2/(\epsilon_\infty r)$. Therefore, ion polarisability is equivalent to decreasing the charge e by a factor $1/\sqrt{\epsilon_\infty}$. Such charge-scaling is shown by simulation to give distribution functions that are excellent approximations to the full electrostatic problem with polarisability (Schröder, 2012).

3.2.3 The Dielectric Constant

Definition (3.5) for l_B involves ϵ, the dielectric constant. An ionic liquid is a pure substance and so there is no true "background" dielectric. Instead it is the ion pair dipoles that must provide the effective dielectric constant. In this section, we will first consider the electric field generated by a dipole in a dielectric medium in response to an applied electric field. Then, using the Boltzmann distribution to compute the average polarisation of the medium, we will self-consistently determine the dielectric constant.

An important subtlety with calculating the dielectric constant in ionic fluids is that the presence of free charges allows the medium to conduct. Thus a static electric field will induce a constant flow of ionic current, and the dielectric constant is ∞ (akin to a metal, which to first approximation is a fluid of electrons). However, the movement of ions across the whole cell is diffusion limited (the electrode polarisation timescale) and thus is much slower than the reorientation of dipoles. The dielectric constant that enters the Bjerrum length (3.5) characterises the response of the medium to thermally-induced fluctuations in the orientation of dipoles. Therefore, it not the *static* dielectric constant that matters, but rather a dynamic dielectric constant that captures the (linear) response of the medium to a time-harmonic electric field with sufficiently high frequency such that the ionic conductivity becomes irrelevant. We will revisit this issue in due course.

We treat the sea of ion pairs as a dipolar fluid consisting of polarisable spheres with dipole moment μ whose interactions are screened by free ions. To derive the dielectric constant, we need to study how a dipole in a background dielectric reacts to an applied field. We first review the approach of Schröer (2001), who generalised a classical result due to Onsager (1936). Our aim here is to clarify the assumptions underpinning the final result.

To make the full problem trackable, we will first consider two sub-problems in classical electrostatics: the problem of a point dipole in a dielectric sphere, then a dielectric sphere with an applied electric field. By exploiting linearity in the Debye-Hückel equation and the Poisson equation, we will then compute the interaction energy between a dipole and the external field. Finally, we will compute the average dipole orientation, and hence the polarisation of the medium, by averaging the dipole orientation over the Boltzmann distribution.

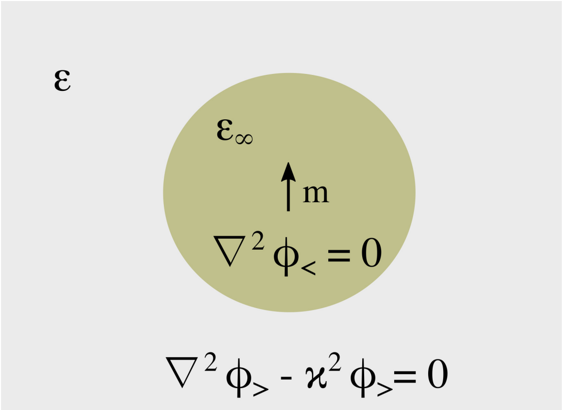

Figure 3.2: *A point dipole of dipole moment μ submerged in a continuum of Debye length κ and dielectric constant ϵ.*

We begin by considering a point dipole in a dielectric sphere of radius a_d of dielectric constant ϵ_∞ submerged in an electrolyte with Debye length κ and dielectric constant ϵ (see Figure 3.2). Outside the dipole sphere, the electric potential satisfies the Debye-Hückel equation

$$\nabla^2 \phi_> = \kappa^2 \phi_>, \quad r > a_d \tag{3.20}$$

and inside the sphere the electric potential satisfies the Poisson equation

$$\nabla^2 \phi_< = 0, \quad 0 < r < a_d. \tag{3.21}$$

Separation of variables yields the general solutions

$$\phi_< = \sum_{l=0}^{\infty} \left(\frac{A_l}{r^{l+1}} + B_l r^l \right) P_l(\cos\theta), \tag{3.22}$$

$$\phi_> = \sum_{l=0}^{\infty} \Big[C_l k_l(\kappa r) + D_l i_l(\kappa r) \Big] P_l(\cos\theta), \tag{3.23}$$

where A, B, C, D are constants of integration, $k_l(x)$ and $i_l(x)$ are the l^{th} modified spherical Bessel function of first and second kind, respectively, and $P_l(x)$ is the l^{th} Legendre polynomial. For a point dipole, only the $l = 1$ terms are non-zero. By noting that $\phi_< \to m\cos\theta/(\epsilon_\infty r^2)$, as $r \to 0$, and the dipole field decays to zero as $r \to \infty$, we have $A_l = m/\epsilon_\infty$ and $D_l = 0$. The remaining constants can be determined by continuity of the electric potential at $r = a_d$, *i.e.*

$$\phi_<(a_d, \theta) = \phi_>(a_d, \theta), \tag{3.24}$$

and Gauss' Law

$$\epsilon_\infty \frac{\partial \phi_<}{\partial r}\bigg|_{r=a_d} = \epsilon \frac{\partial \phi_>}{\partial r}\bigg|_{r=a_d} . \tag{3.25}$$

Equation (3.24) implies

$$\frac{m}{\epsilon_\infty a_d^3} + B_1 = \frac{C_1}{a_d}(1+\kappa a_d)\frac{e^{-\kappa a_d}}{(\kappa a_d)^2}, \tag{3.26}$$

and Equation (3.25) implies

$$\epsilon_\infty \left(B_1 - \frac{m}{\epsilon_\infty a_d^3} \right) = -\epsilon \frac{C_1}{a_d} \left(\frac{e^{-\kappa a_d}}{(\kappa a_d)^2} \left[(\kappa a_d)^2 + 2\kappa a_d + 2 \right] \right). \tag{3.27}$$

From Equations (3.25)-(3.27), we arrive at

$$B_1 = -\frac{m}{\epsilon_\infty a_d^3} \frac{2(\epsilon - \epsilon_\infty)(1+\kappa a_d) + \epsilon (\kappa a_d)^2}{(2\epsilon + \epsilon_\infty)(1+\kappa a_d) + \epsilon(\kappa a_d)^2}, \tag{3.28}$$

$$C_1 = \frac{3 m \kappa^2 e^{\kappa a_d}}{(2\epsilon + \epsilon_\infty)(1+\kappa a_d) + \epsilon (\kappa a_d)^2}. \tag{3.29}$$

Physically, C_1 is the external moment of the immersed dipole — it determines the force, modified by the intervening ionic medium, that the dipole will exert upon a distant charge in the medium. On the other hand, B_1 is the electric field that acts upon the dipole as a result of the electric displacement induced by its own presence, and is known as the "reaction field". The dipole moment of the molecule is the sum of its permanent dipole with moment μ, and dipole moment induced by the reaction field as the molecule is polarisable. As such, the effective dipole moment is given by

$$m = \mu + \nu E_{\text{reaction}} = \mu + \nu m R, \tag{3.30}$$

where ν is the polarisability, and

$$R = \frac{1}{\epsilon_\infty a_d^3} \frac{2(\epsilon - \epsilon_\infty)(1+\kappa a_d) + \epsilon(\kappa a_d)^2}{(2\epsilon + \epsilon_\infty)(1+\kappa a_d) + \epsilon(\kappa a_d)^2}. \tag{3.31}$$

Thus the effective dipole moment m is given by

$$m = \frac{\mu}{1 - \nu R}. \tag{3.32}$$

(We note that the m is aligned with the dipole, hence we suppressed vector notation for simplicity.)

Next, we consider how a dielectric sphere immersed in an electrolyte responds to an

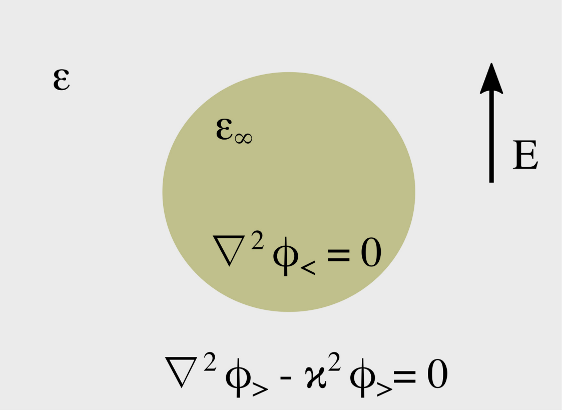

Figure 3.3: *A dielectric sphere immersed in a electrolyte with an imposed external electric field E.*

external imposed electric field E (see Figure 3.3).

Following the previous analysis, the general solution inside the sphere reads

$$\phi_< = B_1' r \cos\theta, \tag{3.33}$$

where $A_1' = 0$ as the solution must be non-singular at the origin. Outside the sphere, the general solution of the Debye-Hückel equation (3.23) cannot match with the asymptotic condition for the imposed electric field $\phi_> \to Er\cos\theta$ as $r \to \infty$. This is because an imposed static electric field drives an ionic current. Instead, what we should be considering is a high frequency electric field such that ions only move in response to the local dipole orientation but not in response to the field itself. Thus we posit that the general solution outside the sphere is

$$\phi_> = \left[C_1' k_l(\kappa r) + D_1' r\right] \cos\theta. \tag{3.34}$$

By matching the solution as $r \to \infty$ to the imposed external electric field, we have $D_1' = E$.

As there are no free surface charges, the components of the electric field must be continuous. Applying boundary conditions (3.25) and (3.24) to (3.33)–(3.34), we obtain

$$B_1' = \frac{3\epsilon E((\kappa a_d)^2/3 + \kappa a_d + 1)}{(2\epsilon + \epsilon_\infty)(1 + \kappa a_d) + \epsilon(\kappa a_d)^2}, \tag{3.35}$$

and

$$C_1' = \frac{a_d^3 \kappa^2 e^{\kappa a_d}(\epsilon - \epsilon_\infty)}{(2\epsilon + \epsilon_\infty)(1 + \kappa a_d) + \epsilon(\kappa a_d)^2}. \tag{3.36}$$

Physically, B_1' is the field in a dielectric sphere induced by an electric field (the so-called "cavity field"), and C_1' is the response of the medium to the dielectric sphere. Effectively, the presence of an electric field induces a dipole moment

$$m' = \nu(E_{\text{cavity}} + Rm') = \nu(cE + Rm'), \tag{3.37}$$

where

$$c = \frac{3\epsilon((\kappa a_d)^2/3 + \kappa a_d + 1)}{(2\epsilon + \epsilon_\infty)(1 + \kappa a_d) + \epsilon(\kappa a_d)^2}. \tag{3.38}$$

Thus the electric field-induced dipole moment (pointing in the opposite direction of the applied electric field) is

$$m' = \frac{\nu c}{1 - \nu R} E. \tag{3.39}$$

Now, consider a dipole in a dielectric with an applied electric field. The total dipole moment of the cavity is the sum of the contribution from the permanent dipole ($\mathbf{m}$), and electric-field induced dipole moment ($\mathbf{m}'$). Crucially, the two do not necessarily point in the same direction due to thermal fluctuations. Let θ be the angle between $\mathbf{m}$ and $\mathbf{m}'$. m_{tot}, the component of the total dipole moment antiparallel to the applied field, is

$$m_{\text{tot}} = m\cos\theta + m', \tag{3.40}$$

and the work done to rotate $\mathbf{m}$ against the applied electric field is

$$w(\theta) = -E_{\text{cavity}} m\cos\theta = -cEm\cos\theta. \tag{3.41}$$

To obtain the macroscopic response of the material to an applied electric field, we need the thermal average of m_{tot}, which is given by

$$\langle m_{\text{tot}} \rangle = \frac{\int_0^\pi \mathrm{d}\theta \; m_{\text{tot}}(\theta) \sin\theta \; e^{-\frac{w(\theta)}{k_B T}}}{\int_0^\pi \mathrm{d}\theta \; \sin\theta \; e^{-\frac{w(\theta)}{k_B T}}}. \tag{3.42}$$

Observing that

$$\langle \cos\theta \rangle = \frac{\int_0^\pi \mathrm{d}\theta \; \cos\theta e^{-\frac{w(\theta)}{k_B T}}}{\int_0^\pi \mathrm{d}\theta \; \sin\theta \; e^{-\frac{w(\theta)}{k_B T}}} = \coth\left(\frac{cEm}{k_B T}\right) - \frac{k_B T}{cEm} \approx \frac{3mc}{k_B T} E + O\left(\left(\frac{mcE}{k_B T}\right)^2\right), \tag{3.43}$$

we arrive at

$$\langle m_{\text{tot}} \rangle = \frac{c}{1 - \nu R}\left[\nu + \frac{\mu^2}{3k_B T(1 - \nu R)}\right] E. \tag{3.44}$$

We note that considering E as asymptotically small in Equation (3.43) is justified as the dielectric constant is fundamentally a linear response quantity. Finally, noting that the total polarisation is simply $P = N\langle m_{\text{tot}} \rangle$, and the classical relation between polarisation and electric field

$$\frac{\epsilon-1}{4\pi}E = P, \tag{3.45}$$

we arrive at an equation for ϵ (note that the RHS is dependent on ϵ through R in (3.31), and so the relation is implicit)

$$\frac{\epsilon-1}{4\pi} = N\frac{c}{1-\nu R}\left[\nu + \frac{\mu^2}{3k_BT(1-\nu R)}\right]. \tag{3.46}$$

After some algebra and making use of the classical Clausius–Mossotti relation

$$\nu = \frac{\epsilon_\infty^2 - 1}{\epsilon_\infty^2 + 2}a_d^3, \tag{3.47}$$

we can rearrange Equation (3.46) into

$$\frac{(\epsilon-\epsilon_\infty)[(2\epsilon+\epsilon_\infty)(1+\kappa a_d)+\epsilon(\kappa a_d)^2]}{\epsilon(\epsilon_\infty+2)^2(1+\kappa a_d+(\kappa a_d)^2/3)} = \frac{2\pi}{9}\frac{(1-\alpha)\rho\mu^2}{k_BT}, \tag{3.48}$$

Equation (3.48) is the central result of this Section. It expresses the macroscopic dielectric constant in terms of microscopic quantities.

Clearly, the derivation of Equation (3.48) contains several assumptions. The most important of these is the mean-field treatment of ion-ion and ion-dipole electrostatic correlations using Debye–Hückel theory; dipole-dipole correlations are also treated in a mean field manner by introducing a self-consistently determined "reaction field". However, this assumption is consistent with our modelling framework: ion-pairs are corrections to mean-field theory, hence we would be double counting the contribution of ion-pairs if a mean-field approach was not used. Another crucial approximation is assuming that dipoles are spheres, and neglecting any steric correlations between ions and dipoles. We believe that steric effects will likely only modify the quantitative results of the model as any ion-pairing is primarily driven by electrostatic attraction.

For the remainder of this Chapter we shall, for simplicity, assume that the volume of the ion pair is equal to the sum of the individual ionic volumes, so that $a_d = 2^{1/3}a$ and $\mu = ea_d/2 = ea/2^{2/3}$.

3.2.4 The Extent of Association

Substituting Equation (3.18) into the left hand side of (3.3), and using (3.16), we arrive at an implicit equation for α, the fraction of ions that are dissociated

$$\frac{1-\alpha}{\alpha^2} = 2\pi\rho a^3 \int_1^\infty r^2 \left[\exp\left(\frac{l_B}{ar}\frac{e^{\kappa a(1-r)}}{\kappa a+1}\right) - 1\right] \mathrm{d}r. \tag{3.49}$$

with α implicit in the right hand side of (3.49) via (3.5) and (3.48) (since l_B is a function of ϵ via (3.5) and that ϵ is a function of α via (3.48)). Here, we have redefined the variable $r \to r/a$ to emphasise the important dimensionless parameters κa and l_B/a.

Equation (3.49) is the main result of our model and contains no fitting parameters. The only experimental measurements needed are the density ρ, ion diameter a, and high frequency dielectric constant ϵ_∞. The ion diameter a is difficult to assess experimentally, not least because cations and anions are seldom truly spherical let alone the same size (recall that this asphericity was one of the reasons that ionic liquids stay liquid at room temperature). Nonetheless, one can estimate an effective ion diameter by noting that the packing fraction $\eta = (\pi/6)\rho a^3 \approx 0.64$ for randomly packed spheres (Bernal and Mason, 1960); we shall subsequently investigate the effect of varying η and find that the results are not sensitive to the precise value of the packing fraction used. We note that the packing fraction of ionic liquids is roughly constant independent of the chemistry (Slattery et al., 2007). In fact, the key dimensionless parameter is κa, which can be written in terms of η and another dimensionless parameter l_B/a via $\kappa a = \sqrt{24\eta\alpha l_B/a}$ (*c.f.* Equation (3.19)). It is therefore not necessary to estimate α directly.

The high frequency dielectric constant ϵ_∞ can be estimated using molecular polarisabilities or the refractive index. However, recent work (Weingärtner, 2013) suggests that ϵ_∞ for an ionic liquid is greater than that predicted via the polarisability/refractive index route (*c.f.* Equation 3.47), indicating another high-frequency mode for dielectric relaxation possibly due to the vibrations of hydrogen bonds (Fumino et al., 2008). To take these internal degrees of freedom into account, we take $\epsilon_\infty = 3.5$ as a typical estimate (see *e.g.* Daguenet et al., 2006; Nakamura and Shikata, 2010).

Figure 3.4a shows that the experimentally measured values of the dielectric constants of several common ionic liquids are quantitatively in agreement with the theoretically predicted values. This demonstrates that the thermodynamic framework developed here is physically reasonable. Figure 3.4a also shows the general dependence of the dielectric constant on the ionic size a. Increasing the effective ionic radius decreases the density of dipoles and hence decreases the dielectric constant. We note that this picture only holds for ionic liquids with short pendant alkyl chains, and is not valid for ionic liquids with longer side chains and polymerised ionic liquids, where locally heterogeneous environments emerge (Bhargava et al., 2007; Triolo et al., 2007; Xiao et al., 2009). This local microstructuring promotes ion pairing and correlations between the ion pairs, thus increasing the dielectric constant (Choi et al., 2013).

Numerical solution of (3.49) shows that α is relatively insensitive to the ion radius and packing fraction (see Figure 3.4b). To understand why this is, we note that in the limit

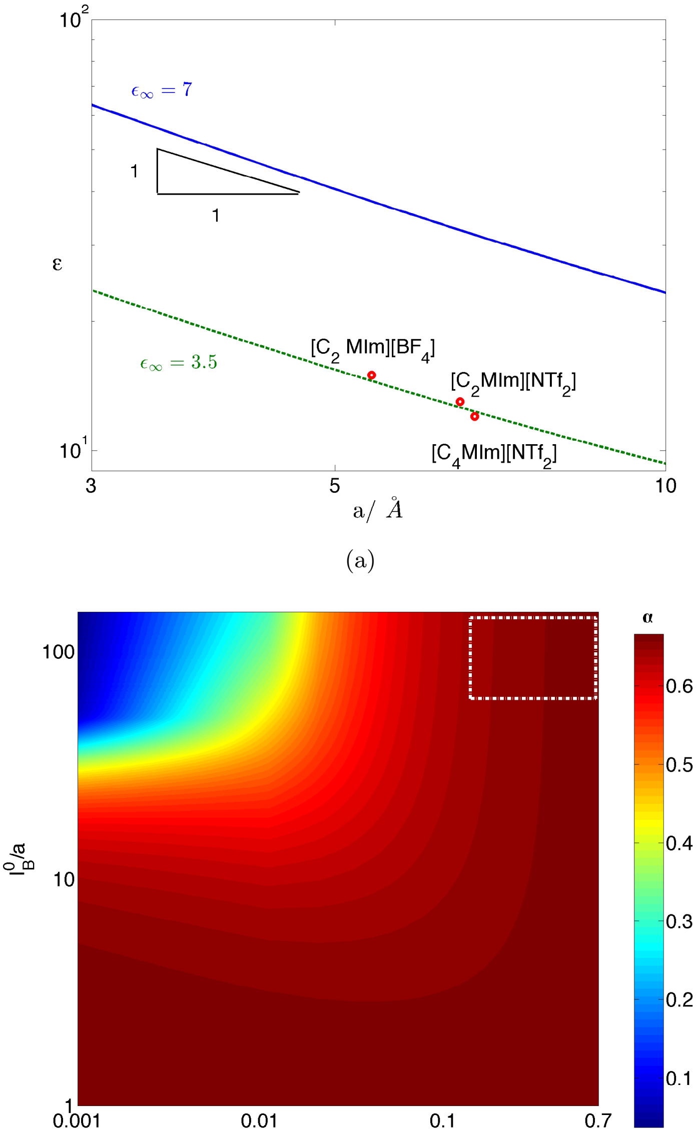

(a)

(b)

Figure 3.4: *a) The dielectric constant as a function of ion diameter plotted for different high frequency dielectric constants* ϵ_∞*. The datapoints show the experimentally obtained values taken from (Stoppa et al., 2010) (*$[\mathrm{C_2MIm}][\mathrm{BF_4}]$*), (Huang et al., 2011) (*$[\mathrm{C_3MIm}][\mathrm{NTf_2}]$*), and (Weingartner, 2006) (*$[\mathrm{C_4MIm}][\mathrm{NTf_2}]$*). The ion diameter is calculated from the density of the ionic liquids taken from (Zhang et al., 2009), assuming the packing fraction* $\eta = 0.64$*. b) The fraction of free ions,* α*, as a function of packing fraction* η *and unscreened electrostatic interaction at closest contact* l_B^0/a*. The white box in the inset shows the largest possible parameter space for a reasonable ionic liquid: ion diameter* $5\AA$*-*$10\AA$ *and density* $\rho = 4 \times 10^{27}\ \mathrm{m}^{-3} (\approx 6M)$*.*

$\kappa a \gg 1$, the integrand in Equation (3.49) can be expanded using Taylor series

$$\exp\left(\frac{l_B}{ar}\frac{e^{\kappa a(1-r)}}{\kappa a+1}\right)-1 \approx \frac{l_B}{ar}\frac{e^{\kappa a(1-r)}}{\kappa a+1}, \quad r>1 \tag{3.50}$$

so that

$$\int_1^{\infty} r^2\left[\exp\left(\frac{l_B}{ar}\frac{e^{\kappa a(1-r)}}{\kappa a+1}\right)-1\right]\,\mathrm{d}r \approx \frac{l_B}{a}(\kappa a)^{-2} = \frac{1}{24\eta\alpha}. \tag{3.51}$$

The transcendental equation (3.49) can then be solved asymptotically, yielding $\alpha \approx 2/3$. This agrees well with numerical results in Figure 3.4b. The leading order expansion (3.48) for $\kappa a \gg 1$ yields

$$\epsilon \approx \frac{4\eta(\epsilon_\infty+2)^2}{27}\frac{l_B^{(0)}}{a}, \tag{3.52}$$

where $l_B^{(0)}$ is the vacuum Bjerrum length (when $\epsilon = 1$). We thus see that the dielectric constant scales inversely with the ionic radius, in agreement with the numerical solution of the full problem (Figure 3.4a).

Our main result is that $\alpha \approx 2/3$, *i.e.* almost 2/3 of ions are *not* bound in ion pairs in a typical ionic liquid at any instant, and, further, that $\kappa a \gg 1$ — the Debye length is small, contrary to previous results (Gebbie et al., 2013a). Although Coulomb interactions in free space are strong and long-ranged, the presence of other free ions significantly screens these interactions. Figure 3.4b shows that the result $\alpha \approx 2/3$ is robust for the whole parameter space that is physically relevant for ionic liquids. The only parameter regime in which ions are strongly bound in ion pairs, and hence $\alpha \ll 1$, is for small ions at low packing fraction. In this regime, the system is closer to a dilute gaseous plasma-like system than an ionic liquid.

At this point, we should comment on several key assumptions of our model: (*i*) The mean-field linearised Poisson-Boltzmann treatment neglects fluctuation effects, which would renormalise the screening length and, for large electrolyte densities, induce an oscillatory decay in the electric potential away from the ion (Attard, 1996). This subtlety is likely to affect the quantitative predictions of our theory, but not our qualitative conclusions as we have accounted for strong electrostatic correlations beyond mean field by considering bound ion pairs. (*ii*) The estimate of the dielectric constant, (3.48), uses a mean-field treatment of dipole-dipole interactions, and linearised Poisson-Boltzmann electrostatics (consistent with our treatment of ion-ion interactions). (*iii*) The calculation of the equilibrium constant is based on McMillan-Mayer theory of an associating solution. The physical picture is that we correct the non-ideality of the ion mixture by introducing dipolar ion-pairs, and Equation (3.16) comes from a self-consistent evaluation of the virial coefficients (Woolley, 1953). Various other approaches have been proposed in the literature (Levin and Fisher, 1996; Holovko, 2005; Schröer, 2011), with various theories differing in their the thermodynamic definition of an “ion pair”; these theories, however, yield qualitatively similar results for our model system. (*iv*) We have only considered ions and ion-pairs here. Interactions between higher order multipoles are weaker. Therefore the fact that ion-pairs are not abundant means that the effects of larger aggregates is likely to be negligible. (*v*) Ionic liquids are typically geometrically anisotropic and have short ranged directional interactions such as hydrogen bonds. We have neglected those factors here as they are secondary in the formation of ion pairs.

3.3 Lifetime of an Ion Pair

It is important to bear in mind that an ion pair is only a transient species — ions can dissociate and form an ion pair with another surrounding ion. Therefore, another natural measure of whether ionic liquids are dilute electrolytes is the lifetime of an ion pair. Assuming random packing, the average distance between one ion in an ion pair and another ion of opposite charge is approximately $\sigma = 2[3/(4\pi\rho)]^{1/3}$. For an ion pair to ‘break’, one ion must move away from the pair. In doing so, the electrostatic energy increases before the ion passes through a “transition state” energy maxima, after which it forms a new ion pair. The energy landscape as the ion moves away from its existing partner and towards an adjacent ion is given by

$$V(r) = u(r) + u(\sigma - r + a), \tag{3.53}$$

where $u(r)$ is the interionic interaction defined by Equation (3.18) and r is the separation between the original ion pair (see Figure 3.5a). The lifetime of an ion pair is the mean first passage time through the energy maxima at $r = (\sigma + a)/2$, and can be estimated using Kramers-Smoluchowski theory to be (Hänggi et al., 1990)

$$\tau = \frac{1}{D} \int_{(\sigma+a)/2}^{\sigma} \mathrm{d}x \int_{a}^{x} \mathrm{d}y \, \left(\frac{y}{x}\right)^2 \exp\Big[V(x) - V(y)\Big], \tag{3.54}$$

where D is the ion self-diffusion coefficient (which is tabulated in the literature, see Table 3.1). Table 3.1 shows that the estimated lifetimes of the ion pairs in typical ionic liquids are relatively short and comparable to the diffusion timescale $\tau_D = a^2/D$.

Further insights can be obtained by writing (3.54) in dimensionless form

$$\tau/\tau_D = \mathfrak{p}\left(\frac{a}{l_B}, \kappa a\right) \tag{3.55}$$

Ionic Liquid Ions	$D/10^8 m^2 s^{-1}$	$a/\AA$	τ/ps	$\mathfrak{p} = \tau/\tau_D$
$[C_2MIm][BF_4]$	1.6 (Noda et al., 2001)	5.4	140	7.7
$[C_3MIm][NTf_2]$	1.2 (est. from Tokuda et al. (2005))	6.5	71	2.0
$[C_4MIm][NTf_2]$	1.2 (Tokuda et al., 2005)	6.7	63	1.7

Table 3.1: *The ion pairs have relatively short lifetimes (as estimated by (3.54)). The ion diameter is estimated from the packing fraction, as outlined in the main text.*

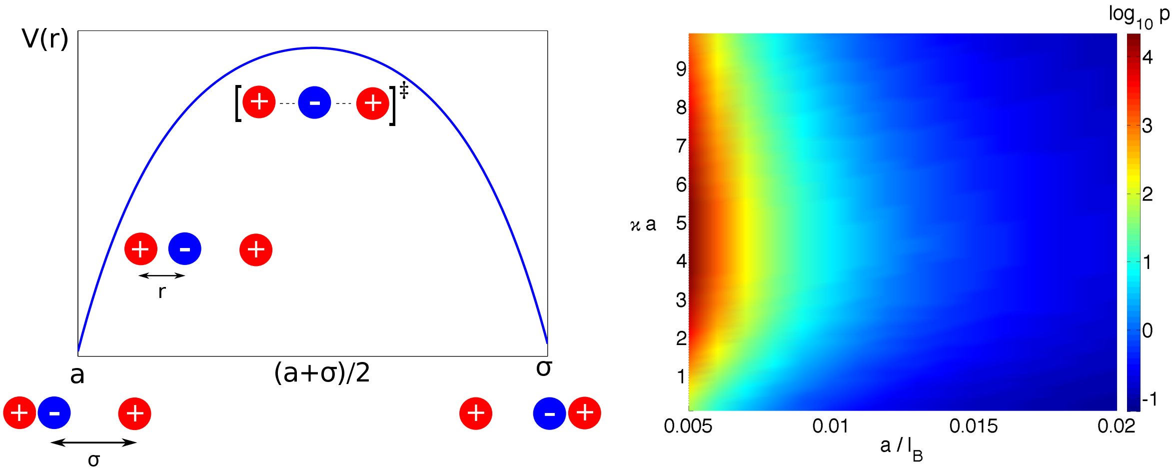

(a)

(b)

Figure 3.5: *a) Schematic cartoon illustrating the energy landscape of the ion pair exchange. b) The scaling function, $\mathfrak{p}$, plotted for the two dimensionless lengthscales κa and a/l_B.*

where $\mathfrak{p}$ is a cumbersome quadrature that depends on two dimensionless lengthscales. Figure 3.5b shows that, for fixed ion size, $\mathfrak{p}$ decreases as the dielectric constant, and thus a/l_B, increases. However, surprisingly, $\mathfrak{p}$ increases before decreasing as the Debye length decreases. Decreasing the Debye length decreases the magnitude of the electrostatic interactions, but the energy barrier $\Delta E = V((R+a)/2) - V(a)$ is a non-monotonic function of κa. The initial increase in the energy barrier as κa increases is due to the effect of screening decreasing $V(a)$, but to a lesser extent the energy maximum at $V((R+a)/2)$. For larger κa all interactions are strongly screened and therefore ΔE decreases. Increasing the ion diameter a whilst keeping the Debye and Bjerrum lengths fixed leads to a decrease in the lifetime due to the reduction of surface charge density on the ion surface.

3.4 Conclusion

The simple model developed here captures the essential physics of ion-ion, ion-dipole and dipole-dipole interaction in determining the abundance of ion pairs in ionic liquids. Despite its simplicity, the theory agrees well with experimental measurements of the dielectric constant. Crucially, our theory predicts that free ions outnumber ion pairs by 2 : 1 with pairs being short-lived. This suggests that ionic liquids cannot be considered as dilute electrolytes. As such, in the remainder of this thesis, we shall, for simplicity, ignore the effect of ion pairing.

On the experimental front, we note that the good quantitative fit obtained by Gebbie et al. (2013a) that supported the dilute electrolyte picture may be an artefact of the surface morphology and interfacial chemistry of gold. It is known that the gold surface is not atomically flat and surface reconstruction occurs upon contact with ionic liquids (Aliaga et al., 2007; Uhl et al., 2013). In fact, other surface force balance studies (Perkin et al., 2010; 2011) seem to indicate a very high degree of Coulomb correlations. Therefore, more experimentation is required to conclusively establish whether ionic liquids should be viewed as dilute electrolyte.

Chapter 4

Ionic Liquids Under Nanoconfinement

Synopsis

The confinement of an ionic liquid between charged solid surfaces is treated using an exactly solvable 1D Coulomb gas model. The model highlights the importance of two dimensionless parameters in determining how the disjoining pressure exerted on the solid surfaces depends on the geometrical confinement. These parameters are the fugacity of the ionic liquid (related to cohesive energy of the bulk ionic liquid), and the electrostatic interaction energy of ions at closest approach. Our theory reveals that thermodynamic fluctuations play a vital role in the "squeezing out" of charged layers as the confinement is increased. With all parameters independently estimated without fitting, the model provides a good qualitative account of previous experimental data.

A paper based on some of the work described in this chapter has been published in the *Journal of Chemical Physics.* (Lee et al., 2014c)

4.1 Introduction

In several important nanotechnological applications, including nanoporous supercapacitors and lubricants for microelectromechanical devices, ionic liquids are under severe geometric confinement between charged surfaces (see Section 1.1). In Chapter 3 we saw that ionic liquids should be considered to be concentrated electrolytes. Therefore, the behaviour of ionic liquids under confinement is complicated by the very strong ion-ion correlations that cannot be accounted for via classical Poisson-Boltzmann theory (*c.f.* Section 2.2).

Previous studies have focused on the effect of strong electrostatic correlations on a semi-infinite electrode-electrolyte interface, and how these correlations behave far from the interface as the bulk ionic liquid is approached. Experiments (*e.g.* Alam et al., 2007a;b; 2008; Islam et al., 2008; Lockett et al., 2008), theories (*e.g.* Eigen and Wicke, 1954; Borukhov et al., 1997; 2000) and simulations (Esnouf et al., 1988; Lamperski and Kłos, 2008; Trulsson et al., 2010; Vatamanu et al., 2010; Fedorov et al., 2010; Hu et al., 2013; Merlet et al., 2013b) have shed light on the structure of bulk ionic liquids near charged surfaces. These works have revealed the effect of ion size in determining the interfacial capacitance, and established that there is a region of closely packed ions near a highly charged surface, followed by a gradual (potentially oscillatory) decay of ion density into the bulk.

Analysis of the long-distance asymptotics of the direct correlation function obtained by the Ornstein-Zernicke equation reveals that the density-density and charge-charge correlation functions decay exponentially with or without an oscillatory component (Attard, 1993; Leote de Carvalho and Evans, 1994; Attard, 1996). Increasing the ion density (or chemical potential) at fixed temperature causes a crossover from monotonic exponential decay of both charge-charge and density-density correlation functions to a damped oscillatory decay of the charge-charge correlation function. A further increase in density triggers the density-density correlations to decay in a damped oscillatory manner.

The oscillatory decay of charge-charge correlations can be rationalised as the result of a competition between the long-ranged ion-ion Coulomb interactions and the steric constraint of packing counterions around the central ion. This causes the ionic atmosphere near the ion to overcompensate the bare ion charge. Crossover from monotonic to oscillatory decay of the density-density correlation function is induced by increased steric correlation as the ion density increases, and is also reported in simple square-well fluids (Fisher and Widom, 1969; Evans et al., 1993). This is known in the context of single-component fluids as the Fisher-Widom transition. Experimentally, X-ray reflectivity (Mezger et al., 2008) and AFM (Hayes et al., 2009) measurements showed an oscillatory decay of charge density away from a highly charged interface; this is corroborated by a recent analytical solution of a 1D lattice Coulomb gas model of ionic fluids (Démery et al., 2012a;b).

The behaviour and structure of severely confined ionic systems are more intricate than these bulk-like systems. Recent surface force balance experiments by Perkin et al. (2010; 2011) demonstrated that the disjoining pressure across a nanometre-thick ionic liquid film confined between two (negatively charged) atomically flat mica surfaces increases in an oscillatory manner as the separation between surfaces decreases (see Figure 4.1 for a schematic representation of these experiments and the typical results). In these experiments, the slit pore is submerged in a bath of ionic liquid. The peaks in the disjoining pressure were attributed qualitatively to squeezing out of layers of ions close to the interface, with the position of the peak being an indicator of the ion radii. To maintain electroneutrality, the system squeezes out layers of pairs of ions. The position of the peak with the smallest separation in those experiments corresponds roughy to the width of the ions, as would be expected on steric grounds. However, the subsequent peaks are much broader and are located further away from integer multiples of the ion radii (*c.f.* Figure 2.3). This suggests that one must move beyond a simple qualitative geometric description to understand the behaviour of a confined ionic liquid. In particular, how thermodynamic fluctuations and strong electrostatic correlations affect the disjoining pressure in systems under severe geometric confinement has not been elucidated theoretically. Here, we aim to fill this gap.

Although the pioneering work on semi-infinite electrode-electrolyte interfaces forms a basis for the general understanding of strongly correlated Coulomb systems, we stress that the oscillatory disjoining force observed in a geometrically confined ionic liquid has a very different physical origin, and should not be conflated with the oscillatory density-density and charge-charge correlation functions observed in the semi-infinite case. Rather, molecular layering of ions close to the charged surface, and the squeezing out of these molecular layers from the slit as the surface separation decreases are the crucial aspects of this intrinsically nanoscale phenomenon.

In this Chapter, we develop a novel and exactly solvable theory of the disjoining pressure in a nanoconfined ionic liquid by considering the system as a 1D Coulomb gas with hard core repulsion. In experimentally relevant systems, the separation between the charged surfaces (O(nm)) is much smaller then the typical lateral lengthscale (O(cm)). The highly charged surface promotes ordering of anions and cations into slabs, and motivates treating the system as an 1D collection of charged slabs rather than a 3D system. Our model reproduces the full range of experimentally observed physical phenomenology, and highlights the key roles that the fugacity and the strength of electrostatic interactions play in determining the disjoining pressure.

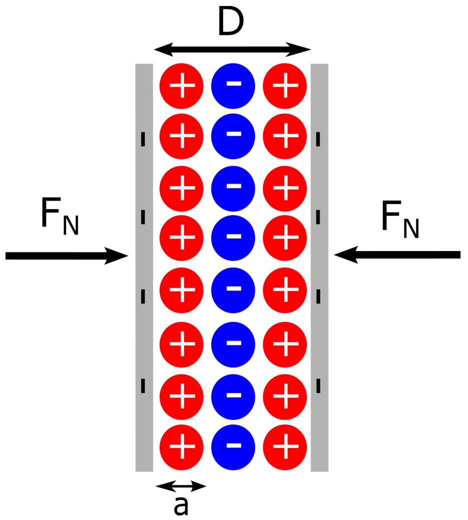

(a)

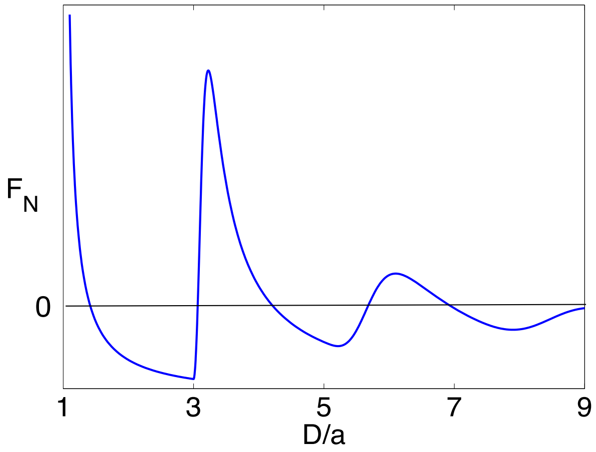

(b)

Figure 4.1: *Cartoon of the surface force balance experiments performed by Perkin et al. (2010; 2011): Panel (a) shows the layering structure of an ionic liquid confined between charged surfaces as well as the force, F_N, required to impose a given plate separation D; (b) shows a cartoon of the typical dependence of the normal force on the surface separation. See Figure 2.3 for an experimentally measured surface force profile.*

4.2 The Model

We consider a 1D system of hard slabs of width a (physically corresponding to the ion diameter) and fixed charges $\pm\sigma$. This system is confined between rigid charged surfaces with surface charge density $-q\sigma$ each and coupled to a bath of bulk ionic liquid. To ensure overall electroneutrality, the sum of the total charge of the slabs must equal $-2q\sigma$ (see Figure 4.2). As such, q must be a half integer or integer — this technical restriction is due to neglecting fluctuations in the surface charge density.

In this model, we neglects the lateral fluctuations within a slab of ion. Lateral fluctuations will generate an entropic repulsion akin to the entropic repulsion observed in fluid membranes (Helfrich and Servuss, 1984; Richetti et al., 1990). This repulsion is only felt between adjacent layers of ions, and thus will likely modify the quantitative behaviour of squeezing out of layers of ions and the force-displacement curve. For simplicity, we only consider the long-ranged electrostatic interactions here.

The thermodynamic properties of a 1D Coulomb gas without hard-core exclusion have been studied extensively by Lenard (1961); Edwards and Lenard (1962). Excluded volume effects have been accounted for by restricting ions to lie on a lattice (Démery et al., 2012a;b). This lattice Coulomb gas model, whilst revealing important qualitative insights for the arrangement of ions, presents artefacts due to the discrete nature of the lattice. This is particularly prevalent in the strongly confined limit, where there are only a few lattice sites and treating the positions of each ion as a discrete variable has the rather unphysical consequence that the disjoining pressure is only defined for discrete surface separations. Here, we remove this restriction, considering instead a Coulomb gas in which the position of each slab is a continuous variable subject to hard-core exclusion.

In 1D, the dimensionless electrostatic interaction energy, $v_{ij}(r)$, between 2 slabs separated by a centre-to-centre distance r takes the form

$$\beta v_{ij}(r) = \begin{cases} -\Xi S_i S_j |r| & |r| \geq 1 \\ \infty & |r| < 1, \end{cases} \tag{4.1}$$

(see Démery et al., 2012a) where $\beta = 1/(k_B T)$, S_i and S_j can take values ± 1 (with $+/-$ corresponding to cation and anions), the lengthscales are non-dimensionalised with respect to the ion diameter a, and the electrostatic parameter

$$\Xi = \beta \frac{\sigma^2 A a}{\epsilon} \tag{4.2}$$

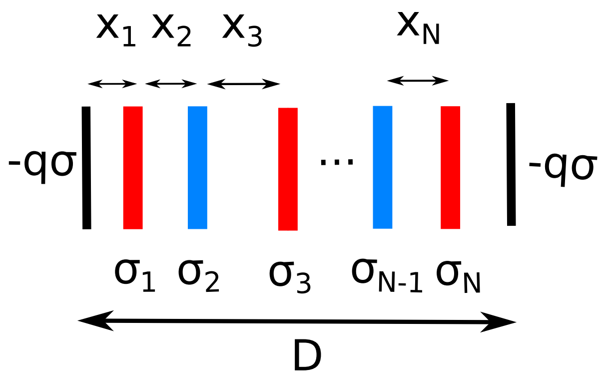

Figure 4.2: *Schematic of the 1D Coulomb system. Hard slabs of charge* $\pm\sigma$ *(cations and anions denoted in this schematic by red and blue respectively) are confined within a slit width* D*. The charge on each of the walls that make up the slit is* $-q\sigma$*.*

is the electrostatic interaction energy of two slabs at closest approach measured relative to the thermal energy k_BT; here A the area of the slab and ϵ the dielectric constant of the medium.

We note that the 1D model assumes a regular and segregated arrangement of cations and anions in the direction perpendicular to the boundary. This is expected to hold when the surface is strongly charged and thus the ions closest to the surface form a densely packed cation layer, followed by a densely packed anion layer that is attracted to the cation layer, and so on. In addition, the assumption that the slabs have a fixed charge relies on small surface separation, and thus the layers are still purely cations or anions.

The canonical partition function of m cations and n anions reads

$$Q_{m,n} = \frac{1}{m!n!} \sum_{\{\sigma\}} \delta_{m-n,2q} \int_0^D \mathrm{d}r_1 ... \int_0^D \mathrm{d}r_N \; e^{-\beta \sum_{i<j} v_{ij}(r_i - r_j)}, \tag{4.3}$$

where the Kronecker delta function imposes global electroneutrality (*i.e.* $\sum_i S_i = 2q$), $\sum_{\{\sigma\}}$ denotes summing over all possible charge configurations and $r_i \in [0, D]$ denotes the position of the charges with r_0 and r_{N+1} being the positions of the charged surfaces (which are fixed), and D being the separation between the charged surfaces. The integral can be rewritten taking advantage of the fact that the slabs cannot overlap. Denoting the separation between the i^{th} and $(i+1)^{\text{st}}$ slab by x_i (see Figure 4.2), we have

$$\int_0^D \mathrm{d}r_1 ... \int_0^D \mathrm{d}r_N = \int_{1/2}^{D-(m+n)+1/2} \mathrm{d}x_1 ... \int_1^{D-\sum_{i=1}^{j-1} x_i - (m+n) + j/2} \mathrm{d}x_j ... \int_1^{D-\sum_{i=1}^{N-1} x_i - 1/2} \mathrm{d}x_N. \tag{4.4}$$

Similar rearrangement of integral has been used to evaluate the partition function of the Tonks gas, a 1D gas with only hard core interaction (Tonks, 1936).

In experimental configurations, the confined ionic liquid is in thermal equilibrium with the surrounding bulk fluid. As such, we transform the partition function in the Canonical Ensemble into the Grand Canonical Ensemble to take into account fluctuations in the number of slabs — these fluctuations correspond physically to squeezing out of ion layers. Introducing the fugacity λ, which is assumed to be the same for cations and anions, the Grand Canonical partition function reads

$$\Lambda = \sum_{m,n=0}^{\left\lfloor \frac{(m+n)a}{L} \right\rfloor} \lambda^{m+n} Q_{m,n}. \tag{4.5}$$

The fugacity is a measure of the bulk cohesive energy — the larger the fugacity is, the more dense is the bulk ionic fluid. We note that this theory can be extended easily to the case $\lambda_+ \neq \lambda_-$.

The key physical quantity of practical interest is the disjoining pressure. This can be computed from the grand canonical partition function by noting that the grand potential takes the form $F = -\beta^{-1} \log \Lambda$, and that the disjoining pressure is

$$P = -\frac{1}{A} \frac{\partial F}{\partial D}. \tag{4.6}$$

Before illustrating the typical results of the model, we briefly discuss typical parameter values for ionic liquids in a surface force balance experiment. The electrostatic parameter Ξ depends on the pairwise interaction between ions located in adjacent slabs, and thus the lateral packing geometry in the slabs. The fact that viscous liquid-like behaviour is still observed for nanoconfined ionic liquids (Bou-Malham and Bureau, 2010) suggests that the electrostatic interaction is comparable to thermal energy, thus Ξ is expected to be order unity or less, and can be estimated using tribological measurements, as discussed later. The fugacity, on the other hand, is a bulk property of the ionic liquid, and is related to bulk density and affinity of the ionic liquid to the slit. As such, we will treat it as an effective parameter and provide estimates for it via the interfacial tension in Section 4.4.

4.3 Like-Charged Interfaces

In surface force balance experiments, a film of ionic liquid is usually confined between atomically flat and negatively charged mica surfaces (*e.g.* Perkin et al., 2011; Smith et al., 2013). The normal force measured in these experiments is oscillatory, and the period of the oscillation suggests that an odd number of layers is confined between surfaces. As such, we set $q = 1/2$, *i.e.* the ions overcompensate the surface charge of the interface.

The qualitative behaviour of the dependence of the pressure on the surface separation can be seen in the narrow separation limit. The partition function for narrow separations ($1 < D < 3$), for which only one layer is sterically allowed, is

$$Q_1 = \int_{1/2}^{D-1/2} \mathrm{d}x_1 \, e^{-\frac{\Xi D}{4}} = e^{-\frac{\Xi}{4}D}(D-1). \tag{4.7}$$

Thus for this one slab system, the pressure is simply

$$\frac{P}{P_0} = \frac{1}{D-1} - \frac{\Xi}{4}, \tag{4.8}$$

where $P_0 = k_B T/aA$ is the pressure scale. The first term in Equation (4.8) originates from the entropy of confinement, while the second term is due to electrostatic interactions between the slabs. Equation (4.8) shows that $P > 0$ for small separations as the loss of translational entropy penalises confinement. However, for $\Xi > 2$, the disjoining pressure is negative for intermediate separations when the effect of electrostatic correlations dominate the effect of confinement. An expression for the disjoining pressure similar to Equation (4.8) has been obtained via a systematic perturbative expansion of the full 3D, counterion only, Coulomb gas in the limit of highly charged surfaces (strong-coupling electrostatics) (Netz, 2001; Naji et al., 2013). There, the partition function is dominated by single-particle contributions from the interaction between counterions and charged surfaces, and Ξ is replaced by the 3D generalisation $\nu = 2\pi l_B|\Sigma|$, where Σ is the electrode surface charge density.

For larger slit widths, multiple layers of ions are sterically permitted within the slit. The partition function for the multiple layers of ions can be computed analytically by evaluating the integrals in Equation (4.4) using, for example, *Mathematica*. For example, the canonical partition function for 3 layers of ions reads

$$Q_3 = \sum_S \int_{1/2}^{D-5/2} \mathrm{d}y_1 \int_1^{D-y_1-3/2} \mathrm{d}y_2 \int_1^{D-y_1-y_2-1/2} \mathrm{d}y_3 \, e^{-H(S_1,S_2,S_3)} \tag{4.9}$$

where

$$H(S_1,S_2,S_3) = \Xi\left(\frac{1}{4}D - S_1S_2y_2 - S_2S_3y_3 - S_1S_3(y_1+y_3)\right) \tag{4.10}$$

and the sum is over the configurations $(S_1,S_2,S_3) = (1,1,-1),(1,-1,1),(-1,1,1)$. Evaluating the integral, we arrive at

$$Q_3 = \frac{1}{12\Xi^3} e^{-\frac{\Xi}{4}(9D+8)} \left\{ 2\Xi^3(D-3)^3 e^{2\Xi(D+1)} + 3e^{2\Xi D}(2\Xi^2(D-3)^2 - 2\Xi(D-3)+1) - 3e^{6\Xi} \right\}. \tag{4.11}$$

The resulting expressions for the grand canonical partition function and disjoining pressure are rather cumbersome and as such we do not include them here. Figure 4.3a shows a peak in disjoining pressure as two layers enter the slit (we note that global electroneutrality requires layers to enter in positive-negative pairs). Note that the magnitude of the peaks decreases as the separation increases, reflecting the decreased thermodynamic driving force for adsorption when there are multiple layers of ions already present in the slit. The peaks are more pronounced for larger fugacities as the ionic fluid favours a densely packed configuration, and thus would fill the slit as soon as the separation exceeds the minimum width at which it is geometrically (or sterically) possible to do so. However, for lower fugacities, the peaks are broader and shift away from the minimum separation dictated by geometry. As the separation increases they become less "periodic". This suggests that directly relating the peaks in disjoining pressure measured from surface force balance experiments to ionic diameter is too simplistic — thermodynamic fluctuations play an important role in the position of those peaks, particularly at relatively large separations.

The effect of varying the electrostatic parameter Ξ is shown in Figure 4.3b. The peak in disjoining pressure becomes more pronounced as Ξ decreases, and for large Ξ the pressure becomes negative, reflecting an attractive force. Physically, this attraction occurs because in the ground state configuration of alternating positive and negative charges, which is thermodynamically favourable for large Ξ, the Hamiltonian is identically $H = \Xi D/4$ regardless of the number of slabs. Thus thermal fluctuations are the sole driving force for the insertion/removal of additional layers.

Figure 4.4 summarises the effect of varying λ and Ξ. Decreasing the fugacity shifts the first, most pronounced peak away from $D = 3$, the minimum separation for which it is geometrically possible to fit 3 layers, and the peak pressure increases concomitantly. In the limit of large fugacity $\lambda \gg 1$, the peak disjoining pressure may be approximated by the asymptotic expressions (via Taylor expansions)

$$P_{\max} \approx \begin{cases} \frac{\lambda^2}{2^{1/3}}, & \Xi \ll 1, \;\; \Xi\lambda \ll 1, \\ -\frac{\Xi}{4} & \Xi \gg 1. \end{cases} \tag{4.12}$$

The position of the first peak in disjoining pressure can also be found asymptotically to be

$$D_{\max} \approx \begin{cases} 3 + \frac{48^{1/3}}{\lambda^{2/3}}, & \Xi \ll 1, \quad \Xi\lambda \ll 1, \\ 3 + \frac{2^{4/3}}{\lambda^{2/3}} & \Xi \gg 1. \end{cases} \tag{4.13}$$

4.4 Comparison with Experiment

Figure 4.5 compares experimental data from Perkin et al. (2011) (performed on the ionic liquid $[C_4C_1Im][Tf_2N]$) with the predictions of the 1D model described here. The exper-

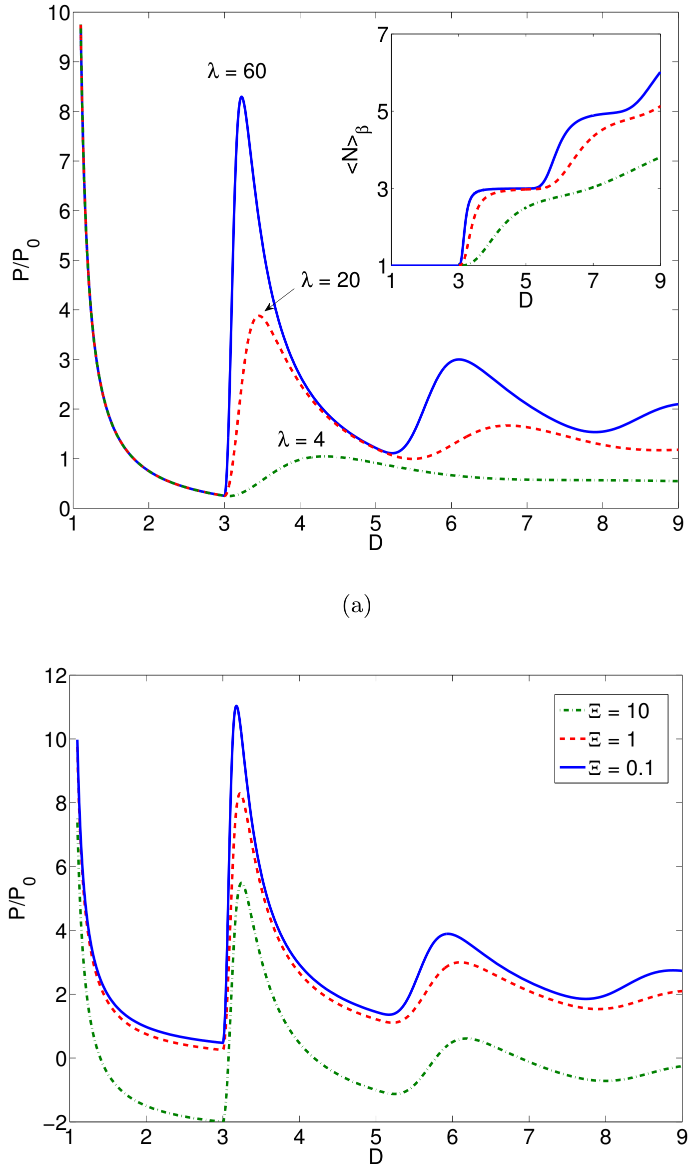

(a)

(b)

Figure 4.3: *The disjoining pressure for large fugacity shows abrupt peaks as the separation increases when ions are confined between like-charged surfaces. (a) The main panel shows the disjoining pressure plotted as a function of separation, and the inset shows the occupancy plotted as a function of separation.* $P_0 = k_BT/aA$ *is the pressure scale. (b) Decreasing the electrostatic parameter* Ξ *promotes thermal fluctuations and increases the peak pressure. The plot shows disjoining pressure as a function of separation plotted for different values of the electrostatic parameter* Ξ *for fugacity* $\lambda = 60$*.*

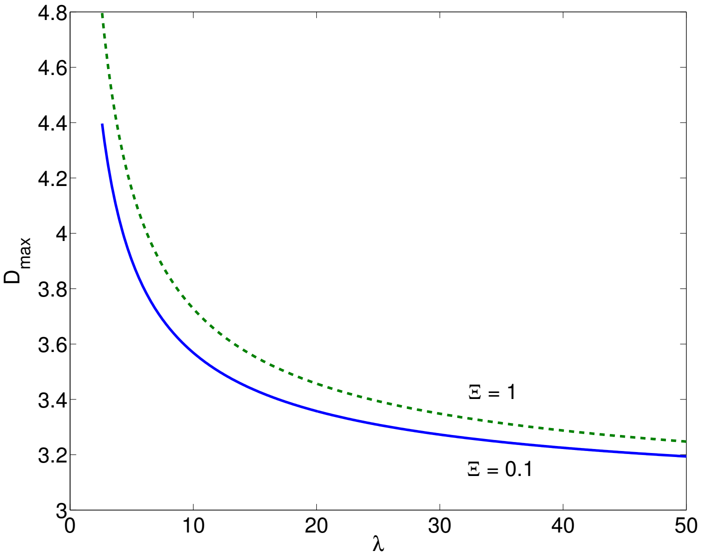

(a)

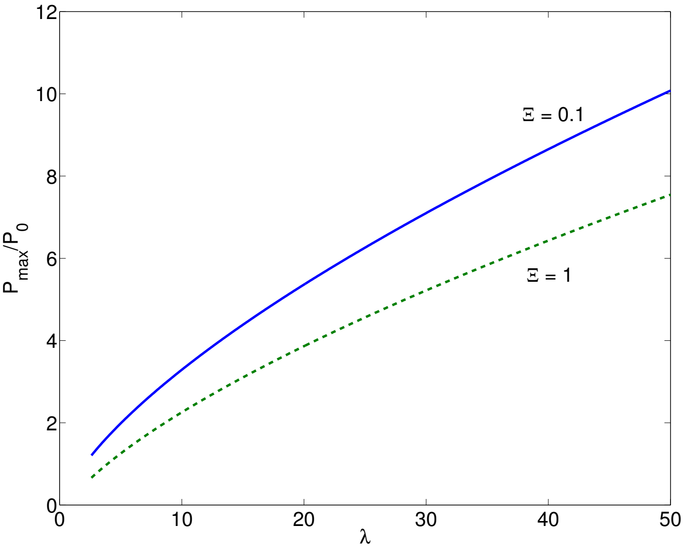

(b)

Figure 4.4: *The position and magnitude of the peak disjoining pressure as functions of fugacity for ions confined between like-charged surfaces. a) The surface separation at which the first peak in the disjoining pressure is observed moves away from* $D = 3$ *as the fugacity decreases. b) Decrease in the fugacity leads to a concomitant decrease in the magnitude of the peak pressure.*

iment is force controlled via a spring, rather than displacement–controlled assumed here for simplicity. As such, the experiment registers branches in which the gradient of the force is larger than the spring constant as attractive "jump in" or repulsive "jump-out". This explains the qualitative difference between the theory and experiment.

We also want to estimate the typical size of the parameters Ξ and λ. Direct evaluation of the electrostatic parameter Ξ via Equation (4.2) is difficult as σ and A are effective parameters that depend on the local arrangement of ions within a slab. However, the electrostatic parameter can be estimated with shear stress measurements. The yield force is the total force needed to "unlock" the slabs and allow them to slide pass each other, whereas the static friction force gives an estimate of the contribution due to geometric incommensurability between the slabs and viscous dissipation. Therefore the difference between the yield force and the static friction force, ΔF, gives the typical force scale required to overcome the Coulomb attraction and slide the layers past each other for a typical slip distance d_s. Thus the typical macroscopic Coulomb interactions between the slabs is approximately $E \sim d_s \Delta F_s$. The corresponding microscopic interaction energy scale differs by a factor of A_i/A_g, where A_g is the geometric area of the plates and A_i is the interaction area, which is less than the geometric area due to the finite radius of curvature of the system (see Figure 4.6 for a schematic drawing). We use the estimate $A_i \approx R\delta$ where R is the radius of curvature and δ is the typical surface separation, here taken as 1 nm. The typical slip length for [C_4C_1Im][Tf_2N] confined between mica surface is $d_s \sim 1$nm and the typical force $\Delta F_s \sim 1\mu$N (Smith et al., 2013), thus we have $\Xi \sim (d_s \Delta F_s/(k_B T))(A_i/A_g) \sim 0.1$.

The fugacity is rather subtle to estimate, as we would like to compute the fugacity of a *slab* of ions, not individual ions. Intuitively, the chemical potential of a slab of ions may be thought of as just the chemical potential of an ion multiplied by the number of ions in a slab. However, this is a massive overestimate as the ion-ion interaction within a slab must be accounted for. In fact, within a slab, ions are solvated (a slab comprises of both anions and cations, although not in equal proportion), and the local environment is not dissimilar to that in solution — the only difference is the a slab is charged whilst the solution is net electroneutral. As a crude approximation, we can take the chemical potential in the model as the chemical potential of an ion because the net surface charge density of a slab is of the same order of magnitude as that of an ion (Somasundaran, 2006). This chemical potential can be estimated from ionic liquid–air interfacial tension measurements. The chemical potential is the change in energy when removing a molecule from the bulk, thus it is twice the energy of transferring one molecule from the bulk to the interface where half of the interactions are deprived, *viz.* $\mu \sim 2\gamma\sigma_m$, where σ_m is the area of a "head group". Experimentally, $\gamma \approx 33.15$ mN/m (Oliveira et al., 2012). Although the cation and anion have different dimensions, an estimate based on the lowest

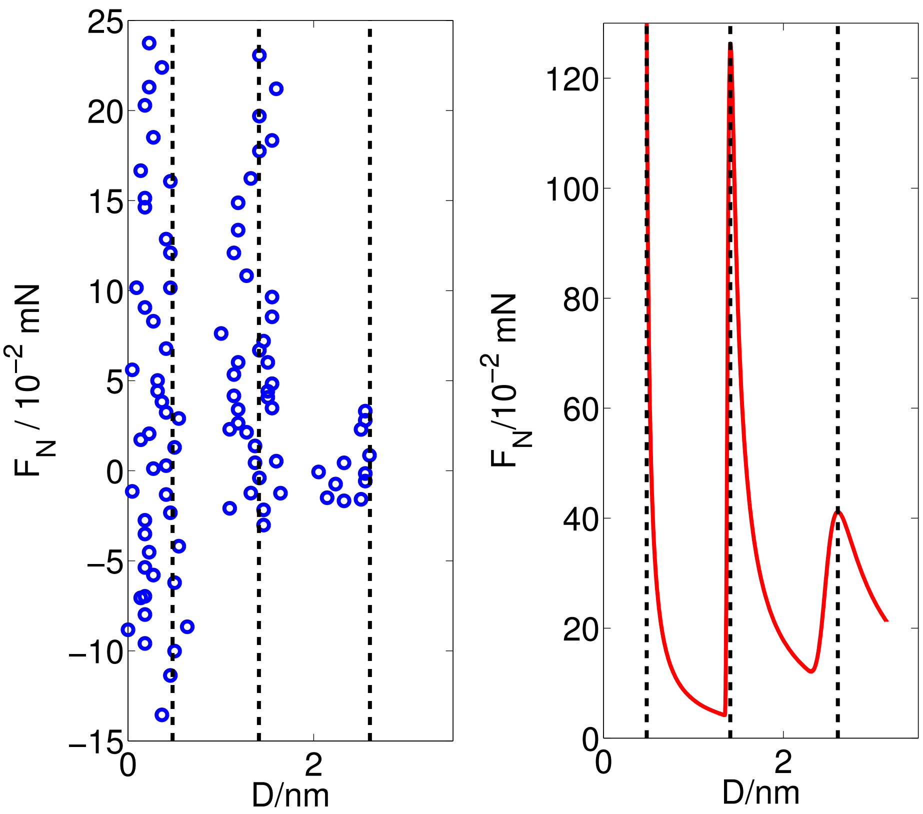

Figure 4.5: *Qualitative comparison of the normal force obtained in Perkin et al. (2011) for the ionic liquid* $[\mathrm{C_4C_1Im}][\mathrm{Tf_2N}]$ *confined between like-charged mica surfaces with the model prediction, the black dotted lines are guides to the eye (the theoretical curve diverges at* $D = a$*, see Equation (4.8)). The parameters used are:* $a = 0.45\mathring{A}$, $\lambda = 84$ *and* $\Xi = 0.1$*. We note that the microscopic force obtained by the model is scaled by* A_g/A_i *to compare with the experimental data, which is actually preformed between crossed cylinders (see Figure 4.6). The experimentally measured force is smaller in magnitude to the theoretical predictions as we neglected the bulk pressure and attractive van der Waals interactions between the mica surfaces.*

energy molecular conformation (the dimensions of the ions are obtained from Gebbie et al. (2013a)) suggests that $a_{\mathrm{cat}} = 0.35$nm for the cation and $a_{\mathrm{ani}} = 0.55$nm for the anion. Thus, as a rough guide, we take the mean and assume here that $a = 0.45$nm, therefore $\sigma_m \approx 27\mathring{A}^2$ (Gebbie et al., 2013a). Thus we arrive at the estimate $\mu = 4.4k_BT$ and $\lambda \approx 84$. We note that this estimate based on surface tension does not account for the fact that ionic liquid ions are chemically anisotropic, and preferred interactions can be maintained even when the ion is transferred from the bulk to the liquid-air interface, *e.g.* by the putting alkyl part outermost and the charged group into the liquid.

Our theory only shows the electrostatic contribution to the normal force — experimentally van der Waals interaction and the bulk pressure (as well as the entropic repulsion

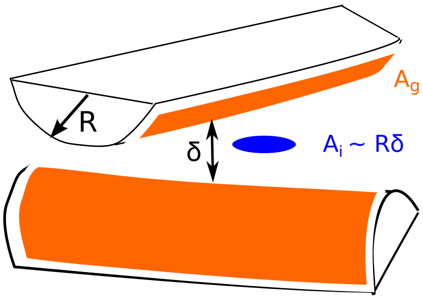

Figure 4.6: *A schematic illustration of the geometry of the crossed cylinder experimental apparatus used by Perkin et al. (2011). In particular, not the difference between the geometric area* A_g *and interaction area* A_i

neglected by treating a layer of ions as a rigid slab) are important contributions. However, the only oscillatory component of the normal force is the electrostatic interaction, thus the qualitative alignment of the peaks predicted by the theory and observed in experiment is an important justification of the theory. In addition both van der Waals and bulk pressure are attractive forces, explaining the fact that the electrostatic component of the force is more positive (repulsive) than the experimentally measured force (note that the force predicted by the theory is positive).

4.5 Oppositely-Charged Surfaces

Similar considerations apply to ionic liquids confined between oppositely charged surfaces, with surface charge $\pm q\sigma$ (see Figure 4.7 for a schematic of such system). The Coulomb gas model developed above can readily be applied. Note that here electroneutrality dictates only even number of slabs can be in the slit.

Figure 4.8 shows that the pressure is negative for small separations, corresponding to attractive interaction between the surfaces when the ions cannot effectively screen the surface charge. As is the case for like-charged surfaces, the adsorption transitions (and hence the maxima in disjoining pressure), become more pronounced as the fugacity of the ionic liquid increases.

However, contrary to the case of like-charged surfaces, the maxima in the disjoining pressure *increases* as the electrostatic parameter Ξ increases (see inset of Figure 4.8). Consider for simplicity the case of $N = 2$ (one cation and one anion layer), in which the Hamiltonian for the ground state configuration of alternating positive and negative charges reads $H_2/(k_B T\ \Xi) = -Dq^2 + y_2(2q+1)$, with y_2 the separation between the ion layers. As the Hamiltonian is linear in y_2, the extrema of the Hamiltonian are reached at

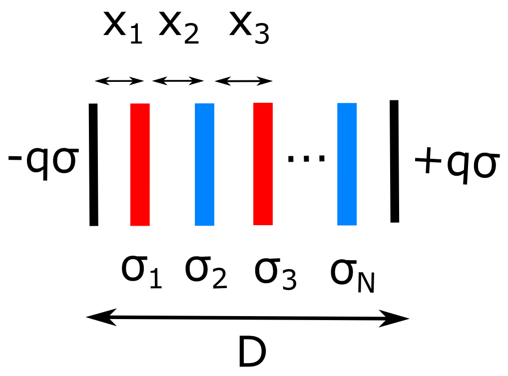

Figure 4.7: *Schematic sketch of the system: Hard slabs of charge $\pm\sigma$ (cations and anions denoted in this figure by red and blue slabs respectively) are confined within a slit of width D. The charge on each of the walls that make up the slit is $+q\sigma$ and $-q\sigma$. Note that by electroneutrality only even number of slabs can be in the slit.*

the boundaries of allowed y_2, *viz.* $y_2 = 1$ (corresponding to layers separated by the hard sphere diameter), and $y_2 = D-1$ (corresponding to layers located at the distance of closest approach to the charged surface). For $D > 2$ the minimum y_2 is attained at $y_2 = D - 1$, and ions are forced close to the surface, creating a "cavity" at the centre that promotes abrupt adsorption of another layer of ions when the slit separation geometrically allows it. This is in direct contrast to the case of like-charged interfaces, where the combined electrostatic attraction of a layer to both surfaces pushes ions to the centre of the slit.

The qualitative behaviour of the disjoining pressure is also dependent on q, the ratio between the surface charge on the charged surface and the charge on the slabs. Figure 4.9 shows that the peak disjoining pressure is low for an overcharged surface ($q > 1$), as the strong electrostatic attraction between the surfaces is not effectively screened by the intervening ions, and the thermodynamic driving force for ion entry is overwhelmed by attraction between the surfaces. For overcharged surfaces the first peak in the disjoining pressure can be lower than subsequent peaks, when more ions have entered the system to screen the interaction between the surfaces.

In the limit of small electrostatic parameter Ξ, the position of the first peak is given by

$$D_{\max} = 2 + \frac{1}{\lambda} + \frac{\Xi}{6\lambda}\left[3\lambda - 2 + 3q^2(1-2\lambda)\right] + O(\Xi^2). \tag{4.14}$$

Thus increasing surface charge shifts the peak to larger separations, as the surface-surface attraction favours small surface separation (note that when $\lambda < 1/2$, the first peak is located outside of the range $2 < D < 4$).

We note that q in this 1D model is an effective parameter — physically it depends on the electrostatic interactions within a slab, which is averaged out in this model. Experimentally for large monovalent ions and highly charged surfaces, surface charge cannot be

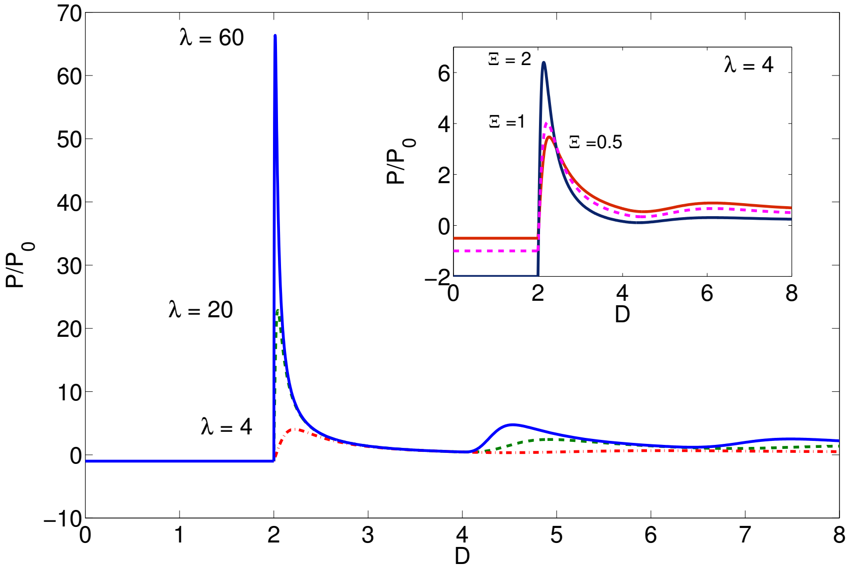

Figure 4.8: *The disjoining pressure as a function of separation for oppositely charged surface with* $q = 1$ *and* $\Xi = 1$*. The inset show the dependence of the pressure on the electrostatic parameter* Ξ*.*

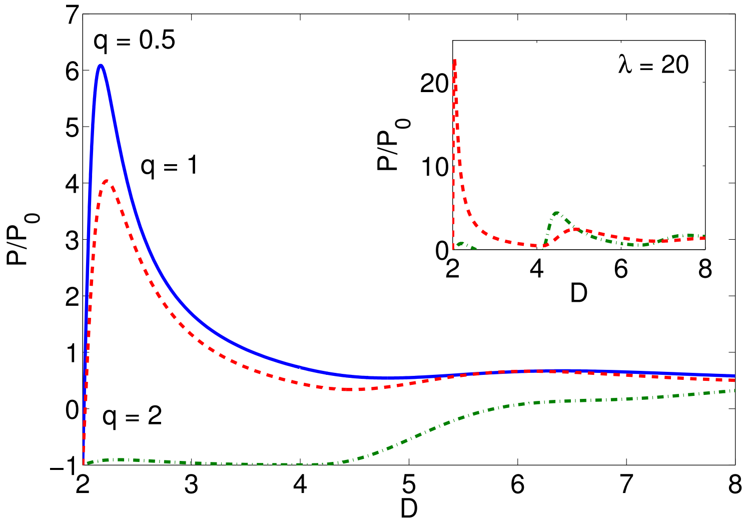

Figure 4.9: *The qualitative features of the disjoining pressure for ions confined between oppositely charged surfaces depends on whether the surfaces are overcharged* ($q > 1$) *or undercharged* ($q < 1$)*. The main panel shows results with fugacity* $\lambda = 4$*, and the inset shows* $\lambda = 20$*.*

completely neutralised even when the layers are laterally close packed, thus $q > 1$. On the other hand, for small ions or sparingly charged surfaces, ions can arrange themselves to form layers that completely neutralise or even overcompensate the surface charge, thus $q \leq 1$. Therefore the qualitative form of the disjoining pressure is an effective way to interrogate not only the layered organisation of ions in the direction perpendicular to the surface, but also the lateral structure within the layer in the direction parallel to the surface.

4.6 Conclusion

We have considered the equilibrium properties of an ionic liquid confined between charged surfaces using a 1D Coulomb gas model. The theory reveals the roles of all physical parameters, but most importantly they group themselves into two dimensionless parameters: the fugacity of the bulk fluid λ and the electrostatic parameter Ξ. These two parameters have clear constituents, and can be independently measured or estimated.

The model shows that the disjoining pressure decays in an oscillatory manner with the separation between surfaces. The maxima of these oscillations correspond to the entering of discrete "layers" of ions, and become more pronounced as the fugacity increases. For like-charged surfaces, the peak disjoining pressure decreases with increasing electrostatic parameter as the ground state Hamiltonian is independent of the number of layers in-between the surfaces. The theory is in good qualitative agreement with experimental data on [C_4C_1Im][Tf_2N] confined between mica surfaces, with all parameters independently estimated without fitting.

For oppositely charged surfaces, the theory predicts that increasing the electrostatic parameter increases the peak disjoining pressure. Ions are pulled close to the charged surfaces, creating a "cavity" at the centre of the slit that allows adsorption of ions from the bulk. The electrostatic parameter can be varied by altering the effective ion radius and the charge on the ionic liquid ions. Experimental studies with atomically flat, oppositely charged surfaces are currently scarce. We hope that our model will motivate further experimental and computational studies.

Chapter 5

Energy Storage via Confined Ionic Liquids

Synopsis

Nanoporous supercapacitors are an emerging player in the field of energy storage that can fill the gap between dielectric capacitors and batteries: dielectric capacitors have large power densities but relatively low energy densities, whereas batteries have the opposite properties. The key issue hindering the development of supercapacitors is the perceived tradeoff between capacitance, power delivery, and reversibility: a trilemma. Current efforts to boost the capacitance of nanoporous supercapacitors focus on reducing the pore size so that they can only accommodate individual ions. However, this reduction compromises the charging dynamics. We show via an analytical theory that charging is sensitively dependent on the affinity of ions to the pores. Moreover, and contrary to conventional wisdom, the capacitance of ionophobic pores can be maximised at pore widths significantly larger than the ion diameter. Our theory also predicts that charging can be irreversible with a significant energy loss per cycle for intermediate ionophilicities. We use these observations to explore the parameter regime in which the capacitance-power-hysterisis trilemma may be resolved.

5.1 Introduction

The physics of charge storage at the nanoscale has received significant attention in recent years due to its relevance for efficient energy storage and the development of novel green technologies (Lu et al., 2013; Simon and Gogotsi, 2013; 2008). In particular, great effort has been channeled into studying electrical double layer capacitors in which energy is stored at the electrode-electrolyte interface.

Unlike conventional dielectric capacitors where energy is stored by the polarisation of a dielectric medium, electrical double layer capacitors store energy by polarising ions at the electrode-electrolyte interface. Ions are attracted to the oppositely charged electrode, arranging themselves in an electrical double layer (see Figure 5.1 for a sketch of an electrical double layer capacitor).

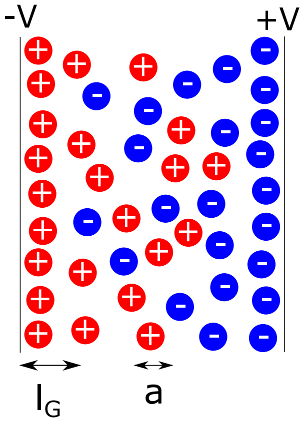

Figure 5.1: *Schematic of an electrical double layer capacitor with a smooth electrode. Here, a is the ion diameter and* l_G *is the characteristic width of the electrical double layer.*

The characteristic distance between the layer of counterions (the so-called Stern layer) and the electrode, l_G, is $O(\mathrm{nm})$. To first approximation, the double layer capacitor can be considered as effectively a dielectric capacitor with effective surface separation l_G, so that the capacitance $C \sim 1/l_G$ (Conway, 1999). Since l_G is small, the double layer capacitance is large compared to traditional dielectric capacitors for which the surface separation is usually macroscopic. In addition, the large mobility of the ions allows electrical double layer capacitors to readily charge and discharge. This gives them a comparative advantage over conventional batteries and fuel cells in terms of power delivery (see Figure 5.2).

Early experiments revealed that porous or rough electrodes enjoy large capacitance per projected area compared to flat electrodes (Conway, 1999). The presence of roughness increases the surface area of the electrode accessible to ions. Intuitively, as charge storage occurs via the packing of ions close to the electrode, surface area enhancement leads to capacitance enhancement. However, recent experiments with porous carbide-divided carbon

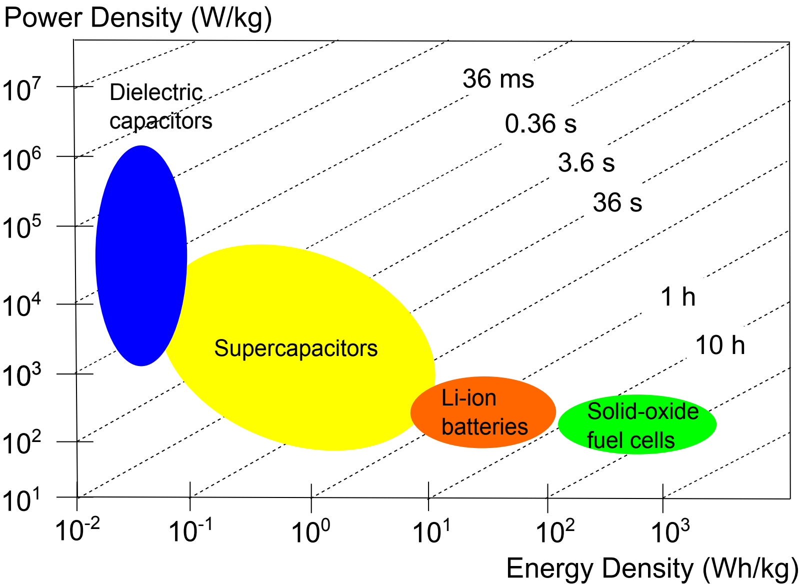

Figure 5.2: *The specific power and energy of supercapacitors compared with other means of energy storage. Imagine a supercapacitor-powered electric vehicle: the specific power shows how fast one can go, and the specific energy shows how far one can go on a single charge. Times shown are the time constants of the devices, obtained by dividing the energy density by the power. The plot is adapted from Simon and Gogotsi (2008); Tan and Lee (2013).*

electrodes (see Raymundo-Piñero et al., 2006; Chmiola et al., 2006; Largeot et al., 2008; Lin et al., 2009) have shown drastic increase in capacitance when the pore size approaches the ion size. Such an increase cannot be accounted for by surface area enhancement alone, and the physical picture in Figure 5.1 ceases to hold (see Figure 5.3).

The extremely large energy density and power density of nanoporous supercapacitors make them particularly well suited for critical applications that require energy in bursts during a short period of time, *e.g.* automobiles and emergency doors (Miller and Simon, 2008; Frackowiak et al., 2013). In addition, the ability of nanoporous supercapacitors to quickly recharge makes them ideal for storing energy from renewable energy sources such as wind turbines and solar cells. Ionic liquids are often the electrolyte of choice for electrical double layer capacitors because they are electrochemically stable.

Prior theories of equilibrium charge storage (Kondrat and Kornyshev, 2011; Skinner et al., 2011; Lee et al., 2014a) and of the kinetics of power delivery (Kondrat and Kornyshev, 2013; Lee et al., 2014a) in nanoporous supercapacitors focused on metallic screening to explain capacitance enhancement. Carbon electrodes are (semi)-conducting, and the free electrons inside the material respond to screen an external charge. The effect of metallic screening can be considered via a simple calculation: Consider a point charge located at the origin and confined in a slit pore of width L. To first approximation, carbon materials can be considered as perfectly metallic, and thus the electric potential $\phi = 0$ on the pore

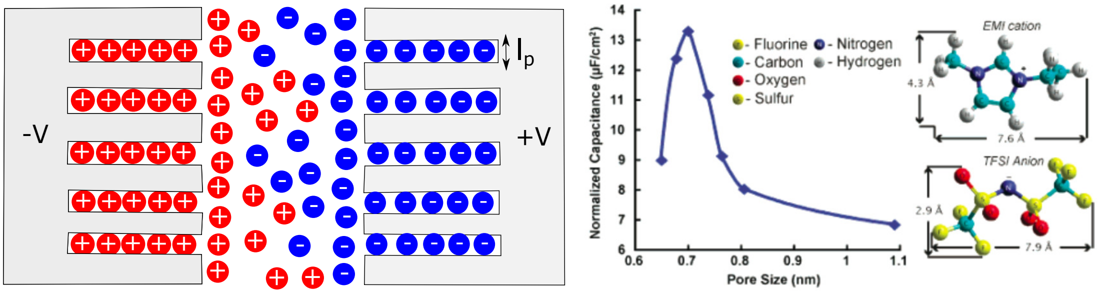

(a) (b)

Figure 5.3: *Marked enhancement in capacitance is seen when the pore size of the electrode approaches the ion size. a) A schematic sketch of a supercapacitor electrode with typical pore width l_p of the same order of magnitude as the ion diameter. b) Experimental measurement by Largeot et al. (2008) which shows that the capacitance increases with decreasing pore width up until the pores are too small for the ions to enter.*

walls. Noting the axisymmetry in the problem, the electric potential satisfies the Laplace equation

$$\frac{1}{r}\frac{\partial}{\partial r}\left(r\frac{\partial \phi}{\partial r}\right)+\frac{\partial^2 \phi}{\partial z^2}=-4\pi q\frac{\delta(r)}{2\pi r}\delta(z),\ z\in[-L/2,L/2], \tag{5.1}$$

with boundary conditions

$$\phi(\pm L/2,r)=0, \tag{5.2}$$

and decay condition at infinity

$$\phi(z,r)\to 0,\ \text{as}\ \sqrt{z^2+r^2}\to\infty, \tag{5.3}$$

We can express $\phi(z,r)$ as a Fourier series

$$\phi(z,r)=\sum_{n=0}^{\infty} f_n(r)\cos\left(\frac{(2n+1)\pi}{L}z\right). \tag{5.4}$$

Substituting Equation (5.4) into (5.1), we find that

$$\frac{1}{r}\frac{\mathrm{d}}{\mathrm{d}r}\left(r\frac{\mathrm{d}f_n}{\mathrm{d}r}\right)-\left(\frac{(2n+1)\pi}{L}\right)^2 f_n=-\frac{4q}{\epsilon L}\frac{\delta(r)}{r}, \tag{5.5}$$

where we have used the identity $\sum_{n=0}^{\infty}\cos\left(\frac{(2n+1)\pi}{L}z\right)=L\delta(z)/2$. Solving Equation (5.5), noting the jump condition for Greens function $\lim_{r\to 0} rf_n'=-4q/(\epsilon L)$, and applying the asymptotic decay condition (5.3), we arrive at

$$f_n(r)=\frac{4q}{\epsilon L}K_0\left(\frac{(2n+1)\pi}{L}r\right), \tag{5.6}$$

and the potential at the symmetry plane of the pore, $z = 0$, is given by the rapidly converging sum[1]

$$\phi(r) = \frac{4q}{\epsilon L} \sum_{n=0}^{\infty} K_0 \left(\frac{(2n+1)\pi}{L} r \right). \tag{5.8}$$

Noting that $K_0(x) \to e^{-x}/\sqrt{2\pi x}$ as $x \to \infty$, Equation (5.8) shows that the interaction energy between two charges in a narrow pore decreases *faster than exponentially* for large separations, with the screening length proportional to L. Decreasing the pore size increases the degree of this so-called "ion-image" interaction, which in turn exponentially screens the electrostatic interactions between ions (Kondrat and Kornyshev, 2011; Rochester et al., 2013). This screening decreases the energy penalty for packing like charges and unbinding unlike charges, purportedly leading to an increase in the capacitance.

This effect of metallic screening has been observed in molecular dynamics (Jiang et al., 2011; Wu et al., 2011; Qiao et al., 2012; Merlet et al., 2012; 2013a; Vatamanu et al., 2013; Péan et al., 2014; Kondrat et al., 2014) and Monte Carlo (Kiyohara et al., 2011; Kondrat et al., 2011; Kiyohara et al., 2012; 2013) simulations. However, if metallic screening is the sole driver of increased capacitance, the capacitance can only be optimised when the pore size equals the ion size. Such a close-fitted pore, however, is detrimental to the charging dynamics because of the reduced effective diffusivity (Kondrat and Kornyshev, 2013; Kondrat et al., 2014) and because the kinetic barrier to pore entry is large. Increased capacitance therefore appears to come at the cost of prolonged charging. A natural question is then: Can the capacitance be maximised away from such close-fitting pores?

Another important aspect in supercapacitor charging is reversibility. A simple mean-field model (Kondrat and Kornyshev, 2011) suggests that a voltage induced phase transition is what drives capacitance; this suggestion is supported by earlier Monte Carlo (Kiyohara et al., 2011) and molecular dynamics (Vatamanu et al., 2015) simulations of porous electrodes. However, such abrupt transitions can be detrimental to charging due to possible 'hysteresis energy losses' when charging and discharging routes follow different stable branches. It is thus important to know whether charging can always be reversible, and how to move away from potential hysteresis.

To answer these crucial questions, we develop a mean-field theory for charge storage in nanoporous supercapacitors by deriving the steric and electrostatic contributions to the free energy of confined ions. We will then compute the phase behaviour of the system and the corresponding differential capacitance.

---

[1] Equation (5.1) can also be solved via the Hankel transform, yielding

$$\phi(r) = \frac{q}{\epsilon} \frac{1}{\sqrt{r^2 + z^2}} - \frac{q}{\epsilon} \int_0^{\infty} e^{-kL} \frac{\cosh(kz)}{\cosh(ka)} J_0(kr) \mathrm{d}k. \tag{5.7}$$

We will use this integral representation to compute the self-energy, as shown below.

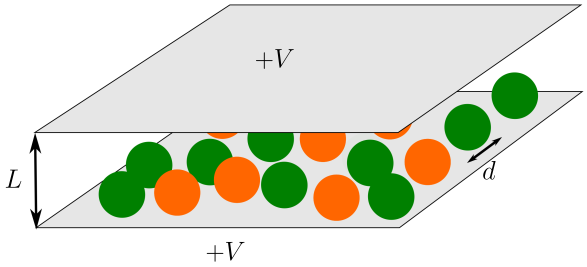

Figure 5.4: *Schematic drawing of the model porous electrode under consideration: Ions of diameter d are confined between two metallic surfaces separated by distance L with applied potential difference V.*

Our model shows that for systems with unfavourable ion-pore interaction energy (ionophobic pores), optimal capacitance can be achieved with pores that are significantly larger than the ion size. In addition, we show that charging hysteresis exists only for a narrow range of ion-pore interaction energies. Thus our model provides a framework to design optimal nanoporous supercapacitors that avoid the capacitance-power-hysteresis trilemma.

5.2 Mean-Field Theory of Charge Storage

Conceptually, a supercapacitor is a device consisting of two nanoporous electrodes immersed in an electrolyte that stores energy via potential-driven adsorption of counterions in electric double layers formed at the electrolyte/electrode interface. Here, we consider a single slit nanopore, where the pore entrance and closing are ignored. Charging is modelled by applying a non-zero potential to the pore walls (Figure 5.4). We focus on pores comparable in size with the ion diameter. In this limit, the system is quasi two-dimensional, and we can assume that ions are located on the central symmetry plane of the pore. The out-of-plane packing of ions (for $L > d$) is taken into account by introducing an effective pore-width dependent ion diameter $d^* \leq d$, as seen below.

5.2.1 Thermodynamic Perturbation Theory

As the electrostatic interaction is exponentially decaying and weak compared to $k_B T$ (*c.f.* Equation (5.8)), we can consider it as a perturbation to an uniform hard sphere fluid. We can write the Hamiltonian of the system as

$$H = H_{\mathrm{HS}} + \lambda H_{\mathrm{ele}}, \tag{5.9}$$

where H_{HS} is the Hamiltonian for hard sphere interactions, and H_{ele} is the Hamiltonian for electrostatic interactions. Assume for now that the partition function for H_{HS}, a collection of uncharged hard spheres, is a quantity that we have an analytical handle on. We wish to treat λ as a perturbative parameter, and set $\lambda = 1$ at the end of the calculation. The free energy is a function of λ, $F = F(N, V, T, \lambda)$, with $F = -k_B T \log Z$ where Z is the partition function. Thus

$$\begin{aligned} \left(\frac{\partial F}{\partial \lambda}\right)_{N,V,T} &= -\frac{k_B T}{Z}\left(\frac{\partial Z(N,V,T,\lambda))}{\partial \lambda}\right)_{N,V,T} \\ &= \frac{\int \mathrm{d}\mathbf{r}^N \, \frac{\partial H}{\partial \lambda} e^{-\beta H(\mathbf{r}^N, \lambda)}}{Z} \\ &= \left\langle \frac{\partial H}{\partial \lambda} \right\rangle_\lambda , \end{aligned} \tag{5.10}$$

where $\langle \cdots \rangle_\lambda$ denotes the ensemble average keeping λ constant (note that $Z = \langle 1 \rangle_\lambda$), and $\mathrm{d}\mathbf{r}^N = \prod_{i=1}^N \mathrm{d}\mathbf{r}_i$ where $\mathbf{r}_i$ is the position vector of the i^{th} particle, and N is the total number of particles. Now, we evaluate the second derivative of the free energy $F(\lambda)$ with respect to λ,

$$\begin{aligned} \frac{\partial^2 F}{\partial \lambda^2} &= \left\langle \frac{\partial^2 H}{\partial \lambda^2} \right\rangle_\lambda - \beta \left\langle \left(\frac{\partial H}{\partial \lambda}\right)^2 \right\rangle_\lambda + \beta \left\langle \left(\frac{\partial H}{\partial \lambda}\right) \right\rangle_\lambda^2 \\ &= -\beta \left[\left\langle (H_{\mathrm{ele}})^2 \right\rangle_\lambda - \langle H_{\mathrm{ele}} \rangle_\lambda^2 \right] \leq 0 \end{aligned} \tag{5.11}$$

Therefore, as the second derivative is non-positive, and

$$\frac{\partial F}{\partial \lambda} \leq \left(\frac{\partial F}{\partial \lambda}\right)_{\lambda=0} \implies F \leq F_{\mathrm{HS}} + \langle H_{\mathrm{ele}} \rangle_{\lambda=0} . \tag{5.12}$$

Equation (5.12) is known as the Gibbs-Bogoliubov inequality (Kardar, 2007). Now, if we assume that the fluctuations of $\frac{\partial H}{\partial \lambda}$ are small for every λ, then

$$\frac{\partial^2 F}{\partial \lambda^2} = -\beta \left[\left\langle (H_{\mathrm{ele}})^2 \right\rangle_\lambda - \langle H_{\mathrm{ele}} \rangle_\lambda^2 \right] \approx 0. \tag{5.13}$$

Therefore, Equation (5.12) becomes

$$F \approx F_{\mathrm{HS}} + \langle H_{\mathrm{ele}} \rangle_{\lambda=0} , \tag{5.14}$$

and the grand canonical free energy density $\mathfrak{F}(\rho_+, \rho_-)$ of ions inside such pores is given by

$$\beta \mathfrak{F} = \beta \langle H_{\mathrm{ele}} \rangle_{\lambda=0} + \beta F_{\mathrm{HS}} + \sum_{\alpha=\pm} h_\alpha \rho_\alpha , \tag{5.15}$$

where h_α is the electrochemical potential of species α, which couples the system to the bulk ionic liquid.

5.2.2 Hard Sphere Free Energy

To make further analytical progress, we need to obtain the thermodynamic properties of confined hard spheres. Unfortunately, even the partition function of such a simple system cannot be evaluated analytically. However, an approximate method known as "scaled particle" theory is a good approximation to such systems (Helfand et al., 1961). To understand the physics behind scaled particle theory, we will review the derivation of the equation of state for a system of hard sphere that is constrained to a 2D plane (*i.e.* effectively a system of hard discs). Equations (5.16)-(5.28) constitute review material. We follow the approach of Hansen and MacDonald (2014) for a 3D hard sphere system, but extend it to treat 2D hard discs.

The key intuition is to consider cavities in a fluid of hard discs. At thermal equilibrium, the probability of finding a cavity of radius r, $\mathcal{P}(r)$ is related to the work needed to form such a cavity, $w(r)$, by the Boltzmann distribution

$$\mathcal{P}(r) = e^{-\beta w(r)}. \tag{5.16}$$

Now, we consider a homogenous 2D fluid of hard discs. The probability of finding a cavity of radius 0 is simply the proportion of total area that is unoccupied by the hard discs, *i.e.* $\mathcal{P} = 1 - \frac{\pi}{4}d^2\rho$, where ρ is the 2D density and d the disc diameter. Let us consider the probability of finding an infinitesimally small cavity of diameter $\epsilon \ll d$. The probability can be evaluated by considering the cavity as a virtual particle, and noting that exclusion area when the small virtual particle and the larger particle are in contact is given by $V_e = \pi(d+\epsilon)^2/4$. Thus, the probability $\mathcal{P}_0$ of finding such cavity is

$$\mathcal{P}_0 = 1 - \frac{\pi}{4}\rho\left(d+\epsilon\right)^2, \tag{5.17}$$

where we have exploited the fact that the particle is small, and therefore the exclusion areas do not overlap. Thus the work done to form a small cavity of diameter ϵ is

$$\beta w_0(\epsilon) = -\log\left(1 - \frac{\pi}{4}\rho\left(d+\epsilon\right)^2\right). \tag{5.18}$$

Next, we consider a large cavity of diameter $s \gg d$. The work needed to form the large cavity is dominated by the pressure-area work and is given by

$$\beta w_l(s) = \frac{\beta\pi}{4}s^2 p, \tag{5.19}$$

where p is the pressure. To interpolate between the large cavity and small cavity limits, we write

$$\beta w(d) = a_0 + a_1 s + \beta\frac{\pi}{4}s^2 p. \tag{5.20}$$

The constants a_0 and a_1 can be determined by requiring the macroscopic description (5.20) match the microscopic description (5.18) for small cavity size, *i.e.* $w(0) = w_0(0)$, and $w'(0) = w_0'(0)$. Thus, we arrive at

$$a_0 = -\log(1-\eta),\ a_1 = \frac{\frac{\pi}{2}\rho d}{1-\eta}, \tag{5.21}$$

where $\eta = (\pi/4)\rho d^2$ is the 2D packing fraction. The excess chemical potential of the system is the work needed to create space to insert an extra particle, thus $\mu_{\text{ex}} = w(d)$, and

$$\mu_{\text{ex}} = -\log(1-\eta) + \frac{2\eta}{1-\eta} + \beta\frac{p\eta}{\rho}. \tag{5.22}$$

Using the classical thermodynamic relation $V\mathrm{d}p = N\mathrm{d}\mu$ (at constant temperature), and the definition of excess chemical potential, $\beta\mu_{\text{ex}} = \beta\mu - \log\rho$, we have an extra relation between μ_{ex} and p

$$1 + \beta\rho\frac{\partial\mu_{\text{ex}}}{\partial\rho} = \beta\frac{\partial p}{\partial\rho}. \tag{5.23}$$

From Equations (5.22)-(5.23), we arrive at the equation of state that was first derived by Helfand et al. (1961)

$$Z \equiv \frac{\beta p}{\rho} = \frac{1}{(1-\eta)^2}, \tag{5.24}$$

and, using the relation $\beta\partial F_{\text{ex}}/\partial\rho = N(Z-1)/\rho$ from classical thermodynamics, the corresponding free energy per area is given by

$$\beta F_{\text{ex}} = \rho\left[\frac{\eta^2}{1-\eta} - \log(1-\eta)\right]. \tag{5.25}$$

The ions in the nanopore is not quite a system of hard discs because the ions can move away from the central plane. However, the typical pore separation is only slightly larger than the ion diameter, and we can account for the positional disorder of ions normal to the pore surface as a perturbation to the otherwise 2D system — this effectively renormalises the ion diameter. The free energy is then given as a sum of the ideal gas contribution and hard core exclusion (see Schmidt and Löwen, 1996; 1997),

$$\beta F_{\text{HS}} = \sum_{\alpha=\pm}\tilde{\rho}_\alpha\log\tilde{\rho}_\alpha + \tilde{\rho}\left[\frac{\tilde{\eta}^2}{1-\tilde{\eta}} - \ln(1-\tilde{\eta})\right], \tag{5.26}$$

where $\tilde{\rho} = \rho(d/\sigma)^2$ is the effective ion density, $\tilde{\eta}(\rho) = \pi\rho\sigma^2/4$ is the effective ion packing fraction and we have introduced an effective ion diameter $\sigma(d, L, \rho)$ that accounts for the out-of-plane packing of ions. Schmidt and Löwen (1996; 1997) showed that

$$\sigma(d, L, \rho)^2 = d^2 + \frac{1}{\alpha(\rho)} - \frac{L \exp\left(\alpha(\rho)L^2/4\right)}{\sqrt{\pi\alpha(\rho)}\mathrm{erfi}(\sqrt{\alpha(\rho)}L/2)}, \tag{5.27}$$

where $\mathrm{erfi}(z) = \pi^{-1/2}\int_{-z}^{z} \mathrm{d}z'\, e^{z'^2}$ is the imaginary error function, and

$$\alpha(\rho) = \pi\rho g(\rho) = \pi\rho\frac{1-\tilde{\eta}(\rho)/2}{(1-\tilde{\eta}(\rho))^2}, \tag{5.28}$$

is the average density at contact, with $g(\rho)$ being the 2D pair correlation function evaluated at contact.

5.2.3 Electrostatic Free Energy

According to Equation (5.14), the electrostatic contribution to the free energy is given by the average of the Hamiltonian for electrostatic interactions over the hard sphere system. Mathematically, this average is given by

$$\langle H_{\mathrm{ele}}\rangle_{\lambda=0} = \frac{1}{Z_{\mathrm{HS}}}\int \mathrm{d}\mathbf{r}_+^{N_+}\int \mathrm{d}\mathbf{r}_-^{N_-}\, H_{\mathrm{ele}}\left(\mathbf{r}_+^{N_+}, \mathbf{r}_-^{N_-}\right)\, e^{-\beta H_{\mathrm{HS}}\left(\mathbf{r}_+^{N_+},\mathbf{r}_-^{N_-}\right)}. \tag{5.29}$$

where $Z_{\mathrm{HS}} \equiv \langle 1\rangle_{\lambda=0}$ is the partition function, $\mathrm{d}\mathbf{r}_\alpha^{N_\alpha} = \prod_{i=1}^{N_\alpha}\mathrm{d}\mathbf{r}_i^\alpha$ where $\mathbf{r}_i^\alpha$ denotes the position of the i^{th} particle of type α, and N_α is the total number of particles of type α. The Hamiltonian for electrostatic interactions is given by

$$H_{\mathrm{ele}} = \frac{1}{2}\sum_{\alpha,\beta=\pm}\sum_{i=1}^{N_\alpha}\sum_{j=1}^{N_\beta}{}' v_{\alpha\beta}(|\mathbf{r}_i^\alpha - \mathbf{r}_j^\beta|), \tag{5.30}$$

where ${\sum}'^{N_\beta}_{j=1}$ denotes sum over index j except $\alpha = \beta = i = j$, and the interaction potential $v_{\alpha\beta}$ is given by (*c.f.* Equation (5.8))

$$v_{\alpha\beta}(r) = \frac{4q_\alpha q_\beta}{\epsilon L}\sum_{n=0}^{\infty} K_0\left(\frac{(2n+1)\pi}{L}r\right). \tag{5.31}$$

Hence, substituting Equation (5.30) into (5.29), we arrive at

$$\langle H_{\mathrm{ele}}\rangle_{\lambda=0} = \frac{1}{2}\sum_{\alpha,\beta=\pm}{}' \int \mathrm{d}\mathbf{r}\mathrm{d}\mathbf{r}' v_{\alpha\beta}(|\mathbf{r}_i^\alpha - \mathbf{r}_j^\beta|)\rho_{\alpha\beta}^{(2)}(\mathbf{r}-\mathbf{r}'), \tag{5.32}$$

where we have introduced the two particle distribution function $\rho^{(2)}_{\alpha\beta}(\mathbf{r}-\mathbf{r}')$, defined as

$$\rho^{(2)}_{\alpha\beta}(\mathbf{r}-\mathbf{r}') = \frac{1}{Z_{\text{HS}}} \sum_{\alpha,\beta=\pm}' \int \mathrm{d}\mathbf{r}_{\alpha}^{N_\alpha} \int \mathrm{d}\mathbf{r}_{\beta}^{N_\beta}\, e^{-\beta H_{\text{HS}}} \sum_{i=1}^{N_\alpha} \sum_{j=1}^{N_\beta} \delta(\mathbf{r}-\mathbf{r}_i^{\alpha})\delta(\mathbf{r}'-\mathbf{r}_j^{\beta}). \qquad (5.33)$$

Physically, $\rho^{(2)}_{\alpha\beta}(\mathbf{r}-\mathbf{r}')$ is the probability of finding a particle of type α at point $\mathbf{r}$ and a particle of type β at point $\mathbf{r}'$ in a hard sphere system. Even in the scaled particle theory framework, $\rho^{(2)}_{\alpha\beta}(\mathbf{r}-\mathbf{r}')$ is very cumbersome. A simple approximation can be motivated by noting that if the particles are uncorrelated, $\rho^{(2)}_{\alpha\beta}(\mathbf{r}-\mathbf{r}') = \rho_\alpha(\mathbf{r})\rho_\beta(\mathbf{r}')$. Since the system is assumed to be homogeneous, $\rho_\alpha(\mathbf{r}) = \rho_\alpha$ is a constant. In order to improve on this total neglect of correlations, we observe that the average particle-particle separation in the system is $R_{\text{c}} = 1/\sqrt{\pi\rho}$, where $\rho = \rho_+ + \rho_-$, and it is unlikely to find two particles with separation $r < R_c$. This observation motivates the approximation

$$\rho^{(2)}_{\alpha\beta}(\mathbf{r}-\mathbf{r}') \approx \rho_\alpha\rho_\beta\theta\Big[|\mathbf{r}-\mathbf{r}'| - R_{\text{c}}(\rho)\Big], \qquad (5.34)$$

where $\theta(x)$ is the Heaviside theta function. We therefore arrive at

$$\beta\left\langle H_{\text{ele}}\right\rangle_{\lambda=0} = 4c^2 R_{\text{c}}(\rho) l_B \sum_{n=0}^{\infty} \frac{1}{2n+1} K_1\left[\frac{\pi R_c(\rho)}{L}(2n+1)\right] \qquad (5.35)$$

with $c = \rho_+ - \rho_-$, and $l_B = q^2/(\epsilon k_B T)$ the thermal Bjerrum length (introduced in Section 2.1). In the following calculations, we will take $\epsilon = 2$ so that $l_B = 280$nm for monovalent ions.

5.2.4 Chemical Potential

The last component of the free energy is the electrochemical potential, which couples the confined system to the bulk ionic liquid. The electrochemical potential is given by

$$h_\pm = \pm u + \delta E_{\text{self}} + \delta E_\pm = \pm u - \frac{l_B}{L}\log 2 + \delta E_\pm, \qquad (5.36)$$

where the first term accounts for the interaction between the ion and the applied potential difference. The second term originates from the change in the ion self-energy due to the presence of metallic walls (the so-called “ion-image” interactions):

$$\delta E_{\text{self}} = l_B \lim_{\mathbf{r}\to 0}\left(\phi(\mathbf{r}) - \frac{1}{|\mathbf{r}|}\right) = -l_B \int_0^\infty \frac{e^{-kL}}{\cosh(kL)}\mathrm{d}k = -\frac{l_B}{L}\log 2, \qquad (5.37)$$

where we have make use of Equation (5.7), the integral representation of the potential.

The last term in Equation (5.36), $\delta E_{\pm}$, is the "resolvation energy" which includes the bulk chemical potential (the energy of transferring an ion from the bulk), and the ion-pore specific interactions (*e.g.* van der Waals interactions). In the following we assume $\delta E_+ = \delta E_- = \delta E$.

At zero applied voltage, $h_{\pm} = h_0 = \delta E_{\text{self}} + \delta E$ and the sign of h_0 determines whether the ion-pore interactions are favourable. For pores with $h_0 > 0$ (unfavourable ion-pore interaction), the occupancy of the pore at zero applied voltage is expected to be low, and we will refer to such pores as *ionophobic*. For large positive h_0 the pore will be (almost) free of ions at zero applied voltage, and we will call such pores *strongly ionophobic*. Conversely pores with $h_0 < 0$ will be termed *ionophilic*, and a large negative h_0 will correspond to *strongly ionophilic* pores, which are nearly fully occupied by ions at no applied voltage. $h_0 = 0$ marks the crossover between *ionophilic* and *ionophobic* which thus occurs at a resolvation energy $\delta E = \delta E_{\text{crossover}} = -\delta E_{\text{self}}$. For instance, for a 1nm wide pore and a typical Bjerrum length of 25nm, we have $\delta E_{\text{crossover}} \approx 17\ k_BT$.

To obtain an estimate for the range resolvation energies, we decompose δE into $\delta E \approx \delta E_{\text{desolv}} + \delta E_{\text{non-ele}}$, where δE_{desolv} is the desolvation energy of the bulk ionic liquid (transferring one solvated ion from the bulk liquid to the vapour state), and $\delta E_{\text{non-ele}}$ is the ion-pore non-electrostatic interactions (ion-pore electrostatic interactions are accounted for in δE_{self}). A combination of quantum mechanical density functional and molecular dynamics simulations (Jover et al., 2014) suggests $\delta E_{\text{desolv}} \approx 75 - 100 k_BT$ per ion.

The major source of non-electrostatic interactions between an ion and the nanopore is the van der Waals attraction. Jover et al. (2014) studied the ion-pore van der Waals interaction for ions located inside a carbon nanotube. We can estimate the ion-pore van der Waals interaction in a carbon-based slit pore by taking the large radius limiting value of the van der Waals interaction energy in the nanotube, *i.e.* $E_{\text{vdw,slit}} \approx 2E_{\text{vdw,cylinder}}(R \to \infty)$, as the $R \to \infty$ asymptotic value of the van der Waals interaction energy corresponding to the interaction energy between an ion and one side of the pore. This gives $\delta E_{\text{vdW}} \approx -65 k_BT$. We thus find that, roughly, $10 \lesssim \delta E/(k_BT) \lesssim 35$ (note that the crossover between ionophobic and ionophilic pores, $\delta E_{\text{crosover}}$, lies in this range). We stress that this range is not exhaustive as other physical effects (*e.g.* specific surface chemistry of the pore) are not taken into account; the definitive metric of ionophilicity/-phobicity is the occupancy of the pore at zero applied voltage.

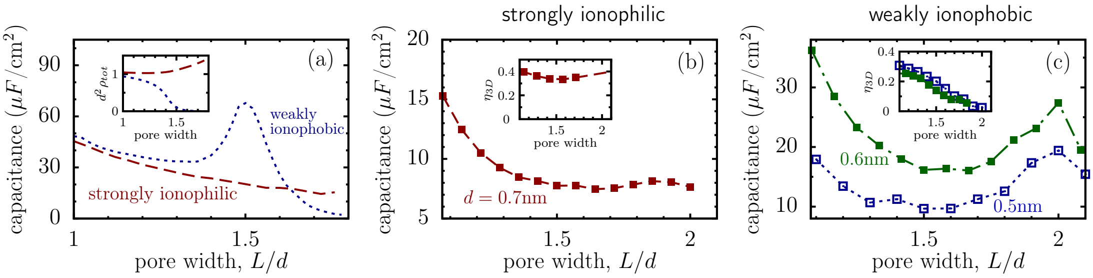

Figure 5.5: *The differential capacitance at zero voltage as a function of pore width. (a) Results from the mean field theory, plotted for weakly ionophobic ($\delta E = 25 k_B T$) and strongly ionophilic ($\delta E = 10 k_B T$) pores. The ion diameter is 0.5nm. The inset shows how the total ion density at zero voltage depends on pore width. (b)-(c) Results from Monte Carlo simulations for a strongly ionophilic pore ($\delta E = -2.5 k_B T$) and for weakly ionophobic pores ($\delta E = 38.5 k_B T$ for $d = 0.5$nm and $\delta E = 33.2 k_B T$ for $d = 0.6$nm). The insets show the 3D packing fraction $\eta_{3D} = (\pi/6)\rho d^3$ as a function of pore width.*

5.3 Searching for Maximal Capacitance

The key quantity characterising that low voltage capacitance response of a supercapacitor is the differential capacitance at zero voltage, *i.e.*

$$C_{D0} = \left.\frac{\mathrm{d}Q}{\mathrm{d}V}\right|_{V=0}. \tag{5.38}$$

Here Q is the charge stored in the slit pore, and V is the applied potential. In the following discussion, we compute $Q(V)$ via free energy minimisation, either through a mean-field theory or Monte Carlo simulations (see Appendix A for details of the MC simulations).

The mean-field approximation for the Helmholtz free energy density is given by (*c.f.* (5.15), and the expression for the entropic packing energy and electrostatic interaction energy derived in the previous Section)

$$\beta F(\rho_+, \rho_-) = U_{\mathrm{el}}(\rho_+, \rho_-) - S(\rho_+, \rho_-) + \sum_{\alpha=\pm} h_\alpha \rho_\alpha, \tag{5.39}$$

where U_{el} is the contribution to free energy due to electrostatic interactions (see Equation (5.35)), $S(\rho_+, \rho_-)$ is the excluded volume entropic contribution (see Equation (5.26)), and we assume that the density of ions in the slit pore is homogeneous. To obtain $Q(V)$ and hence C_{D0}, we minimise $F(\rho_+, \rho_-)$ over ρ_+ and ρ_- subject to fixed V, noting that $e(\rho_+ - \rho_-)$ is the charge per unit area where e is the elementary charge

For strongly ionophilic pores, the capacitance is indeed maximal for the smallest possible pores, in agreement with the conventional view that the capacitance increases monotonically as the pore size decreases (Raymundo-Piñero et al., 2006; Chmiola et al., 2006;

Largeot et al., 2008; Lin et al., 2009) (see dashed line in Figure 5.5a). Surprisingly, however, we find that for weakly ionophobic pores the differential capacitance exhibits a second peak when the pore width is significantly larger than the ion diameter (though still smaller than $2d$). This behaviour is due to two competing effects: On the one hand, the loss of ion-image interactions and an increase in the strength of the electrostatic interactions hinders ions from entering the pore. On the other hand, the same factors also render the pore less populated at zero voltage (the inset in Figure 5.5a). Thus the peak is achieved when the decrease in the total density frees up enough space in the pore that counter-ion insertion becomes entropically more favourable. In fact, for narrow and weakly ionophilic pores the initial charging is predominantly due to swapping co-ions for counterions and expelling co-ions, whereas for wider pores, it is the counter-ion insertion that drives charging.

This charging behaviour is in contrast to strongly ionophilic pores, where the total ion density increases with increasing pore width because the out-of-plane degrees of freedom allow ions to pack more efficiently. Therefore both entropy and ion-ion as well as ion-image interactions work against charging as the pore size (L) increases, and so the capacitance decreases monotonically for increasing L. The case of strongly ionophobic pores is not considered here — charging commences only when ions can overcome the ionophobicity barrier ($eV \approx \delta E$) and hence the capacitance at zero voltage is low or vanishes.

Monte Carlo simulations confirm the trends of predicted by the mean field model: Strongly ionophilic pores show a monotonic decrease of capacitance with increasing pore size (Figure 5.5b), while weak ionophobicity produces a local maximum with capacitances comparable to, or even higher than, the capacitance at $L \approx d$ (Figure 5.5c). The total ion packing fraction is almost constant with increasing pore width for strongly ionophilic pores (inset of Figure 5.5b) whereas for ionophobic pores it decreases with increasing pore width (inset of Figure 5.5c), agreeing qualitatively with the mean field model (inset of Figure 5.5a). We note that a slightly smaller δE in mean field theory is sufficient to achieve the same ion occupancy at zero voltage, hence ionophobicity, as in the Monte Carlo simulations. This discrepancy is because our mean field theory does not account for the change in ion-image interactions due to ions positioning themselves off the central symmetry plane of the pore (though this effect does not change the qualitative predictions of the mean field model).

Another important aspect in capacitance optimisation is how to choose between ion size and pore size. Intuitively one might expect that it is the *ratio* between the two that affects the capacitance. However, Figure 5.6a reveals another surprise: for weakly ionophilic pores, a peak in the capacitance emerges as ion diameter increases keeping the ratio between pore width and ion diameter fixed. Physically, even keeping L/d constant, the magnitude of the electrostatic interaction at contact $\sim 1/L$ (*c.f.* Equation (5.8)), and the

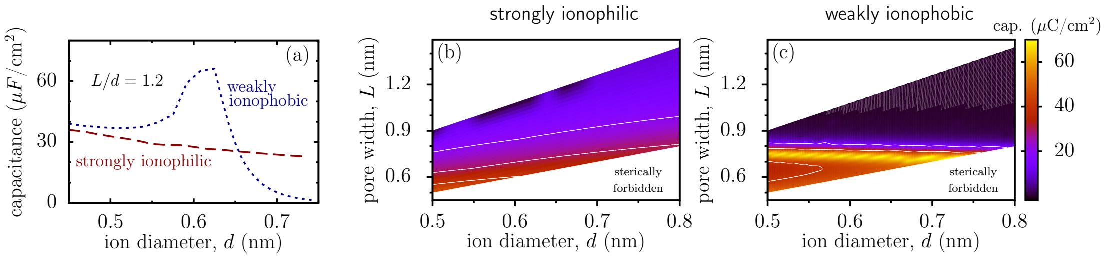

Figure 5.6: *(a) Capacitance at zero voltage as a function of ion diameter for weakly ionophobic ($\delta E = 25k_BT$) and strongly ionophilic ($\delta E = 10k_BT$) pores calculated using MFT. (b)-(c) Capacitance map for strongly and weakly ionophilic nanopores in the plane of ion diameter (d) and the pore width (L) calculated using MFT. This figure suggests a 'two-step optimisation strategy', in which an optimal pair (d, L) exists that maximises the differential capacitance.*

total density at zero voltage decreases with L as $\delta E_{\text{self}} \sim -1/L$ (see Equation (5.36)). Both effects promote charge storage by making the pore less populated for weak ionophobicities, and thus adsorption of new counterions becomes entropically more favorable. However, the charge density per ion is also decreased as L increases because $\sigma \sim 1/d^2 \sim 1/L^2$ (at constant L/d). Therefore it is a balance between these factors that gives rise to a peak in the capacitance in weakly ionophilic pores. For strongly ionophilic pores, the total density at zero applied voltage is large regardless, thus neither the self-energy factor nor the reduction of electrostatic interactions affect the capacitance much, and it is the reduction of ion charge density that leads to a monotonic decrease.

Therefore, to get the largest possible capacitance, one must optimise *both* the pore width and the ion diameter depending on the ionophilicity (see Figure 5.6b and c); the corresponding optimum depends on ionophilicity.[2]

It is important to stress that the presence of a second maximum is different from the oscillatory behaviour of capacitance as a function of pore width (Feng and Cummings, 2011; Jiang et al., 2011; Pizio et al., 2012) and solvent polarity (Jiang and Wu, 2014) observed in earlier studies. For weakly ionophobic pores, a maximum occurs because of entropic effects, while previous works, the pore is wider than a few ion diameters and thus it is the overlapping double layers that cause the non-monotonicity in the capacitance.

The fact that the capacitance reaches a maximum for a relatively *wide* pores has an important impact on optimizing supercapacitors. It has been assumed that there must be a trade-off between having large capacitance (narrow pores) and fast charging (wide pores) (Kondrat and Kornyshev, 2013). Charging is slower for narrower pores because

---

[2] Mathematically, the three dimensional lengthscales are l_B, d and L. One can non-dimensionalise the free energy (5.15), and this will show that the free energy is only a function of dimensionless quantities l_B/d and l_B/L. We report results in dimensional units here to facilitate comparison with future experimental data.

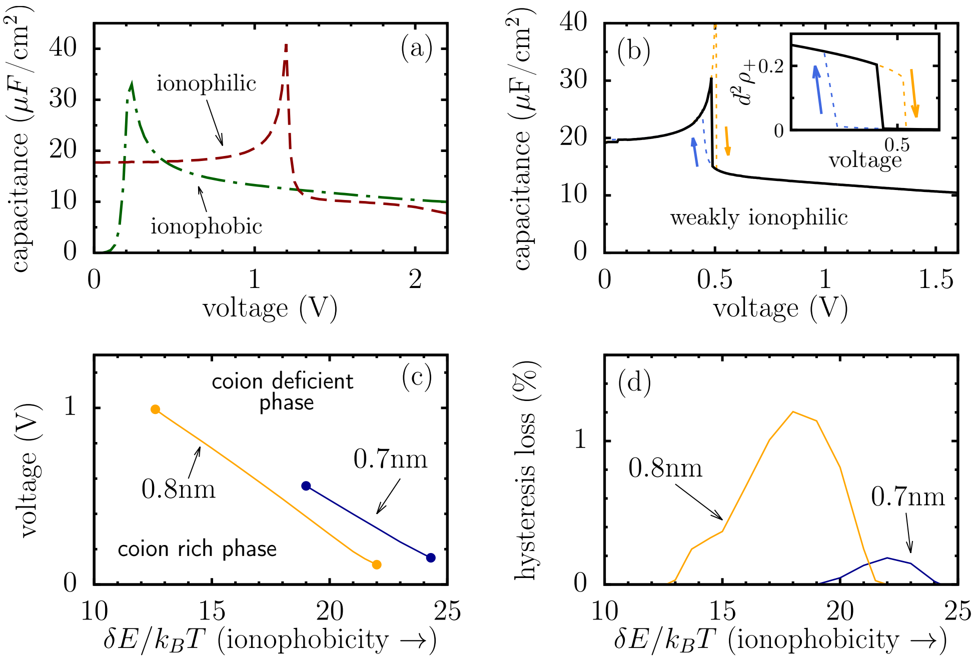

Figure 5.7: *Charging proceeds via a discontinuous phase transition for some parameter regimes. In all plots ion diameter $d = 0.5nm$. (a) Capacitance as a function of voltage in the continuous charging regime. The ionophilic and -phobic pores have $\delta E = 10k_BT$ and $\delta E = 32k_BT$ respectively. (b) Capacitance as a function of voltage in the discontinuous charging regime. The solid curve indicates the minimum free energy path, and the dotted curves denote the hysteresis loop. The curve is plotted for $\delta E = 18k_BT$. The inset shows the abrupt expulsion of co-ions that drives the phase transition. (c) The phase diagram plotted for different slit widths. (d) The percentage of energy that is lost due to hysteresis during discharging of a nanopore charged at 1.3 volts.*

the collective (or effective) diffusion coefficient, which determines the rate of charging, decreases with decreasing pore width (Kondrat and Kornyshev, 2013; Kondrat et al., 2014; Lee et al., 2014b). Our analysis therefore provides the key insight that charging kinetics and capacitance can be simultaneously optimised by tuning the ionophilicity of the pore.

5.4 Hysteretic Charging

Beyond the low-voltage response of supercapacitors, which is captured by the differential capacitance at zero voltage (5.38), we now turn to the question of reversibility and charging hysteresis for large applied voltages. Figure 5.7 shows that charging can proceed via a first-order discontinuous phase transition for intermediate ionophilicities, or via a continuous process beyond the critical endpoints.

Figure 5.7a shows the capacitance as a function of applied voltage for ionophobic and ionophilic pores with no phase transition. For strongly ionophobic pores with resolvation energy δE above the critical endpoint, the pore is initially empty and counter-ions will only enter the pore when the applied potential matches the unfavourable resolvation energy; hence there is a peak in capacitance when charging starts at $eV \approx \delta E$. Subsequently, a separate regime of packing like charges starts and persists until the applied potential surpasses the interaction energy between co-ions. Beyond that point the capacitance falls off rapidly. Indeed, recent NMR experiments show that charging proceeds continuously without phase transition and abrupt co-ion expulsion for KOH activated carbon pores (Griffin et al., 2014b; 2015), which are known to be strongly ionophilic (Richey et al., 2014). We note that while it is difficult to calculate the resolvation energy (ionophobicity) for these pores, Figure 5.7c suggests that it must at least be lower than $12k_BT$, consistent with our estimate of the crossover between the ionophilic and ionophobic pores which occurs at $\delta E_{\text{crossover}} \approx 17k_BT$.

The situation is different for strongly ionophilic pores with δE below the critical endpoint. The pore is initially nearly fully occupied with ions. Charging occurs via *quid pro quo* swapping of co-ions for counter-ions due to the very strong resolvation energy, and the charge density increases but the total density remains almost constant. Therefore, the capacitance is almost constant throughout charging, and only falls off when the co-ion density in the slit pore approaches zero.

For ionophilicities between the two critical endpoints, charging proceeds via a large discontinuous drop in density and capacitance (see Figure 5.7b). At low voltages, charging proceeds through swapping of co-ions for counter-ions and co-ion expulsion, but at the point of the phase transition the system discontinuously expels nearly all co-ions (see inset of Figure 5.7b), and beyond that point charging occurs via counter-ion adsorption. This voltage-induced abrupt expulsion of co-ions and the drop in total ion density has recently been observed in atomistic molecular dynamics simulations of [C2mim][FSI] and [C4mim][TFSI] ionic liquids in slit nanopores (Vatamanu et al., 2015). Figure 5.7c shows that the transition voltage increases with decreasing ionophobicity, as both counter ions and co-ions are favourably adsorbed into the pore, making it more difficult to expel the co-ions. The window of ionophilicities for which a phase transition occurs is wider for larger pores where electrostatic interactions are stronger and more long-ranged.

A signature of a discontinuous phase transition is hysteresis. The red dotted lines in Figure 5.7b show that the branch followed by the system as the voltage is increased is different to that followed by the system as the voltage is decreased.

To obtain the energy lost due to hysteresis (Figure 5.7d), we first calculate the energy stored when charging a nanopore from $u = 0$ to $u = V = 1.3$ V along the charging path (orange lines/arrows in Figure 5.7b), $\mathcal{E}_{\text{charg}} = \mathcal{E}(0, V)$, and the energy released by fully discharging it along the discharging path (blue lines/arrows in Figure 5.7b), $\mathcal{E}_{\text{discharg}} =$

$-\mathcal{E}(V,0)$, noting that the energy (per surface area) stored in a nanopore by charging it from $u = u_1$ to $u = u_2$ is

$$\mathcal{E}(u_1, u_2) = \int_{u_1}^{u_2} C_D(u) u \, \mathrm{d}u, \tag{5.40}$$

where $C_D(u) = \mathrm{d}Q/\mathrm{d}V$ is differential surface-specific capacitance. The hysteric energy loss is then shown as percentage of the stored energy lost in hysteresis, *i.e.* $100\% \times (\mathcal{E}_{\text{charg}} - \mathcal{E}_{\text{discharg}})/\mathcal{E}_{\text{charg}}$. Figure 5.7d shows that a sizeable amount of energy is lost per cycle as a consequence of hysteresis, with wider pores producing the largest energy losses. In practical applications, the regime where charging proceeds via a first order phase transition should be avoided. However, this hysteresis loop in the differential capacitance can be used to probe the properties of the capacitor system experimentally.

5.5 Conclusion

Using a mean-field model for charge storage in 2D nanoconfinement, we have demonstrated the potential for simultaneously boosting capacitance, accelerating charging, and avoiding hysteresis in nanoporous supercapacitors. Our analysis shows that the long-espoused paradigm that equates narrow pores with necessarily larger capacitance does not always hold: Entropic effects may produce a second, more pronounced peak in capacitance for relatively wide ionophobic pores (Figure 5.5a). Similarly, there is an optimal ion diameter for weakly ionophilic pores, when keeping the ratio between the ion diameter and pore width constant (Figure 5.6a). For large applied voltages, a voltage-induced discontinuous phase transition is predicted by the model, and the phase diagram has two critical endpoints corresponding to the limit of very ionophobic and ionophilic pores (Figure 5.7). The phase transition gives rise to hysteresis and a sizeable energy loss, and can be avoided by either reducing the operating voltage of the capacitor, or moving the pore ionophilicity away from the critical endpoints, for instance by making the pores more ionophobic. Thus, the capacitance-power-hysteresis trilemma can be resolved by judicious tuning of experimental parameters.

We note that the ion diameter and pore width are parameters that may be relatively straightforward to tune experimentally. Further, our framework shows that both parameters can be optimised independently. On the same footing, our model singles out a key outstanding challenge for further experimentation — the controlled tuning of the ionophobicity/-philicity of the pore. This tuning could be achieved by changing the ion-pore non-electrostatic interaction. In addition to van der Waals interactions, suppose we have an ion that has multiple conformational states with different effective diameters (for example expanded versus folded alkyl chains on an ionic liquid ion). If the pore separation is less than the effective diameter of the lowest energy conformation, then entering the pore will require the ion to adopt a higher conformation energy, and thus incur a conformational energy penalty. Similarly, if the pore walls are flexible and ions can only enter by deforming the walls (as observed in Kaasik et al. (2013); Hantel et al. (2014)), the elastic energy will result in an unfavourable ion-pore non-electrostatic interaction. This interaction could also be controlled by addition of surfactants to ionic liquids (Fic et al., 2010; 2011) or by using ionic liquid mixtures (Lin et al., 2011). Experimental studies of ionophilicity are currently scarce, and we hope that our theory will provide a framework to assess and direct future efforts to address this.

Appendix 5.A Monte Carlo Simulations

The grand canonical Monte Carlo simulations were performed by Dr Svyatoslav Kondrat of Forschungszentrum Jülich using the Towhee package (Martin, 2013). He has used the same method as in Kondrat et al. (2011), and we refer the reader there for details of the simulation.

Ionic liquid molecules are modelled as charged hard spheres, but instead of the Coulomb potential, we use the analytical solution for the ion-ion interactions

$$v_{\alpha\beta}(r, z_1, z_2) = \frac{4 q_\alpha q_\beta}{\varepsilon_p L} \sum_{n=1}^{\infty} K_0\left(\pi n r / L\right) \sin(\pi n z_1 / L) \sin(\pi n z_2 / L). \tag{5.41}$$

Ion-pore wall interactions are captured by the self-energy potential

$$\begin{aligned} \delta E_{\text{self}}(z) &= \lim_{r \to 0} (\phi(r) - 1/r) \\ &= -\frac{l_B}{L} \int_0^\infty \left[\frac{1}{2} - \frac{\sinh(Q(1 - z/L)) \sinh(Qz/L)}{\sinh(Q)} \right] dQ, \end{aligned} \tag{5.42}$$

where z is the position across the pore and r distance to the charge (see Kondrat and Kornyshev (2011)).

The resolvation energy (δE) and the applied voltage (V) are subsumed into the chemical potential in the grand canonical simulations, $\mu_{\pm}^{(sim)} = \delta E \pm eV$, where e is the elementary charge, and δE contains the chemical potential of ions in the bulk of a supercapacitor. In all our simulations we took temperature $T = 328$K and the relative dielectric constant inside pores $\varepsilon_p = 2$.

To calculate differential capacitance, we differentiated the accumulated charge obtained from Monte Carlo simulations with respect to voltage numerically using the Holoborodko method with seven points (Holoborodko, 2008).

Chapter 6

Dynamics of Ion Transport in Ionic Liquids

Synopsis

A gap in understanding the link between continuum theories of ion transport in ionic liquids and the underlying microscopic dynamics has hindered the development of frameworks for the transport phenomena in these concentrated electrolytes. We construct a continuum theory of ion transport in ionic liquids by coarse graining a simple exclusion process defined on a lattice. The resulting dynamical equations can be written as a gradient flow with a degenerate mobility function. This form of the mobility function gives rise to charging behaviours that are different to those known in dilute electrolytic solutions; the predicted behaviours agree qualitatively with the phenomenology observed in experiments and simulations.

A paper based on some of the work described in this chapter has been published by *Physical Review Letters.* (Lee et al., 2015a)

6.1 Introduction

We saw in Chapter 2 that ionic liquids are concentrated electrolytes, and should not be modelled as a dilute electrolyte (with solvent consisting of ion-pairs), as had been suggested previously. Although the equilibrium structure of the electrical double layer in ionic liquids is relatively well studied, understanding the dynamic response of ionic liquids to an applied potential or surface charge is more challenging because of the difficulty in identifying an appropriate reference dynamics. While the continuum equations for ion transport in dilute electrolytes were derived by Nernst and Planck more than a century ago (Nernst, 1888; 1889; Planck, 1890), high ion concentrations make understanding ion transport in ionic liquids difficult, and a thermodynamically consistent extension of continuum transport equations to ionic liquids has remained elusive.

Previous theoretical studies (Kilic et al., 2007; Zhao, 2011; Jiang et al., 2014b;a; Yochelis, 2014b;a) relied on dynamical density functional theory (Marconi and Tarazona, 1999; 2000), in which the ion flux, $\mathbf{j}_\pm$, is related to the ion density field $\rho_\pm$ and free energy density functional $F[\rho_+, \rho_-]$ via

$$\mathbf{j}_\pm = -M_\pm \rho_\pm \nabla \left(\frac{\delta F}{\delta \rho_\pm} \right), \tag{6.1}$$

where $M_\pm$ is the cation/anion mobility, which is a constant. A key assumption in the derivation of (6.1) is that ion density is low compared to an underlying solvent bath (Español and Löwen, 2009). In particular, the dynamic density functional theory framework cannot reproduce the macroscopic limit of lattice dynamics.

This problem can be illustrated by considering a system of particles on a lattice with lattice constant a undergoing a simple exclusion process, where particles are hopping randomly on a lattice and can move between nearest-neighbour lattice sites at each step of the process, with the only constraint being that only one particle may occupy a given lattice site at any instant of time. It is worth noting that lattice gas models are commonly used as simple models of ionic liquids (Kilic et al., 2007; Kornyshev, 2007; Bazant et al., 2011; Zhao, 2011). The continuum limit of this kinetic process is well known, and leads to the linear diffusion equation $c_t = D\nabla^2 c$ for the particle density c (Spohn, 1991). However, substituting the lattice gas free energy $F = \frac{k_B T}{a^3} \int_V [a^3 c \log(a^3 c) + (1 - a^3 c) \log(1 - a^3 c)] \, \mathrm{d}^3 r$ into (6.1), and applying the continuity equation, we instead obtain

$$\frac{\partial c}{\partial t} = D \nabla \cdot \left(\frac{\nabla c}{1 - a^3 c} \right), \tag{6.2}$$

where $D \equiv M/k_B T$. The divergence in the mobility in (6.2) as $a^3 c \to 1$ shows that

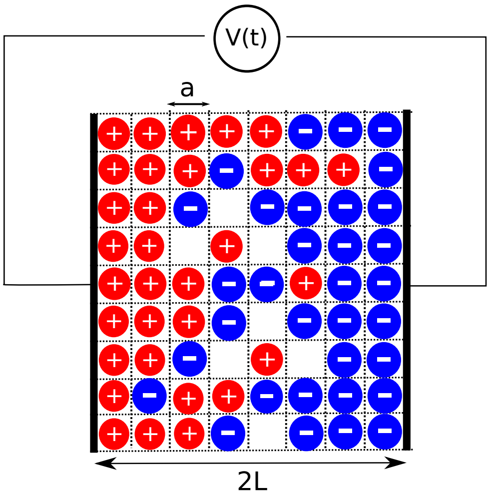

Figure 6.1: *Schematic of the system under consideration: cations and anions on a lattice of lattice constant a.*

the dynamics generated by dynamical density functional theory is very different from the dynamics of the reference lattice system.

6.2 Dynamics of an Interacting Two Component System

The goal of this Chapter is to derive a consistent model for ion transport in solvent-free ionic liquids based on the lattice Coulomb gas, and analyse the dynamics of electrical double layer formation. We map the system onto a lattice (see Figure 6.1) and take the continuum limit of the microscopic reference kinetics of a discrete symmetric exclusion process. Similar lattice reference kinetics were successfully used to model spinodal decomposition in alloys (Gouyet, 1993; Plapp and Gouyet, 1997; 1999; Gouyet et al., 2003; Petrishcheva and Abart, 2012), and were shown to be a microscopic basis for the continuum Cahn-Hilliard equation (Giacomin and Lebowitz, 1996; 1997; 1998).

We first consider a one-dimensional lattice of lattice constant a (corresponding to ion diameter a in the continuum limit) for simplicity, and later generalize our results to higher dimensions. We consider a discrete-time dynamics in which particles can only move between nearest-neighbour lattice sites between time t and $t+\Delta t$. Denoting by $S_i^\alpha(t) \in \{0,1\}$ the occupancy of the i^{th} lattice site at time t by ion of type $\alpha = \{+,-\}$, the evolution master equation for S_i^α reads

$$\begin{aligned} S_i^\alpha(t+\Delta t) = {} & r^\alpha_{i\to i+1} S_i^\alpha S_{i+1} + r^\alpha_{i+1\to i} S^\alpha_{i+1}(1-S_i) + r^\alpha_{i\to i-1} S_i^\alpha S_{i-1} \\ & + r^\alpha_{i-1\to i} S^\alpha_{i-1}(1-S_i) + \left(1 - r^\alpha_{i\to i+1} - r^\alpha_{i\to i-1}\right) S_i^\alpha, \end{aligned} \tag{6.3}$$

where the S_i^α on the right hand side are taken at time t and $S_i = S_i^+ + S_i^-$; $r_{i\to i\pm 1}^\alpha$ is unity if particle α at site i attempts to jump to site $i \pm 1$ and is zero otherwise: this transition propensity takes into account the long-ranged interparticle interactions as explained below. The first term of Eq. (6.3) ensures that there will be particle α at site i and time $t + \Delta t$, if it is there at time t, attempts to move to site $i + 1$ and finds that site occupied. The second term describes a possible transition from site $i+1$ to site i when there is no particle at site i. The third and forth terms describe the same processes between sites i and $i - 1$. Finally, the last term corresponds to a particle α at site i that does not attempt to leave it during the interval Δt.

An ensemble average of $r_{i\to j}^\alpha$ with $|i - j| = 1$ gives a transition rate that satisfies the detailed balance and can thus be related to the Boltzmann factor by

$$\langle r_{i\to j}^\alpha \rangle = \frac{1}{2} e^{-(V_j^\alpha - V_i^\alpha)/2k_B T}, \tag{6.4}$$

where

$$V_i^\alpha = \sum_{j\neq i} \sum_\beta U_{\alpha\beta}(|i-j|) S_j^\beta \tag{6.5}$$

is a potential acting on particle α at site i due to all remaining particles, and $U_{\alpha\beta}(|i-j|)$ is the microscopic (electrostatic) interaction potential between the particles. In the absence of long-ranged interactions ($U_{\alpha\beta} = 0$), there is no preferred direction of motion, thus $\langle r_{i\to i\pm 1}^\alpha \rangle = 1/2$.

To obtain an ensemble averaged evolution equation, we rescale the lattice indices by the lattice spacing a, and define $x = ai$. Denoting by $\rho_\alpha(x) = \langle S^\alpha(x) \rangle$ the ensemble average, we apply the mean field approximation $\left\langle S^\alpha(x) S^\beta(y) \right\rangle \approx \langle S^\alpha(x) \rangle \left\langle S^\beta(y) \right\rangle$ and $\left\langle r_{i\to j}^\alpha \right\rangle \approx \exp\left[- \left(\left\langle V_j^\alpha \right\rangle - \left\langle V_i^\alpha \right\rangle \right) / (2k_B T) \right] / 2$.

In the continuum limit one obtains

$$\langle S^\alpha(t + \Delta t) \rangle = \rho_\alpha(t) + \Delta t \frac{\partial \rho_\alpha}{\partial t} + O(\Delta t^2), \tag{6.6}$$

$$\left\langle S_{i\pm 1}^\alpha \right\rangle = \rho_\alpha(x) \pm a \frac{\partial \rho_\alpha}{\partial x} + \frac{a^2}{2} \frac{\partial^2 \rho_\alpha}{\partial x^2} + O(a^3), \tag{6.7}$$

and

$$V_i^\alpha \approx \mu_\alpha(x) \equiv \int U(|x - x'|)(\rho_\alpha(x') - \rho_\beta(x')) \frac{\mathrm{d}x'}{a}. \tag{6.8}$$

where we have ignored the (constant) self-energy contribution. The transition probability (6.4) can be simplified by assuming that the local potential is a smoothly varying function in the continuum limit, thus expand the exponential using Taylor series and obtain

$$\begin{aligned}\langle r^{\alpha}_{i\to i\pm 1}\rangle &\approx \frac{1}{2}-\frac{1}{4k_BT}(V^{\alpha}_{i\pm 1}-V^{\alpha}_{i})+...\\ &\approx \frac{1}{2}-\frac{1}{4k_BT}\left[\mu_\alpha(x\pm a)-\mu_\alpha(x)\right]\\ &= \frac{1}{2}-\frac{1}{4k_BT}\left(\pm a\frac{\partial \mu_\alpha}{\partial x}+\frac{a^2}{2}\frac{\partial^2\mu_\alpha}{\partial x^2}+\cdots\right),\end{aligned} \tag{6.9}$$

and similarly for $\langle r_{i\pm 1\to i}\rangle$. After some algebra we arrive at

$$\frac{1}{D}\frac{\partial \rho_\alpha}{\partial t}=\rho_\alpha\frac{\partial^2\rho}{\partial x^2}+(1-\rho)\frac{\partial\rho_\alpha}{\partial x}+\beta\rho_\alpha(1-\rho)\frac{\partial^2\mu_\alpha}{\partial x^2}-\beta\left[\rho_\alpha\frac{\partial\rho}{\partial x}-(1-\rho)\frac{\partial\rho_\alpha}{\partial x}\right]\frac{\partial\mu_\alpha}{\partial x}, \tag{6.10}$$

where we have defined $\rho\equiv\rho_+ + \rho_-$, and identified $D=a^2/(2\Delta t)$ as the self-diffusion coefficient.

Equation (6.10) can be generalised to three dimensions by replacing derivatives by gradient and divergence operators (as the fluxes in the x, y and z directions are de-coupled), and may be rewritten in matrix form

$$\partial_t \boldsymbol{c}=\nabla\cdot\left[\mathcal{D}\nabla\boldsymbol{c}+\mathcal{M}\nabla\boldsymbol{\mu}\right], \tag{6.11}$$

where $\boldsymbol{c}=[c_\alpha,c_\beta]\equiv a^{-3}[\rho_\alpha,\rho_\beta]^T$ is the concentration of cations and anions,

$$\mathcal{M}=\frac{D}{k_BT}\begin{pmatrix} c_\alpha(1-a^3c) & 0\\ 0 & c_\beta(1-a^3c)\end{pmatrix} \tag{6.12}$$

is the mobility matrix, $c\equiv c_\alpha+c_\beta$, and

$$\mathcal{D}=D\begin{pmatrix} 1-a^3c_\beta & a^3c_\alpha\\ a^3c_\beta & 1-a^3c_\alpha\end{pmatrix} \tag{6.13}$$

is the diffusion matrix. The first term in Equation (6.11) is the flux of ions due to a concentration gradient, and the second term is the flux due to long-ranged interactions. We now observe that

$$\mathcal{S}=-\frac{1}{T}\,\mathcal{M}^{-1}\mathcal{D} \tag{6.14}$$

is the Hessian of the lattice gas entropy

$$s(c_+,c_-)=-\frac{k_B}{a^3}\left[\sum_{\alpha=\pm}a^3c_\alpha\log(a^3c_\alpha)+(1-a^3c)\log(1-a^3c)\right]. \tag{6.15}$$

Thus, using Equations. (6.11) and (6.14), we arrive at

$$\partial_t \boldsymbol{c} = \nabla \cdot (\mathcal{M} \nabla \tilde{\boldsymbol{\mu}}), \tag{6.16}$$

where $\tilde{\mu}_\alpha = \delta \mathcal{F} / \delta c_\alpha$ and

$$\mathcal{F}[\{\rho_\alpha\}] = \sum_{\alpha\beta} \int_V c_\alpha(\mathbf{r}_1) U_{\alpha\beta}(|\mathbf{r}_1 - \mathbf{r}_2|) c_\beta(\mathbf{r}_2) \, \mathrm{d}^3\mathbf{r}_1 \mathrm{d}^3\mathbf{r}_2 - T \int_V s(c_\alpha, c_\beta) \, \mathrm{d}^3\mathbf{r}. \tag{6.17}$$

Equation (6.16) is the continuum kinetic equation for an interacting two component system. Note the important physical constraint that the evolution equation for the total concentration c, in the absence of any interactions ($U_{\alpha\beta} = 0$), reduces to the linear diffusion equation. This constraint, as explained above, respects the fact that the underlying dynamics of our reference system is the simple exclusion process on a lattice.

6.3 Continuum Electrokinetic Equations

To apply Equation (6.16) to an ionic liquid system, we introduce a characteristic length scale l_c for short-ranged interactions, and split the Coulomb potential $v_{\alpha\beta} = v^{sr}_{\alpha\beta} + v^{lr}_{\alpha\beta}$, where $v^{sr}_{\alpha\beta}(r) = q_\alpha q_\beta l_B e^{-r/l_c}/r$ and $v^{lr}_{\alpha\beta}(r) = q_\alpha q_\beta l_B (1 - e^{-r/l_c})/r$, where $l_B = q^2/(\epsilon k_B T)$ is the Bjerrum length. Below the length scale l_c, it is actually the hard core exclusion that matters rather than Coulomb interaction, thus v^{sr} is neglected. This truncation of the Coulomb potential is necessary as the mean-field model underestimates steric correlations, and as such the divergence of the Coulomb interaction at the origin renders electrostatic interactions effectively *too strong*. A natural estimate is $l_c = a$, so that

$$\frac{U^{\mathrm{eff}}_{\alpha\beta}(\mathbf{r}_1, \mathbf{r}_2)}{k_B T} \approx q_\alpha q_\beta l_B \frac{1 - e^{-|\mathbf{r}_1 - \mathbf{r}_2|/l_c}}{|\mathbf{r}_1 - \mathbf{r}_2|}. \tag{6.18}$$

This decomposition of the Coulomb potential is not unique — the exponential function is chosen phenomenologically for mathematical convenience. We note that the idea of decomposing of the Coulomb interaction into short and long-ranged parts has been used by Chen and Weeks (2006); Santangelo (2006) as a perturbative method to solve the path integral (2.13) in Chapter 2.

To further simplify the system, we note that the chemical potential $\mu_\pm = \delta F / \delta \rho_\pm$ is given by

$$\frac{\mu_\pm}{k_B T} = \pm u + \log\left(\frac{a^3 c_\pm}{1 - a^3 c}\right); \tag{6.19}$$

where we have defined the local electric potential

$$u(\mathbf{r}) = \beta \int_V [c_+(\mathbf{r}') - c_-(\mathbf{r}')] U_{++}^{\text{eff}}(|\mathbf{r} - \mathbf{r}'|) \, \mathrm{d}^3\mathbf{r}'. \tag{6.20}$$

Recalling that $(1 - l_c^2 \nabla^2)\nabla^2 \left[(1 - e^{-|\mathbf{r}_1 - \mathbf{r}_2|/l_c})/(|\mathbf{r}_1 - \mathbf{r}_2|)\right] = -4\pi\delta(\mathbf{r}_1 - \mathbf{r}_2)$, we can rewrite the integral equation (6.20) as a differential equation

$$(1 - l_c^2 \nabla^2)\nabla^2 u = -4\pi l_B (c_+ - c_-), \tag{6.21}$$

and rearrange (6.16) in terms of u. We find that

$$\begin{aligned} \frac{\partial c_\pm}{\partial t} &= D\nabla \cdot \left[\pm c_\pm (1 - a^3 c)\nabla u + (1 - a^3 c)\nabla c_\pm + a^3 c_\pm \nabla c\right] \\ &= D\nabla \cdot \left\{ c_\pm (1 - a^3 c) \nabla \left[\pm u + \log\left(\frac{a^3 c_\pm}{1 - a^3 c} \right) \right] \right\}. \end{aligned} \tag{6.22}$$

Note that Equation (6.21) is identical to the modified Poisson equation derived by Bazant et al. (2011), which was based on gradient expansion of a nonlocal electrostatic kernel.

6.4 Charging by a Step Voltage

To gain insight into the characteristic behaviour of the system (6.21)-(6.22), we turn our attention to a simple one-dimensional problem: Consider an ionic liquid with bulk concentration $c = c_0$ bounded by two parallel, blocking electrodes at $x = -L, L$. Initially the concentration of the two ion species are uniform, and a step voltage of amplitude $2V$ is applied at $t = 0$. Introducing the Debye length $l_D = 1/\sqrt{8\pi c_0 l_B}$, packing fraction $\gamma = a^3 c_0$, and dimensionless length scales $\delta_c = l_c/L$ and $\delta_D = l_D/L$, we will use dimensionless variables $\tau = (D/L l_D)t$, $X = x/L$, and $C_\pm = c_\pm/c_0$. The no-flux condition at the electrodes are

$$\pm C_\pm (1 - \gamma C)\frac{\partial u}{\partial X} + (1 - \gamma C)\frac{\partial C_\pm}{\partial X} + \gamma C_\pm \frac{\partial C}{\partial X}\bigg|_{X=\pm 1} = 0. \tag{6.23}$$

At the surface of the electrodes, we posit that the classical Gauss law $-\epsilon u_x = 4\pi\sigma$ holds, with σ the (dimensional) surface charge density, and ϵ the dielectric constant of the medium (Bazant et al., 2011; Storey and Bazant, 2012). This condition, together with the constant potential condition gives

$$u(X = \pm 1, \tau) = \pm V, \; u_{XXX}(X = \pm 1, \tau) = 0, \; \tau > 0. \tag{6.24}$$

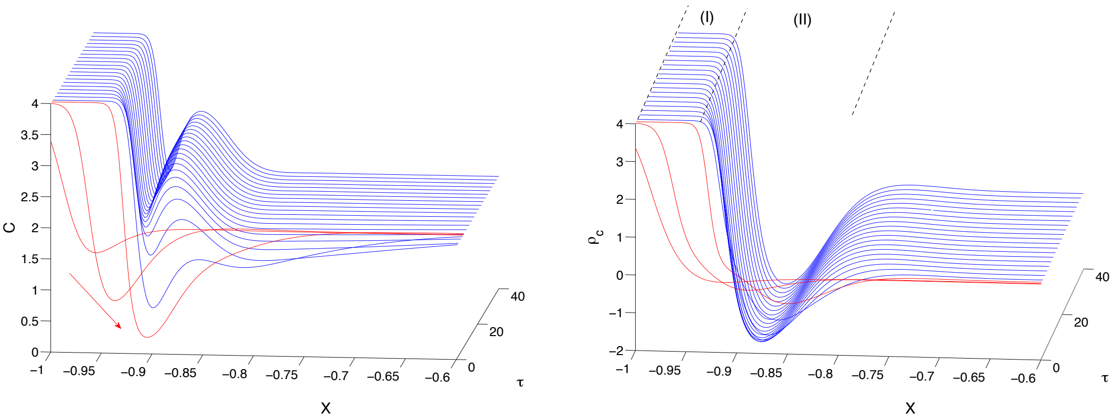

(a) (b)

Figure 6.2: *a) The total density $C \equiv C_+ + C_-$, and b) charge density $\rho_c \equiv C_+ - C_-$, as a function of distance X away from the electrode and time. Both a) and b) are plotted with parameters $\gamma = 0.25$, $\delta_c/\delta_D = 10$ as estimated in the main text, and $\delta_D = 0.01$. The red/blue curves denotes the first/second charging regimes, and the arrow shows the increasing density deficit in the first charging regime. Numerical solution of the coupled partial differential equations was done using the `pdepe` package in Matlab.*

The initial conditions are

$$C_\pm(X, 0) = 1, \; X \in [-1, 1]. \tag{6.25}$$

To avoid complications of double layer overlap, we consider widely separated electrodes ($\delta_D \ll 1$) taking $\delta_D = 0.01$. From the estimate $l_c = a$, Bjerrum length $l_B = 50\mathring{A}$, ion diameter $a = 5\mathring{A}$ and assuming an ion packing fraction of $\gamma = 0.25$ (see *e.g.* Bazant et al., 2011), we have $\delta_c/\delta_D = \sqrt{8\pi\gamma l_B/a} \approx 10$. We solve the resulting 1D parabolic-ecliptic PDE system using the Matlab package `pdepe` (see Appendix A for details about the numerical method).

Figure 6.2 shows that charging proceeds via two distinct regimes: First, the (negative) electrode attracts cations from the vicinity and expels anions, resulting in a dense, “compact layer” of cations near the electrode that overcompensates the surface charge (region I in Figure 6.2). Ion diffusion is hindered as the mobility matrix (6.12) vanishes in regions of high density. As a result, the total density reaches a minimum away from the compact layer (*c.f.* red arrow in Figure 6.2a). In the second stage, anions arrive from the bulk to screen the now net-positive compact layer. This flux fills the total density deficit near the compact layer incurred in the first charging regime, creating a region of negative charge density and in fact excess total density (region II in Figure 6.2b).

A key measure of practical interest is the integrated total diffuse charge,

$$Q(t) = \int_{-1}^{0} \rho_c(x, t) \, \mathrm{d}x. \tag{6.26}$$

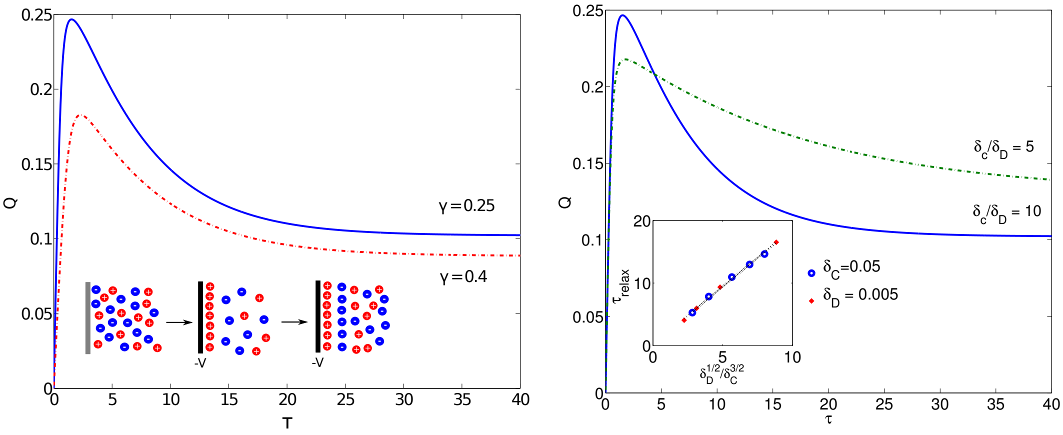

(a)

(b)

Figure 6.3: *a) (Main panel) The total charge as a function of time for different packing fractions γ; (Inset) A schematic of the charging mechanism. b) (Main panel) The total charge as a function of time for different values of δ_c/δ_D with $\delta_D = 0.01$, $\gamma = 0.25$ fixed. (Inset) The relaxation time towards equilibrium τ_{relax} as a function of δ_c and δ_D (obtained by fitting the numerical data to the exponential function $Q = Q_\infty + Q_1 e^{-\tau/\tau_{\text{relax}}}$.*

Figure 6.3a and b show that, as charging proceeds, the total charge initially increases, corresponding to the formation of the compact layer. However, arrival of anions in the second charging regime decreases the charge to the final equilibrium value. This charging mechanism is schematically illustrated in Figure 6.3a. Increasing the packing fraction γ decreases the charge stored in the compact layer, and the peak diffuse charge decreases. The correlation length δ_c/δ_D controls the extent of overcompensation of electrode surface charge by the compact layer. Therefore, decreasing the correlation length reduces the extent of charge overcompensation and also the peak diffuse charge (Figure 6.3b).

Further insights into the charging process can be obtained by noting that the initial rise in charge occurs over $\tau \sim O(1)$. In dimensional terms this corresponds to $t = Ll_D/D$, a usual RC timescale for double layer charging in dilute electrolytes (Bazant et al., 2004). Following Bazant et al. (2004), this timescale can be derived by considering the charging process as charging a capacitor (the interfacial double layer) in series with a resistor (the bulk solution): The bulk conductivity is related to the concentration of charge carrier c_0 via $\sigma_b = 2e^2 c_0 \mu$, where μ is the mobility. Using the Einstein's relation $\mu = D/(k_B T)$ (*n.b.* Equation (6.14) is the multicomponent generalisation of this relation), we arrive at $\sigma_b = 2e^2 c_0 D/(k_B T)$. Therefore, the bulk resistance is

$$R_b = \frac{V}{J} = \frac{LE_0}{\sigma_b E_0} = \frac{l_D^2 L}{\epsilon D}, \tag{6.27}$$

where J is the current, and E_0 is the bulk electric field. The double layer capacitance, in the linear regime, can be considered as that of a parallel plate capacitor with plate separation

l_D (the electrode acts as one plate, and the barycentre of the excess ion concentration acts as the other), thus

$$C_{DH} = \frac{\epsilon}{l_D}. \tag{6.28}$$

Therefore, $t = Ll_D/D = C_{DH}R_b$ is timescale of charging for dilute electrolytes, corroborating the fact that the peak in diffuse charge Q has its origin in the formation of a compact layer of counterions near the electrode.

Numerical experiments (see inset of Figure 6.3b) suggest that the late-stage exponential relaxation of the charge to equilibrium has a distinctly different timescale

$$\tau_{\text{relax}} \sim \frac{\delta_D}{\delta_c}\frac{1}{\sqrt{\delta_c\delta_D}}. \tag{6.29}$$

This scaling confirms that the decay in stored charge comes from the formation of charge oscillations, where the strong Coulomb correlations come into play: δ_c/δ_D is the characteristic steric correlation length, and $\sqrt{\delta_c\delta_D}$ is a characteristic wavelength of the oscillations (*c.f.* Equation (6.21)). Indeed, setting $\delta_c = 0$, and hence neglecting strong Coulomb interactions, the charge profiles remains monotonic and the diffuse charge increases monotonically to the equilibrium value (see Figure 6.4). Note that for $\delta_c = 0$, charging is complete when $\tau = 1$, the RC time constant.

The non-monotonic charging seen in Figure 6.3 is due to combining the mobility (6.12) with strong Coulomb correlations ($\delta_c \neq 0$). In fact, dynamical density functional theory (6.1), where the mobility matrix is given by

$$\mathcal{M}_{\text{ddft}} = \frac{D}{k_BT}\begin{pmatrix} c_\alpha & 0 \\ 0 & c_\beta \end{pmatrix}, \tag{6.30}$$

predicts a monotonic evolution of $Q(t)$, in contrast to the results predicted by our model (Zhao, 2011). The degenerate mobility (6.12) in our approach ensures that the flux due to electrostatic interactions vanishes at close packing, and thus there are distinct regimes of initial charge density polarisation and, at later times, rearrangement of the double layer into cation-rich and anion-rich layers. Molecular dynamics simulation of molten salts undergoing discharging (Lanning and Madden, 2004) agrees qualitatively with our prediction that charge polarisation occurs over a much faster timescale than relaxation via bulk diffusion; quantitive comparison will be the subject of future work.

Interestingly, Jiang et al. (2014a) reported a non-monotonic evolution of diffuse charge in the limit where the double layers can overlap. Our calculations show that the phenomenon of “kinetic charge inversion” is a general feature of strong electrostatic correlations.

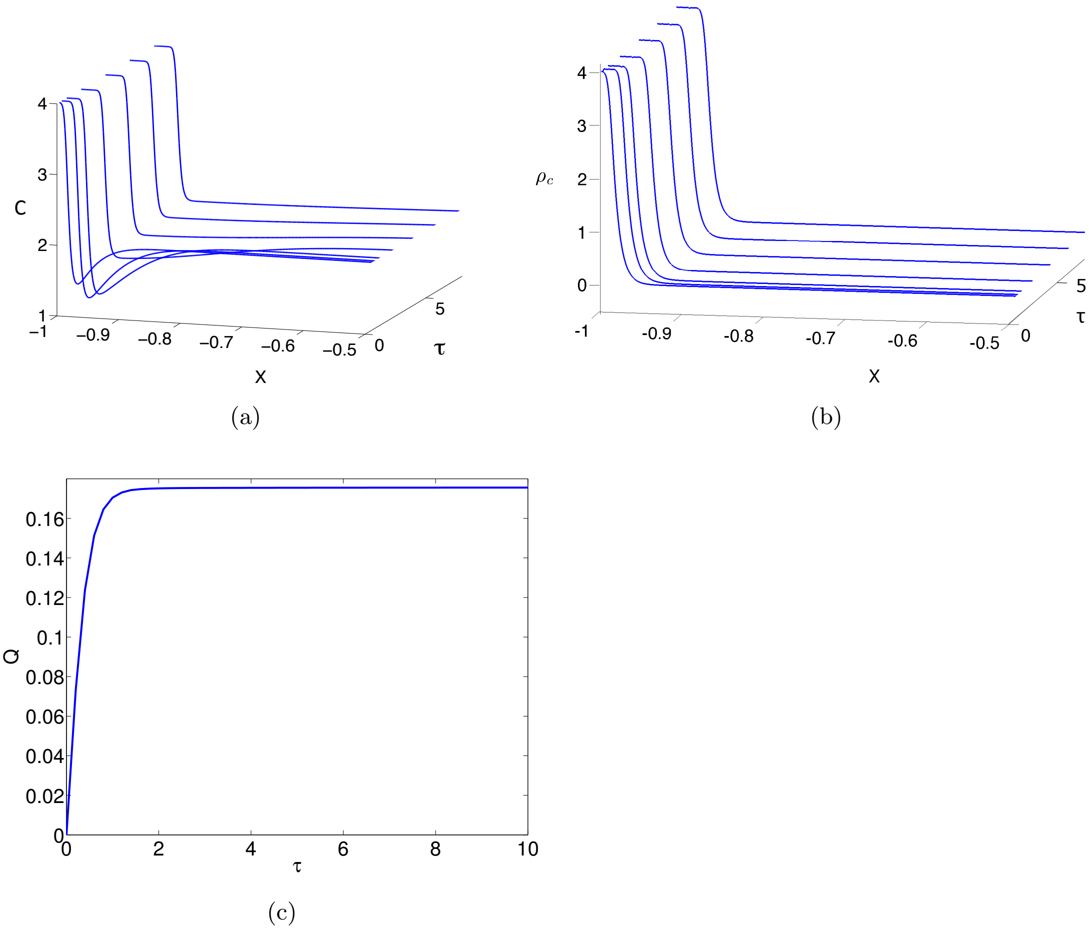

(a)

(b)

(c)

Figure 6.4: *The charge and density profile with strong electrostatic correlation neglected ($\delta_c = 0$), and $\delta_d = 0.01$, $\gamma = 0.25$. a) The total density $C \equiv C_+ + C_-$, and b) charge density $\rho_c \equiv C_+ - C_-$, as a function of distance X away from the electrode and time. c) The total charge as a function of time for different packing fractions.*

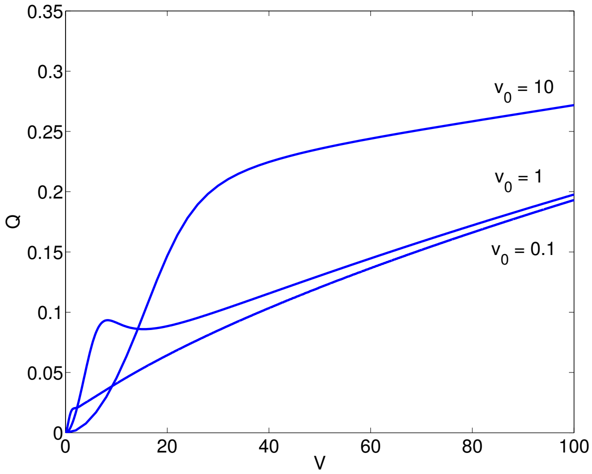

Figure 6.5: *The charge stored in the electrical double layer is non-monotonic for a time-dependent applied potential that increases linearly in time. The parameters used in the numerical calculations are* $\gamma = 0.25$*,* $\delta_c/\delta_D = 10$*, and* $\delta_D = 0.01$*.*

6.5 Far from Equilibrium Charging

The effect of strong electrostatic correlations becomes more pronounced when the system is driven far away from equilibrium by time-dependent boundary conditions. We first consider a time-dependent applied potential difference, akin to a linear-sweep voltammetry experiment. For simplicity, we consider an applied potential that increases linearly in time, *i.e.*

$$u(X = \pm 1, \tau) = \pm v_0 \tau. \tag{6.31}$$

Figure 6.5 shows that the integrated total diffuse charge is a non-monotonic function of voltage when $v_0 = O(1)$. This non-monotonic variation in stored charge (effectively a "negative capacitance") is due to the sequential formation of alternating layers of counterion and co-ion next to the electrode. For $v_0 \ll 1$ (slow charging), the system is in quasi-equilibrium hence thermodynamic stability dictates that Q increases monotonically with V. In the opposite limit of $v_0 \gg 1$ (fast charging), the co-ion layer adjacent to the compact layer does not have time to form — the system continuously pulls in counterions to quench the rapidly increasing potential and thus the charge-voltage curve is still monotonic. This effect shows again that the timescale for the formation of the compact layer is the RC time, hence this negative capacitance is only seen when the timescale of voltage increase is on the same order as the RC time, *i.e.* $v_0 = O(1)$.

Another way to drive the system out of equilibrium is via imposing a constant current, *i.e.*

$$\left.\frac{\partial u}{\partial X}\right|_{X=\pm 1} = \pm J\tau. \tag{6.32}$$

Figure 6.6a shows that the non-equilibrium double layer rearrangement manifests itself in the non-monotonic evolution of the potential drop across the system when the current density J is large. Figure 6.6b shows that charging commences initially via counter-ion arriving to screen the electrode charge. The first minima in the potential drop is reached when co-ions starts to build up adjacent to the counter-ion layer. This process continues with sequential growth space charge layers with net charges of alternating signs near the electrode wall, causing oscillations in the potential. This charging mechanism is similar to that seen in Figure 6.3 and 6.5.

The theoretical predictions agrees qualitatively with recent molecular dynamics simulations by Jiang et al. (2014c), which show that the voltage drop across the system evolves non-monotonically when the electrode charge is increased linearly with time (Figure 6.6c). These simulations were performed with equisized (radius 0.5 nm) and unit-charged Lennard-Jones particles. The electrode walls were modelled as a square lattice of homogeneously charged Lennard-Jones particles with a lattice spacing of 0.33nm. We note that this non-monotonic evolution of potential drop cannot be obtain via conventional dynamical density functional theory with mobility function (6.30), which would predict a monotonic increase in potential drop as a function of time (Jiang et al., 2014c).

Although the response of the system to charge-controlled charging is similar to potential-controlled charging, the former is significantly more pronounced than the latter. Heuristically, this is because charge fluctuations and potential fluctuations are related via $\delta Q = C\delta V$, where C is the differential capacitance. Ionic liquid systems enjoy large capacitance due to the formation of an electrical double layer, and therefore small fluctuations in V manifest themselves in large fluctuations in Q; however, large fluctuations in Q manifest only in small fluctuations in V. Therefore, current/charge controlled experiments (where V can fluctuate) may be a more suitable experimental technique to probe the non-equilibrium physics of ionic liquids.

6.6 Conclusion

In summary, we have derived an continuum theory for ion transport in solvent-free ionic liquids based on coarse-graining the reference dynamics of a simple exclusion process defined on a lattice. The resulting equations have the structure of a gradient flow with a degenerate mobility function. As an example, these equations are analysed for a system

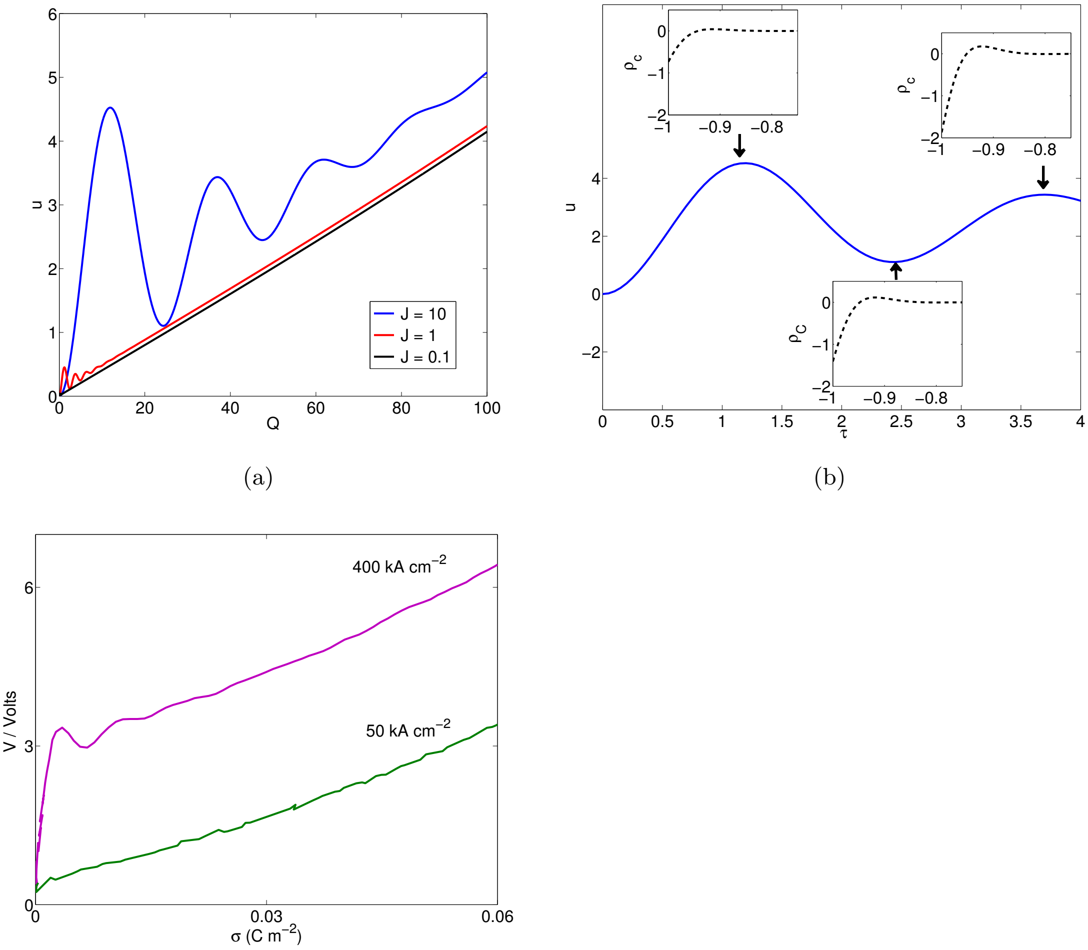

(a)

(b)

(c)

Figure 6.6: *a) The voltage drop across the system evolves non-monotonically under constant current charging conditions,* (6.32)*. b) The charge density profile near the electrode at different times for* $J = 10$*. The parameters used in the numerical calculations are* $\delta_D = 0.01$*,* $\delta_c/\delta_D = 10$ *and* $\gamma = 0.25$*, and the total electrode charge* $Q = J\tau$*. c) The evolution of potential difference obtained using non-equilibrium molecular dynamics simulations of Jiang et al. (2014c). Note that in dimensional units* $J = 1$ *corresponds to current density* $\approx 200\mathrm{kAcm}^{-2}$.

where a step voltage is applied between widely separated electrodes, and for constant-current charging and linear sweep voltammetric experiments. Even in those simple cases, our theory qualitatively differs from previously developed theories for electrolyte solutions. Importantly, we show that the total diffuse charge may, in general, be a non-monotonic function of time. Experiments and simulations on electrokinetic transport in ionic liquids are currently scarce, and we hope that our theory provides a framework to interpret experiments and motivate further investigation.

Appendix 6.A Numerical Method

We solve 1D parabolic partial differential equation system (6.21)-(6.22) numerically using the `pdepe` package in Matlab R2012b, with Equation (6.21) written as two coupled second order partial differential equations for u and $w = u_{XX}$

$$\delta_D^2 u_{XX} - w = 0,$$
$$\delta_c^2 w_{XX} - w - \rho = 0.$$

The `pdepe` package discretises spatial derivatives using finite differences and the resulting coupled PDEs are propagated using the implicit time stepping scheme `ode15s` with default error tolerances.

To resolve the boundary layers near the electrode surfaces, we use a non-linear map $y \in [0,1] \to X \in [-1,1]$

$$X = \frac{\tanh[\delta(y-0.5)]}{\tanh(\delta/2)} \tag{6.33}$$

where δ is a parameter that determines the degree of localisation of the mesh near the boundaries of the interior domain, with a larger value of δ corresponding to greater degree of localisation of mesh points about the domain boundary. In the computation reported in the main text, the mesh is generated by setting y to be 1000 equi-spaced points, and $\delta = 4$ is used for $\delta_D = 0.01$, and $\delta = 8$ is used for $\delta_D = 0.001$. Numerical experiments show that that refining the mesh further does not change the numerical result.

Chapter 7

Disjoining Pressure in Active Non-equilibrium Fluids

Synopsis

Many important physical phenomena, ranging from hydrodynamic turbulence to the collective behaviour of bacteria, are intrinsically far from equilibrium and hence cannot be described by equilibrium statistical physics. Despite their ubiquity, there are few general theoretical results that describe these non-equilibrium steady states. Here, we argue that a generic signature of non-equilibrium systems is a nontrivial fluctuation spectrum. Based on this observation, we derive a general relation for the force exerted by a non-equilibrium system on two embedded walls. We find that for a narrow, unimodal spectrum, the force law can be characterised in terms of the width and the position of the peak in the fluctuation spectrum, and will, in general, oscillate between repulsion and attraction. We demonstrate the generality of our framework by examining two apparently disparate examples. First, we study the spectrum of wind-water interactions on the ocean surface to reveal force oscillations underlying the maritime Casimir effect. Second, we demonstrate quantitative agreement with force generation in recent simulations of active Brownian particles. A key implication of our work is that important non-equilibrium interactions are encoded in the fluctuation spectrum. In this sense, the noise becomes the signal.

7.1 Introduction

Active, non-equilibrium systems are realised in many physical and biological processes. In such systems, non-equilibrium steady states are sustained by the input of energy. Examples range from external mechanical driving, as in the case of turbulence, to chemical gradients and high-energy chemical bonds, which many microswimmers, synthetic and natural alike, use as the means of propulsion. Indeed, life itself is an example of such a non-equilibrium system.

The diverse physical mechanisms leading to non-equilibrium steady states have motivated many studies that focus on the microscopic physics of the respective system. Unlike the equilibrium counterpart, the requirement of energy input into non-equilibrium steady states places convenient statistical concepts, such as the partition function and the free energy, on more tenuous ground. In fact, theories and simulations of active Brownian particles show that self-propulsion induces complex phase behaviour qualitatively different from the passive analogue (Fily and Marchetti, 2012; Redner et al., 2013; Stenhammar et al., 2013; Buttinoni et al., 2013; Cates and Tailleur, 2015).

Long-ranged non-equilibrium forces are well known for chemotactic colloidal systems (Saha et al., 2014; Soto and Golestanian, 2014), where the colloid emits chemicals through, for example, surface-induced chemical processes. In such scenarios, the concentration field of chemicals produced by one colloid generates a attractive/repulsive phoretic force on neighbouring colloids. In fact, as the concentration of chemical near a colloid satisfies a diffusion equation, the concentration gradient decays as $1/r$ (in 3D) where r is the distance away from the colloid. Therefore, if the phoretic force is linearly proportional to the concentration gradient of chemicals, active chemotactic systems can be seen as the non-equilibrium generalisation of ionic liquids.

Surprisingly, even in the absence of any long-ranged chemotactic interactions, Ni et al. (2015) recently reported a *long-ranged* and oscillatory force between two hard slabs submerged in a fluid of active Brownian hard spheres. This observation suggests that non-equilibrium activity of particles may be enough to generate an effective interaction between inclusions.

Part of the difficulty in understanding the plethora of non-equilibrium phenomena is that there are very few general results that are broadly applicable to non-equilibrium systems; those that are known principally pertain to the linear response regime close to equilibrium (see Mazur and de Groot, 1963; Zwanzig, 2001), or to fluctuation relations for small systems (Jarzynski, 1997; Crooks, 1999). In this Chapter, we argue that there is an analogy between active fluids and the passive, strongly correlated fluids that we have considered in previous Chapters. In particular, we have shown in Chapter 4 that the disjoining pressure, as measured using the surface force balance, is a useful way to unravel the structure of a Coulomb fluid at equilibrium. Here, we will show how the disjoining pressure allows us to develop a unifying framework for non-equilibrium system.

7.2 Spectral Density and Disjoining Force

We begin with the question: How can we distinguish a suspension of pollen at thermal equilibrium from a suspension of active microswimmers? A natural means of monitoring fluctuations uses dynamic light scattering (Chu, 1974). A general feature of the macroscopic view of physical systems is that fluctuations are intrinsic and are the result of statistical averaging over microscopic degrees of freedom. The magnitude of this intrinsic noise can, in general, be a function of the frequency; the resulting fluctuation spectrum is one key signature of a particular physical system.

Although the fluctuation spectrum can be derived from microscopic kinetic processes, here we are interested in how the general properties of such spectra can provide a framework for understanding nonequilibrium behaviour. Equilibrium thermal fluctuations, such as that for our Brownian suspension or the Johnson–Nyquist noise (Nyquist, 1928), are usually associated with white noise corresponding to equipartition of energy between different modes. The key insight is that non-equilibrium processes have the potential to generate a nontrivial (even non-monotonic) fluctuation spectrum. A classical example from hydrodynamics concerns ocean waves that are driven to a non-equilibrium steady state via wind-wave interactions. The non-equilibrium fluctuation spectrum of ocean waves is well described by

$$G(k) = \frac{\alpha\rho g}{2k^3} \exp\left[-\beta\left(\frac{k_0}{k}\right)^2\right], \tag{7.1}$$

where ρ is the density of water, g is gravitational acceleration, $k_0 = g/U^2$, U is the wind speed, and $\alpha = 0.0081$ and $\beta = 0.74$ are fitted parameters (Pierson and Moskowitz, 1964).

As energy can be difficult to define for an active system, a natural macroscopic quantity for non-equilibrium systems is the disjoining force — the force exerted by the medium on embedded bodies. The relation between fluctuation spectra and disjoining force is fruitfully examined by considering a one-dimensional system consisting of two plates of length W separated by a distance L and immersed in the non-equilibrium medium. The fluctuation imparts an effective radiative stress, with the collective waves caused by the fluctuations being reflected by the plates. Noting that the fluctuation spectrum $G(k)$ is related to the wave energy density E via

$$G(k) = \frac{\mathrm{d}E}{\mathrm{d}k}, \tag{7.2}$$

the radiation force per unit plate length due to waves with wavenumber between k and $k + \Delta k$, with angle of incidence between θ and $\theta + \Delta\theta$, is

$$\delta F = G(k)\delta k \cos^2\theta \frac{\delta\theta}{2\pi}. \tag{7.3}$$

One factor of cosine in Equation (7.3) is due to projecting the momentum in the horizontal direction, the other one due to momentum being spread over an area larger than the cross sectional length of the wave, and the factor of 2π accounts for the force per unit angle. For isotropic fluctuations, we can consider $\delta\theta$ as an infinitesimal quantity and, upon integrating from $\theta = -\pi/2$ to $\pi/2$, we arrive at

$$\delta F = \frac{1}{4} G(k)\delta k. \tag{7.4}$$

Outside the plates, the waves can take any wavenumber, thus the total force is given by

$$F_{\text{out}} = \frac{1}{4}\int_0^\infty G(k)\mathrm{d}k. \tag{7.5}$$

However, inside the plates the wavenumber can only take integer multiples of $\Delta k = \pi/L$ (because we assume that the waves are reflected by each plate). Therefore, the force imparted by the waves to the inner surface of the plate is

$$F_{\text{in}} = \sum_{n=0}^{\infty} G(n\Delta k)\Delta k, \tag{7.6}$$

and the net disjoining force is given by

$$F_{\text{fluct}} = F_{\text{in}} - F_{\text{out}} = \frac{1}{4}\left[\frac{\pi}{L}\sum_{n=0}^{\infty} G\left(\frac{n\pi}{L}\right) - \int_0^\infty G(k)\mathrm{d}k\right]. \tag{7.7}$$

7.3 Maritime Casimir Force

We illustrate the central result, Equation (7.7), by applying it to the ocean-wave spectrum Equation (7.1). Figure 7.1a shows that the resulting force is non-monotonic, and the force can be *repulsive* ($F_{\text{fluct}} > 0$) as well as attractive ($F_{\text{fluct}} < 0$). Physically, the origin of the attractive force is akin to the Casimir force between metals — the presence of walls

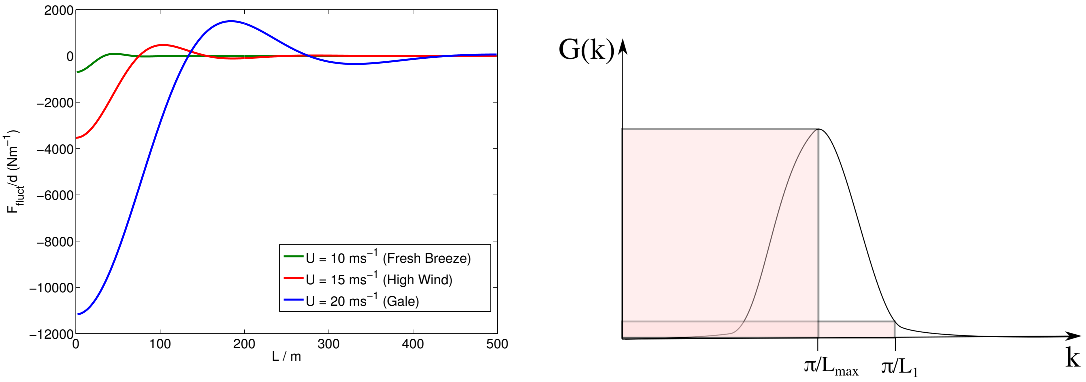

(a) (b)

Figure 7.1: *(a) The fluctuation-induced force per unit length for different wind velocities, with the qualitative descriptors taken from the Beaufort scale (Beer, 1996). (b) The disjoining force is the difference between the integral over the noise spectrum (area under the curve), and the Riemann sum (the shaded regime). The plot shows graphically that the sum overestimates the integral when one "grid point" coincides with* $k_{\text{max}} = \pi/L_{\text{max}}$.

restricts which modes are allowed in the interior, so that the energy density outside the walls is greater than that inside. In the limit $L \to 0$, fluctuations inside the plates are suppressed, and $F_{\text{fluct}} = -F_{\text{out}} = -\rho_w W \alpha U^4/(16\beta g)$. This attractive "Maritime Casimir" force has been observed since antiquity (*e.g.*, Boersma, 1996, and refences therein) and experimentally measured in a wavetank (Denardo et al., 2009).

However, the *non-monotonicity* of the spectrum gives rise to an *oscillatory* force-displacement curve. In particular, the force is repulsive when one of the allowed discrete modes is close to the peak wavenumber of the spectral density (see Figure 7.1b), since the sum overestimates the integral in Equation (7.7) and the outward force is greater than the inward force. Thus, we expect the local maxima in the repulsive force to be located at

$$L_n = n\frac{\pi}{k_{\text{max}}}, \tag{7.8}$$

where $G'(k_{\text{max}}) = 0$; the separation between the force peaks is $\Delta L = \pi/k_{\text{max}}$. In a maritime context, our calculation shows that as long as the separation between ships is $L > \pi/k_{\text{max}} = \pi U^2\sqrt{3/(2\beta)}/g$, the repulsive fluctuation force will keep the ships away from one another. Although quantitative measurement of this oscillatory hydrodynamic fluctuation force remains elusive, an oscillatory force has been observed in the acoustic analogue for which a non-monotonic fluctuation spectrum was produced (Larraza and Denardo, 1998; Larraza et al., 1998).

Anecdotally, in the early 19th Century, the French nautical writer P. C. Causseé published the book "Album of the Mariner" (Causseé, 1836). In it a remark was made about two ships attracted to each other via a swell wave. To resolve this potentially perilous situation, Causseé recommended the lowering of a sloop with a sufficiently strong crew to tow one ship out of reach of the other. Here, we provided a mathematical explanation of the maritime Casimir effect — if the ships are sufficiently far apart from each other, the hydrodynamic fluctuation force actually prevents the ships from colliding.

7.4 General Fluctuation Spectra

Further insight into the general framework can be obtained by applying it to a generic log-normal energy spectrum

$$G(k) = \frac{1}{k\sigma\sqrt{2\pi}} \exp\left(-\frac{1}{2\sigma}(\log k - \mu)^2\right), \tag{7.9}$$

where μ is the mean of the spectrum in wavenumber space and σ is the standard deviation. This form of the spectrum allows us to independently vary the width, as well as the position, of the peak. Figure 7.2 suggests that the period of the oscillating force is controlled by the position of the peak in the energy spectrum, and decreases as the peak is shifted to larger k. This is because the peaks in repulsive force are attained when the wavenumber of one allowed mode equals the peak wavenumber of the spectrum, *viz.*

$$L_n = n\frac{\pi}{k_{\max}}, \tag{7.10}$$

hence the separation between the peaks $\Delta L = \pi/k_{\max}$.

The numerical data in Figure 7.2 suggest that certain features of the force law are universal: The peaks in the fluctuation-induced force $F_{\max} \propto 1/n$, where n is the peak number, and the peak width $\propto n$. Since $n = Lk_{\max}/\pi$, we have $F \sim 1/L$ — an inverse force law. To derive these scalings, we note that any narrow fluctuation spectrum can be approximated by

$$G(k) \approx \begin{cases} G_0 + \frac{G_2}{2}(k - k_{\max})^2, & |k - k_{\max}| < \sqrt{-\frac{2G_0}{G_2}} \\ 0 & \text{otherwise} \end{cases} \tag{7.11}$$

where $G_0 = G(k_{\max})$ and $G_2 = G''(k_{\max})$. In the narrow-peak limit ($w \sim 2\sqrt{-G_0/G_2} \ll \pi/L$, where w is the typical full width at half maximum of the spectrum based on a parabolic approximation), the n^{th} peak in the force is given by

$$F_n \approx \begin{cases} \frac{\pi}{4L}\left[G_0 + \frac{G_2}{2}\left(\frac{n\pi}{L} - k_{\max}\right)^2\right] - \frac{\sqrt{2}G_0}{3}\sqrt{\frac{G_0}{-G_2}}, & \left|\frac{n\pi}{L} - k_{\max}\right| < \left(-\frac{2G_0}{G_2}\right)^{1/2}, \\ -\frac{\sqrt{2}G_0}{3}\sqrt{\frac{G_0}{-G_2}} & \text{otherwise.} \end{cases} \tag{7.12}$$

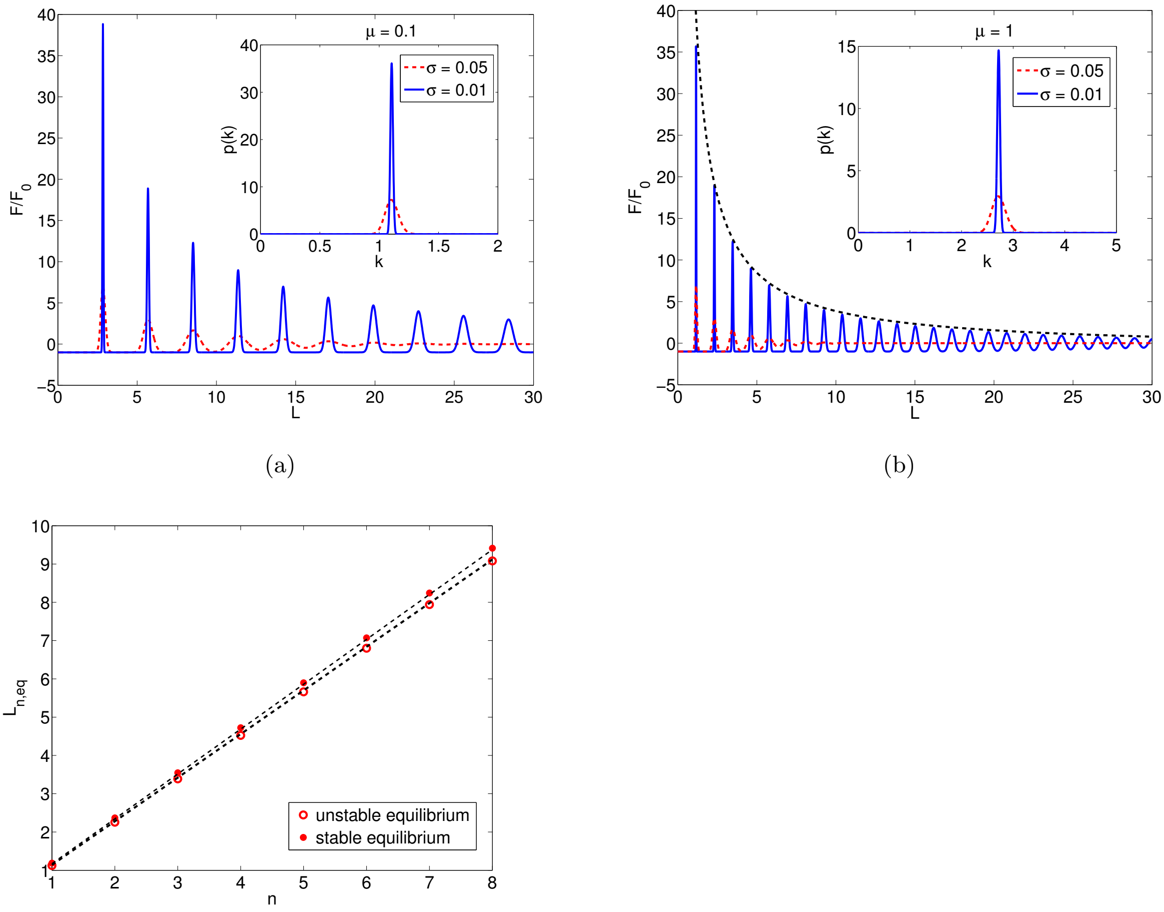

(a)

(b)

(c)

Figure 7.2: *The Casimir force as a function of separation for the log-normal spectrum Equation (7.9). (a)-(b) show how the period and width of the peaks vary with the variance and mean of the energy spectrum. The envelop in (b) shows that the asymptotic approximation for the maximum force, Equation (7.13), agrees with the numerical results. (c) The location of stable and unstable equilibria associated with the* n^{th} *peak. The data points are obtained by finding the roots of (7.7) numerically, and the dotted lines are the asymptotic result (7.16).*

Equation (7.12) shows that the n^{th} maximum, located at $L_n = n\pi/k_{\text{max}}$, has magnitude

$$F_{n,\text{max}} = \frac{G_0\pi}{4L} - \frac{\sqrt{2}G_0}{3}\sqrt{\frac{G_0}{-G_2}} = \frac{G_0 k_{\text{max}}}{4n} - \frac{\sqrt{2}G_0}{3}\sqrt{\frac{G_0}{-G_2}}, \tag{7.13}$$

and thus the maximum force is linear in the inverse plate separation.

The force reaches a minimum when

$$\frac{n\pi}{L} - k_{\text{max}} = (-2G_0/G_2)^{1/2}. \tag{7.14}$$

Writing $L = L_{\text{max}} + l_n = n\pi/k_{\text{max}} + l_n$, where l_n is the half-width of the peak, we obtain

$$l_n = n\pi\left(\frac{1}{\sqrt{-2G_0/G_2} + k_{\text{max}}} - \frac{1}{k_{\text{max}}}\right). \tag{7.15}$$

Therefore the width of the force maxima increases *linearly* with n, and the positions of the n^{th} mechanical equilibria ($F_{\text{fluct}} = 0$) are given by

$$L_{n,eq} = L_n \pm l_n = n\pi\left(\frac{1}{k_{\text{max}}} \pm \frac{1}{\sqrt{-2G_0/G_2} + k_{\text{max}}} \mp \frac{1}{k_{\text{max}}}\right), \tag{7.16}$$

with the positive branch being the stable equilibria, and the negative branch being the unstable equilibria. Equation (7.16) agrees with numerical data (see Figure 7.2c), without any fitting parameters.

7.5 Active Brownian Suspensions

Equations (7.13) and (7.15) predict that the force-displacement curve has peak repulsion $\propto 1/L$ and peak width $\propto n$. These predictions are completely general relying on the peak in the spectrum being sufficiently narrow. They form a phenomenological theory that can be applied to systems where the fluctuation spectrum is not known *a priori* to extract properties of the spectrum.

We illustrate the generality of this approach by considering the simulation results reported by Ni et al. (2015) for self-propelled Brownian hard spheres confined between hard walls. In the simulations the motion of particle i with position $\mathbf{r}_i$ and $\hat{\mathbf{u}}_i$ is described via the overdamped Langevin equation

$$\frac{\mathrm{d}\mathbf{r}_i}{\mathrm{d}t} = \frac{D_0}{k_B T}\Big(- \nabla_i U + f\hat{\mathbf{u}}_i + \boldsymbol{\zeta}_i(t)\Big), \tag{7.17}$$

where the potential energy $U = U(\mathbf{r}_1, \mathbf{r}_2, \cdots, \mathbf{r}_N)$ is the sum of interactions (assumed to be repulsive, short-ranged, Weeks-Chandler-Andersen) between all particle pairs, and D_0 is the short-time self-diffusion coefficient of particle i and is proportional to its inverse diameter $1/\sigma$. A stochastic force with zero mean, $\boldsymbol{\zeta}_i(t)$, describes the collisions with the solvent molecules, and satisfies

$$\left\langle \boldsymbol{\zeta}_i(t) \boldsymbol{\zeta}_j^T(t') \right\rangle = 2(k_B T)^2 \mathbf{1} \delta_{ij}/D_0, \tag{7.18}$$

with $\mathbf{1}$ the identity matrix. The active, self-propulsion of the particle is modelled by a constant force f in the direction $\hat{\mathbf{u}}_i$ at time t, which undergoes free Brownian rotation with a rotational diffusion coefficient $D_r = 3D_0/\sigma$ given by the Stokes-Einstein relation, *i.e.*

$$\hat{\mathbf{u}}_i = (\cos\phi_i \ \sin\phi_i)^T, \quad \left\langle \frac{\mathrm{d}\phi_i(t)}{\mathrm{d}t} \right\rangle = 0, \quad \left\langle \frac{\mathrm{d}\phi_i(t)}{\mathrm{d}t} \frac{\mathrm{d}\phi_j(t)}{\mathrm{d}t} \right\rangle = 2D_r \delta_{ij} \delta(t - t'). \tag{7.19}$$

Experimentally, self-propelled particles can be achieved and steered by various mechanisms, ranging from catalytic reactions of Janus particles (Theurkauff et al., 2012), to laser-heated metal-capped particles (Palacci et al., 2013).

To compute the disjoining pressure for confined active Brownian particles, Ni et al. (2015) simulated a system with two hard slabs immersed in the bath of self-propelled Brownian hard spheres moving according to (7.18)-(7.19), and computed the force exerted by the particles on the slab. They found an oscillatory decay in the disjoining force (Figure 7.3a) that is quantitatively described by our scalings shown in equations (7.13) and (7.15) (Figure 7.3b). In particular, our analysis of their data suggest a spectrum with $k_{\max} = \pi$ and width $\sqrt{-2G_0/G_2} = 0.2$.

Further analytical insights can be obtained by considering the ideal particle limit. In this limit, Ni et al. (2015) observed that the disjoining pressure is attractive and decays monotonically with separation. This can be explained within our framework by noting that the self-propulsion of point-particles can effectively be described by the Langevin equation

$$\frac{\mathrm{d}\mathbf{r}_i}{\mathrm{d}t} = \frac{D_0}{k_B T} \left(\boldsymbol{\eta}_i(t) + \boldsymbol{\zeta}_i(t) \right), \tag{7.20}$$

where $\boldsymbol{\eta}(t)$ is a Gaussian coloured noise satisfying (Farage et al., 2015)

$$\langle \boldsymbol{\eta}_i(t) \rangle = 0, \ \left\langle \boldsymbol{\eta}_i(t) \boldsymbol{\eta}_j^T(t') \right\rangle = \frac{f^2}{3} e^{-2D_r|t-t'|} \mathbf{1} \delta_{ij}. \tag{7.21}$$

In the frequency domain, the fluctuation spectrum $S(\omega)$ is the Fourier transform of the

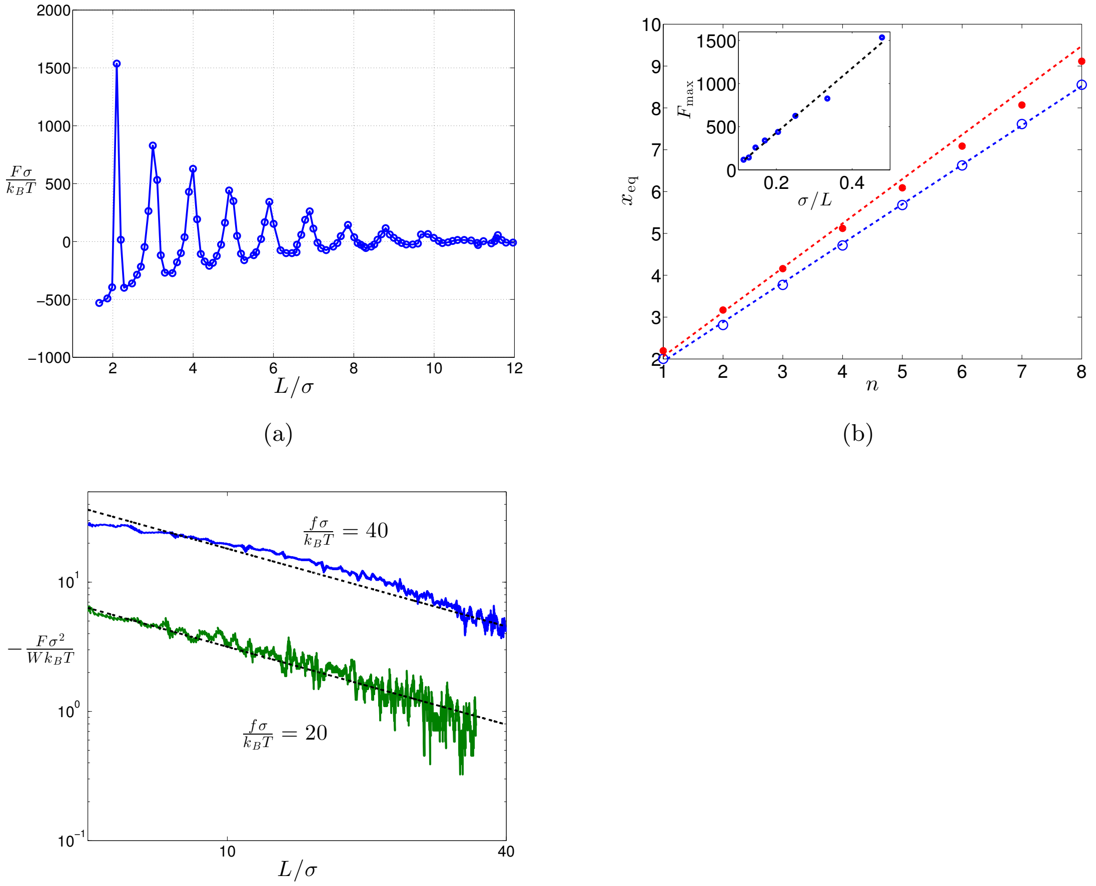

(a)

(b)

(c)

Figure 7.3: *Comparison of our asymptotic results with the simulations of Ni et al. (2015) of a 2D suspension of self-propelled Brownian spheres, confined between hard slabs, which are interacting via the Weeks-Chandler-Anderson potential. In (a) and (b) the packing fraction in the bulk is* $\rho\sigma^2 = 0.4$*, where* σ *is the particle diameter, and the wall length is* $W = 10\sigma$*. Self-propulsion is described via a constant force* $f = 40k_BT/\sigma$ *in the direction* $\hat{\mathbf{u}}_i(t)$ *acting on the* i^{th} *particle. The propulsion direction* $\hat{\mathbf{u}}_i(t)$ *undergoes rotational diffusion with diffusion coefficient* $D_r = 3D_0/\sigma^2$*, where* D_0 *is the translational diffusion coefficient. We note for smaller values of* f *simulated in Ni et al. (2015), the peaks are less pronounced and obscured by numerical noise. (a) The force-displacement curve as presented by Ni et al. (2015). (b) The simulation data agrees with our asymptotic predictions (7.13) and (7.15) with fitted parameters* $G_0 = 4.8\times10^3$ *and* $G_2 = -2.4\times10^5$*. As the peaks are spaced approximately* σ *apart, we take* $k_{\rm max} = \pi$*. The positions of the stable (closed circles) and unstable (open circles) mechanical equilibria (when* $F = 0$*, see Methods) are given by* $x_{\rm eq}$*. The inset shows the force maxima in (a)* $\propto 1/L$ *and agrees with equation (7.13). (c) The function* $A\sigma/L$ *(black dotted line,* c.f.*, Equation (7.23)) can be fitted (using* A*) to simulation data for ideal non-interacting self-propelled ideal point particles with* $F\sigma^2/(Wk_BT) = 40$ *(*$A = 182$*) and* $F\sigma^2/(Wk_BT) = 20$ *(*$A = 31.6$*). Here* $W = 80\sigma$*.*

time-correlation function and is

$$S(\omega) = \frac{4D_r f^2}{3} \frac{1}{4D_r^2 + \omega^2}. \tag{7.22}$$

The Lorentzian noise spectrum of Equation (7.22) deviates from the entropy-maximising white noise. Assuming a linear dispersion relation $\omega(k) = vk$, where v is the characteristic speed of density fluctuations in the system, and substituting Equation (7.22) into Equation (7.7) yields an analytical expression for the force

$$F_{\text{fluct}} = -\frac{\pi f^2}{3v} \left[\frac{v}{2D_r L} + \coth\left(\frac{2D_r L}{v} \right) - 1 \right], \tag{7.23}$$

wherein the large L limit is given by $F_{\text{fluct}} = -\pi f^2/(6D_r L)$. Figure 7.3c shows that the disjoining pressure obtained from simulation $\propto 1/L$. Doubling the activity f increases the prefactor by a factor of 5.6, which is close to the factor of 4 predicted by equation (7.23). Interestingly, it is the coupling between excluded volume interactions and active self-propulsion that gives rise to a non-monotonic spectrum and the oscillatory decay seen in Figure 7.3a.

We note that the $\propto 1/L$ decay in the force means that the degree of correlation in active systems is significantly more pronounced than strongly interacting fluids at equilibrium. For Coulomb fluids considered in Chapter 4, the disjoining pressure between two charged plates decays *exponentially* due to Debye screening, although the Coulomb force between individual ions is inversely proportional to separation. Therefore, interestingly, the degree of screening in active systems is significantly less than its equilibrium counterpart.

7.6 Conclusion

Although there are a plethora of ways to prepare non-equilibrium systems, we suggest that an unifying organising principle resides in their non-trivial energy fluctuation spectrum. By adopting this top-down view, we computed the relationship between the disjoining pressure and the fluctuation spectrum, and verified our approach by considering two seemingly disparate non-equilibrium physical systems: the maritime Casimir effect, which is driven by wind-water interactions, and the forces generated by confined active Brownian particles.

Our framework affords crucial insight into the phenomenology of both driven and active non-equilibrium systems by providing the bridge between microscopic calculations (Solon et al., 2014), measurements of the fluctuation spectra (Chu, 1974) and the varied measurements of Casimir interactions (Lamoreaux, 1997; Munday et al., 2009; Sushkov et al., 2011). Moreover, another form of an “active fluid” can be constructed in a pure system using, for example, a thermally non-equilibrium steady state; temperature fluctuations in such a system have been observed to give rise to long-range Casimir-like behaviour (Kirkpatrick et al., 2013; Aminov et al., 2015). Hence, an intriguing possibility suggested by our analysis is that rather than tuning forces by controlling the nature (e.g., dielectric properties (French et al., 2010)) of the bounding walls, one can envisage actively controlling the fluctuation spectra of the intervening material. Indeed, a natural speculation is that swimmers in biological (engineering) settings could (be designed to) actively control the forces they experience in confined geometries.

Chapter 8

Epilogue

> The real point of honour [for a scientist] is not to be always right. It is to dare to propose new ideas, and then to check them.
>
> *(Pierre-Gilles de Gennes)*

8.1 Synopsis

In this thesis, we have studied the structure of ionic liquids in bulk and in nanoconfinement. We have shown, using a simple thermodynamic model, that despite strong Coulombic interactions, the majority of ions are free rather than being bundled up in ion pairs. This is because the presence of other free ions effectively screens out the electric field around an ion, and renders the ion-ion interaction exponentially decaying. As a result, ionic liquids can be considered to be truly concentrated electrolytes with strong electrostatic correlations.

With the importance of high ion concentration established, we then moved to nanoconfinement. We considered the equilibrium properties of an ionic liquid confined between charged surfaces by developing a 1D Coulomb gas model with hard core exclusion. This model showed that the disjoining pressure decays in an oscillatory manner with increasing surface separation. As expected intuitively, the maxima of these oscillations correspond to discrete "layers" of ions entering the slit from a reservoir. However, the model also highlighted that the disjoining pressure is coupled to the bulk thermodynamics via the fugacity, in qualitative agreement with available experimental data.

Focusing on a single layer ionic liquid confined between two metallic electrodes, we developed a model for charge storage in nanoporous supercapacitors at equilibrium. Our theory challenges the conventional wisdom that a trilemma between increasing capacitance, optimising power delivery, and reducing hysteresis exists. We identified "ionophilicity", the ion-pore affinity at zero applied voltage, as a key parameter, and uncovered a regime of ionophilicity in which the trilemma may be resolved.

Having studied the equilibrium properties of bulk and confined ionic liquids, we studied the behaviour of ionic liquids out of equilibrium. This was done by coarse graining a lattice simple exclusion process, leading to continuum dynamical equations that can be written as a gradient flow with a degenerate mobility function. Solution of these equations predicts charging behaviours that are qualitatively different to those known in electrolytic solutions, but observed in simulations of ionic liquids. Crucially, the accumulated charge in the double layer is no longer a monotonic function of time.

Finally, we studied active, out-of-equilibrium, fluids. Recent molecular dynamics simulations uncovered long-ranged, oscillatory, forces between inclusions immersed in a system of active Brownian particles. While this effect is seemingly analogous to oscillations studied in Chapter 4, we revealed key aspects of this result that are different from the behaviour of ionic liquids at equilibrium. We argue that this behaviour is likely to be generic in such system: the general signature of active and driven non-equilibrium systems is a non-trivial fluctuation spectrum. This physical insight allows us to construct a unifying top-down framework that can describe a plethora of seemingly disparate non-equilibrium phenomena.

8.2 Future Work

Monte Carlo simulations have verified our simple mean-field model of ions confined in a metallic nanopore. The most pressing question resulting from Chapter 5 is experimental effort to quantify and control ionophilicity. This may be done using solid state Nuclear Magnetic Resonance techniques (Wang et al., 2013; Griffin et al., 2014a), which allow one to measure the occupancy of the nanopore at zero applied voltage. Once ionophilicity is quantified, experimental measurement of differential capacitance of nanoporous supercapacitors for ionic liquids with different ionophilicities must be done to verify the predictions of our model.

Molecular dynamics simulations should be done to verify the results of our lattice model for ion transport. Only a handful of simulations to date focus on the dynamic behaviour of ionic liquids. Furthermore, almost all studies use chemically realistic models of ionic liquids, obscuring the key physics with specities (*e.g.* particular chemical functional groups). It would be instructive go to back to the basic physics and systematically study the kinetics of charging for a collection of spherical ions of the same size.

On the theoretical front, a key challenge is to model lubrication and nanotribology with confined ionic liquids. It is uncertain whether the stick-slip dynamics observed in nanoconfined ionic liquids is due to discrete layers of ions slipping past each other, or rather shear-induced partial melting of the system (see Figure 1.3). The answer to this fundamental question will have a large impact on the optimal design of ionic liquids as lubricants. The major theoretical challenge is to incorporate shear into electrokinetic equations. For Brownian hard sphere systems, theoretical models for shear-induced phase transitions have been proposed recently by Brader and Krüger (2011); Aerov and Krüger (2014). The non-equilibrium electrokinetic framework developed here should be extended to elucidate how shear influences the structure of the electrical double layers and thus frictional forces.

Another aspect of non-equilibrium phenomenology is the potential analogy between active colloids and ionic liquids. It is evident from the simulations of Ni et al. (2015) that there is a long-ranged force between active self-propelling colloids that interact only via a hard sphere potential; an oscillatory–decaying disjoining pressure is observed similar to ionic fluids, although the force between active colloids is much longer-ranged than Coulombic systems. We have constructed a top-down approach to describe such phenomenology based on a non-monotonic fluctuation spectrum. While comparison with existing simulation results seems favourable, further simulations/analysis are needed to compute the fluctuation spectra for different microscopic models. In addition, the effect of a long-ranged (say, chemotactic) interaction superposed on top of self-propulsion should be investigated using our formalism.

Bibliography

about.com. http://0.tqn.com/d/chemistry/1/s/q/p/sodium-chloride-3d-ionic.jpg. 2014.

A. A. Aerov and M. Krüger. Driven colloidal suspensions in confinement and density functional theory: Microstructure and wall-slip. *Journal of Chemical Physics*, 140(9): 094701, 2014.

M. T. Alam, M. Islam, T. Okajima, T. Ohsaka, et al. Measurements of differential capacitance in room temperature ionic liquid at mercury, glassy carbon and gold electrode interfaces. *Electrochemistry Communications*, 9(9):2370–2374, 2007a.

M. T. Alam, M. M. Islam, T. Okajima, and T. Ohsaka. Measurements of differential capacitance at mercury/room-temperature ionic liquids interfaces. *Journal of Physical Chemistry C*, 111(49):18326–18333, 2007b.

M. T. Alam, M. M. Islam, T. Okajima, and T. Ohsaka. Capacitance measurements in a series of room-temperature ionic liquids at glassy carbon and gold electrode interfaces. *Journal of Physical Chemistry C*, 112(42):16600–16608, 2008.

C. Aliaga, C. S. Santos, and S. Baldelli. Surface chemistry of room-temperature ionic liquids. *Physical Chemistry Chemical Physics*, 9(28):3683–3700, 2007.

A. Aminov, Y. Kafri, and M. Kardar. Fluctuation induced forces in non-equilibrium (diffusive) dynamics. *arXiv preprint arXiv:1501.01006*, 2015.

P. Attard. Asymptotic analysis of primitive model electrolytes and the electrical double layer. *Physical Review E*, 48(5):3604, 1993.

P. Attard. Electrolytes and the electric double layer. *Advances in Chemical Physics*, 92: 1–160, 1996.

M. Z. Bazant, K. Thornton, and A. Ajdari. Diffuse-charge dynamics in electrochemical systems. *Physical Review E*, 70(2):021506, 2004.

M. Z. Bazant, B. D. Storey, and A. A. Kornyshev. Double layer in ionic liquids: Overscreening versus crowding. *Physical Review Letters*, 106(4):046102, 2011.

T. Beer. *Environmental oceanography*, volume 11. CRC Press, 1996.

M.-D. Bermúdez, A.-E. Jiménez, J. Sanes, and F.-J. Carrión. Ionic liquids as advanced lubricant fluids. *Molecules*, 14(8):2888–2908, 2009.

J. D. Bernal and J. Mason. Packing of spheres: Coordination of randomly packed spheres. *Nature*, (188):910–911, 1960.

B. L. Bhargava, R. Devane, M. L. Klein, and S. Balasubramanian. Nanoscale organization in room temperature ionic liquids: a coarse grained molecular dynamics simulation study. *Soft Matter*, 3(11):1395–1400, 2007.

S. L. Boersma. A maritime analogy of the Casimir effect. *American Journal of Physics*, 64(5):539–540, 1996.

I. Borukhov, D. Andelman, and H. Orland. Steric effects in electrolytes: A modified Poisson-Boltzmann equation. *Physical Review Letters*, 79(3):435, 1997.

I. Borukhov, D. Andelman, and H. Orland. Adsorption of large ions from an electrolyte solution: a modified Poisson-Boltzmann equation. *Electrochimica Acta*, 46(2):221–229, 2000.

I. Bou-Malham and L. Bureau. Nanoconfined ionic liquids: effect of surface charges on flow and molecular layering. *Soft Matter*, 6(17):4062–4065, 2010.

J. M. Brader and M. Krüger. Density profiles of a colloidal liquid at a wall under shear flow. *Molecular Physics*, 109(7-10):1029–1041, 2011.

I. Buttinoni, J. Bialké, F. Kümmel, H. Löwen, C. Bechinger, and T. Speck. Dynamical clustering and phase separation in suspensions of self-propelled colloidal particles. *Physical Review Letters*, 110(23):238301, 2013.

M. E. Cates and J. Tailleur. Motility-induced phase separation. *Annual Review of Condenced Matter Physics*, 6:219, 2015.

P. C. Causseé. *l'Album du Marin*. Charpentier Père, Fils & Cie Editeurs, 1836.

Y.-G. Chen and J. D. Weeks. Local molecular field theory for effective attractions between like charged objects in systems with strong Coulomb interactions. *Proceedings of the National Academy of Sciences*, 103(20):7560–7565, 2006.

J. Chmiola, G. Yushin, Y. Gogotsi, C. Portet, P. Simon, and P. Taberna. Anomalous increase in carbon capacitance at pore sizes less than 1 nanometer. *Science*, 313(5794): 1760–1763, 2006.

U. H. Choi, A. Mittal, T. L. Price Jr, H. W. Gibson, J. Runt, and R. H. Colby. Polymerized ionic liquids with enhanced static dielectric constants. *Macromolecules*, 46(3):1175–1186, 2013.

B. Chu. *Laser Light Scattering.* Elsevier, 1974.

B. Conway. *Electrochemical supercapacitors: scientific fundamentals and technological applications.* Springer, 1999.

G. E. Crooks. Entropy production fluctuation theorem and the nonequilibrium work relation for free energy differences. *Physical Review E*, 60(3):2721, 1999.

C. Daguenet, P. J. Dyson, I. Krossing, A. Oleinikova, J. Slattery, C. Wakai, and H. Weingärtner. Dielectric response of imidazolium-based room-temperature ionic liquids. *Journal of Physical Chemistry B*, 110(25):12682–12688, 2006.

V. Démery, D. S. Dean, T. C. Hammant, R. R. Horgan, and R. Podgornik. The one-dimensional Coulomb lattice fluid capacitor. *Journal of Chemical Physics*, 137(6): 064901, 2012a.

V. Démery, D. S. Dean, T. C. Hammant, R. R. Horgan, and R. Podgornik. Overscreening in a 1d lattice Coulomb gas model of ionic liquids. *Europhysics Letters*, 97(2):28004, 2012b.

B. C. Denardo, J. J. Puda, and A. Larraza. A water wave analog of the Casimir effect. *American Journal of Physics*, 77:1095, 2009.

S. Edwards and A. Lenard. Exact statistical mechanics of a one-dimensional system with Coulomb forces. ii. the method of functional integration. *Journal of Mathematical Physics*, 3(4):778–792, 1962.

M. Eigen and E. Wicke. The thermodynamics of electrolytes at higher concentration. *The Journal of Physical Chemistry*, 58(9):702–714, 1954.

R. Esnouf, A. Smith, and P. Grout. The computer simulation of the metal-molten salt interface. *Philosophical Magazine A*, 58(1):27–35, 1988.

P. Español and H. Löwen. Derivation of dynamical density functional theory using the projection operator technique. *Journal of Chemical Physics*, 131(24):244101, 2009.

R. Evans, J. Henderson, D. Hoyle, A. Parry, and Z. Sabeur. Asymptotic decay of liquid structure: oscillatory liquid-vapour density profiles and the Fisher-Widom line. *Molecular Physics*, 80(4):755–775, 1993.

T. Farage, P. Krinninger, and J. Brader. Effective interactions in active Brownian suspensions. *Physical Review E*, 91(4):042310, 2015.

M. V. Fedorov, N. Georgi, and A. A. Kornyshev. Double layer in ionic liquids: The nature of the camel shape of capacitance. *Electrochemistry Communications*, 12(2):296–299, 2010.

G. Feng and P. Cummings. Supercapacitor capacitance exhibits oscillatory behavior as a function of nanopore size. *Journal of Physical Chemistry Letters*, 2(22):2859, 2011.

K. Fic, G. Lot, and E. Frackowiak. Electrochemical properties of supercapacitors operating in aqueous electrolyte with surfactants. *Electrochimica Acta*, 55:7484, 2010.

K. Fic, G. Lot, and E. Frackowiak. Effect of surfactants on capacitance properties of carbon electrodes. *Electrochimica Acta*, 60:206, 2011.

Y. Fily and M. C. Marchetti. Athermal phase separation of self-propelled particles with no alignment. *Physical Review Letters*, 108(23):235702, 2012.

M. E. Fisher and Y. Levin. Criticality in ionic fluids: Debye-H́uckel theory, Bjerrum, and beyond. *Physical Review Letters*, 71(23):3826, 1993.

M. E. Fisher and B. Widom. Decay of correlations in linear systems. *Journal of Chemical Physics*, 50(9):3756–3772, 1969.

R. H. Fowler and E. A. Guggenheim. *Statistical Thermodynamics*. Cambridge University Press, 1949.

E. Frackowiak, Q. Abbas, and F. Béguin. Carbon/carbon supercapacitors. *Journal of Energy Chemistry*, 22(2):226–240, 2013.

R. H. French, V. A. Parsegian, R. Podgornik, R. F. Rajter, A. Jagota, J. Luo, D. Asthagiri, M. K. Chaudhury, Y. M. Chiang, S. Granick, et al. Long range interactions in nanoscale science. *Reviews of Modern Physics*, 82(2):1887, 2010.

T. Fujimoto and K. Awaga. Electric-double-layer field-effect transistors with ionic liquids. *Physical Chemistry Chemical Physics*, 15(23):8983–9006, 2013.

K. Fumino, A. Wulf, and R. Ludwig. The cation–anion interaction in ionic liquids probed by far-infrared spectroscopy. *Angewandte Chemie International Edition*, 47(20):3830–3834, 2008.

M. A. Gebbie, M. Valtiner, X. Banquy, E. T. Fox, W. A. Henderson, and J. N. Israelachvili. Ionic liquids behave as dilute electrolyte solutions. *Proceedings of the National Academy of Sciences*, 110(24):9674–9679, 2013a.

M. A. Gebbie, M. Valtiner, X. Banquy, W. A. Henderson, and J. N. Israelachvili. Reply to perkin et al.: Experimental observations demonstrate that ionic liquids form both bound (Stern) and diffuse electric double layers. *Proceedings of the National Academy of Sciences*, 110(44):E4122–E4122, 2013b.

M. A. Gebbie, H. A. Dobbs, M. Valtiner, and J. N. Israelachvili. Long-range electrostatic screening in ionic liquids. *Proceedings of the National Academy of Sciences*, page 201508366, 2015.

G. Giacomin and J. L. Lebowitz. Exact macroscopic description of phase segregation in model alloys with long range interactions. *Physical Review Letters*, 76(7):1094, 1996.

G. Giacomin and J. L. Lebowitz. Phase segregation dynamics in particle systems with long range interactions. i. macroscopic limits. *Journal of Statistical Physics*, 87(1-2): 37–61, 1997.

G. Giacomin and J. L. Lebowitz. Phase segregation dynamics in particle systems with long range interactions ii: Interface motion. *SIAM Journal on Applied Mathematics*, 58 (6):1707–1729, 1998.

J.-F. Gouyet. Atomic mobility and spinodal-decomposition dynamics in lattice gases. simple discrete models. *Europhysics Letters*, 21(3):335, 1993.

J.-F. Gouyet, M. Plapp, W. Dieterich, and P. Maass. Description of far-from-equilibrium processes by mean-field lattice gas models. *Advances in Physics*, 52(6):523–638, 2003.

J. M. Griffin, A. C. Forse, H. Wang, N. M. Trease, P.-L. Taberna, P. Simon, and C. P. Grey. Ion counting in supercapacitor electrodes using NMR spectroscopy. *Faraday Discussions*, 2014a.

J. M. Griffin, A. C. Forse, H. Wang, N. M. Trease, P.-L. Taberna, P. Simon, and C. P. Grey. Ion counting in supercapacitor electrodes using NMR spectroscopy. *Faraday Discussions*, 176:49–68, 2014b. doi: 10.1039/C4FD00138A.

J. M. Griffin, A. C. Forse, W.-Y. Tsai, P.-L. Taberna, P. Simon, and C. P. Grey. In situ NMR and electrochemical quartz crystal microbalance measurements reveal the structure of the electric double-layer in supercapacitor electrodes. *Nature Materials*, 2015. Article ASAP.

Guardian. http://static.guim.co.uk/sys-images/observer/pix/pictures/2012/2/8/1328722835154/rock-salt-007.jpg. 2014.

J. P. Hallett and T. Welton. Room-temperature ionic liquids: solvents for synthesis and catalysis. 2. *Chemical Reviews*, 111(5):3508–3576, 2011.

P. Hänggi, P. Talkner, and M. Borkovec. Reaction-rate theory: fifty years after Kramers. *Reviews of Modern Physics*, 62(2):251, 1990.

J.-P. Hansen and J. R. MacDonald. *Theory of simple liquids*. Elsevier, 4th edition, 2014.

M. Hantel, D. Weingarth, and R. Kötz. Parameters determining dimensional changes of porous carbons during capacitive charging. *Carbon*, 69:275–286, 2014.

R. Hayes, S. Z. El Abedin, and R. Atkin. Pronounced structure in confined aprotic room-temperature ionic liquids. *Journal of Physical Chemistry B*, 113(20):7049–7052, 2009.

E. Helfand, H. Frisch, and J. Lebowitz. Theory of the two-and one-dimensional rigid sphere fluids. *Journal of Chemical Physics*, 34(3):1037–1042, 1961.

W. Helfrich and R.-M. Servuss. Undulations, steric interaction and cohesion of fluid membranes. *Il Nuovo Cimento D*, 3(1):137–151, 1984.

P. Holoborodko. Smooth noise robust differentiators. http://www.holoborodko.com/pavel/numerical-methods/numerical-derivative/smooth-low-noise-differentiators/, 2008.

M. Holovko. Concept of ion association in the theory of electrolyte solutions. In *Ionic Soft Matter: Modern Trends in Theory and Applications*, pages 45–81. Springer, 2005.

Z. Hu, J. Vatamanu, O. Borodin, and D. Bedrov. A molecular dynamics simulation study of the electric double layer and capacitance of [BMIM][PF6] and [BMIM][BF4] room temperature ionic liquids near charged surfaces. *Physical Chemistry Chemical Physics*, 15:14234, 2013.

M.-M. Huang, Y. Jiang, P. Sasisanker, G. W. Driver, and H. Weinga rtner. Static relative dielectric permittivities of ionic liquids at 25 ° C. *Journal of Chemical and Engineering Data*, 56(4):1494–1499, 2011.

P. A. Hunt, I. R. Gould, and B. Kirchner. The structure of imidazolium-based ionic liquids: Insights from ion-pair interactions. *Australian Journal of Chemistry*, 60(1):9–14, 2007.

M. M. Islam, M. T. Alam, and T. Ohsaka. Electrical double-layer structure in ionic liquids: a corroboration of the theoretical model by experimental results. *Journal of Physical Chemistry C*, 112(42):16568–16574, 2008.

C. Jarzynski. Nonequilibrium equality for free energy differences. *Physical Review Letters*, 78(14):2690, 1997.

D. Jiang and J. Wu. Unusual effects of solvent polarity on capacitance for organic electrolytes in a nanoporous electrode. *Nanoscale*, 2014. doi: 10.1039/c4nr00046c.

D. Jiang, Z. Jin, and J. Wu. Oscillation of capacitance inside nanopores. *Nano Letters*, 11(12):5373, 2011.

J. Jiang, D. Cao, D.-e. Jiang, and J. Wu. Kinetic charging inversion in ionic-liquid electric double layers. *Journal of Physical Chemistry Letters*, 2014a.

J. Jiang, D. Cao, D.-e. Jiang, and J. Wu. Time-dependent density functional theory for ion diffusion in electrochemical systems. *Journal of Physics: Condensed Matter*, 26(28): 284102, 2014b.

X. Jiang, J. Huang, H. Zhao, B. G. Sumpter, and R. Qiao. Dynamics of electrical double layer formation in room-temperature ionic liquids under constant-current charging conditions. *Journal of Physics: Condensed Matter*, 26(28):284109, 2014c.

J. F. Jover, R. Lugo, H. Toulhoat, P. Simon, and T. De Bruin. Screening methodology for the efficient pairing of ionic liquids and carbonaceous electrodes applied to electric energy storage. *Journal of Physical Chemistry C*, 118(2):864–872, 2014.

F. Kaasik, T. Tamm, M. Hantel, E. Perre, A. Aabloo, E. Lust, M. Bazant, and V. Presser. Anisometric charge dependent swelling of porous carbon in an ionic liquid. *Electrochemistry Communications*, 34:196–199, 2013.

M. Kardar. *Statistical physics of particles.* Cambridge University Press, 2007.

M. S. Kilic, M. Z. Bazant, and A. Ajdari. Steric effects in the dynamics of electrolytes at large applied voltages. ii. modified Poisson-Nernst-Planck equations. *Physical Review E*, 75(2):021503, 2007.

T. Kirkpatrick, J. O. de Zárate, and J. Sengers. Giant Casimir effect in fluids in nonequilibrium steady states. *Physical Review Letters*, 110(23):235902, 2013.

K. Kiyohara, T. Sugino, and K. Asaka. Phase transition in porous electrodes. *Journal of Chemical Physics*, 134:154710, 2011.

K. Kiyohara, H. Shioyama, T. Sugino, and K. Asaka. Phase transition in porous electrodes. ii. effect of asymmetry in the ion size. *Journal of Chemical Physics*, 136:094701, 2012.

K. Kiyohara, H. Shioyama, T. Sugino, K. Asaka, Y. Soneda, K. Imoto, and M. Kodama. Phase transition in porous electrodes. iii. for the case of a two component electrolyte. *Journal of Chemical Physics*, 138(23):234704, 2013.

S. Kondrat and A. Kornyshev. Superionic state in double-layer capacitors with nanoporous electrodes. *Journal of Physics: Condensed Matter*, 23:022201, 2011.

S. Kondrat and A. Kornyshev. Charging dynamics and optimization of nano-porous supercapacitors. *Journal of Physical Chemistry C*, 117:12399–12406, 2013.

S. Kondrat, N. Georgi, M. Fedorov, and A. Kornyshev. A superionic state in nano-porous double-layer capacitors: insights from monte carlo simulations. *Physical Chemistry Chemical Physics*, 13(23):11359–11366, 2011.

S. Kondrat, P. Wu, R. Qiao, and A. A. Kornyshev. Accelerating charging dynamics in subnanometre pores. *Nature Materials*, 13:387–393, 2014.

A. A. Kornyshev. Double-layer in ionic liquids: paradigm change? *Journal of Physical Chemistry B*, 111(20):5545–5557, 2007.

I. Krossing, J. M. Slattery, C. Daguenet, P. J. Dyson, A. Oleinikova, and H. Weingärtner. Why are ionic liquids liquid? a simple explanation based on lattice and solvation energies. *Journal of the American Chemical Society*, 128(41):13427–13434, 2006.

S. K. Lamoreaux. Demonstration of the Casimir force in the 0.6 to 6 μ m range. *Physical Review Letters*, 78(1):5, 1997.

S. Lamperski and J. Kłos. Grand canonical monte carlo investigations of electrical double layer in molten salts. *Journal of Chemical Physics*, 129(16):164503, 2008.

O. J. Lanning and P. A. Madden. Screening at a charged surface by a molten salt. *The Journal of Physical Chemistry B*, 108(30):11069–11072, 2004.

C. Largeot, C. Portet, J. Chmiola, P. Taberna, Y. Gogotsi, and P. Simon. Relation between the ion size and pore size for an electric double-layer capacitor. *Journal of the American Chemical Society*, 130(9):2730–2731, 2008.

A. Larraza and B. Denardo. An acoustic Casimir effect. *Physics Letters A*, 248(2):151–155, 1998.

A. Larraza, C. D. Holmes, R. T. Susbilla, and B. Denardo. The force between two parallel rigid plates due to the radiation pressure of broadband noise: An acoustic Casimir effect. *Journal of the Acoustical Society of America*, 103(5):2267–2272, 1998.

A. A. Lee, S. Kondrat, and A. A. Kornyshev. Single-file charge storage in conducting nanopores. *Physical Review Letters*, 113(4):048701, 2014a.

A. A. Lee, S. Kondrat, G. Oshanin, and A. A. Kornyshev. Charging dynamics of supercapacitors with narrow cylindrical nanopores. *Nanotechnology*, 25:315401, 2014b. doi: 10.1088/0957-4484/25/31/315401.

A. A. Lee, D. Vella, S. Perkin, and A. Goriely. Unravelling nanoconfined films of ionic liquids. *Journal of Chemical Physics*, 141(9):094904, 2014c.

A. A. Lee, S. Kondrat, D. Vella, and A. Goriely. Dynamics of ion transport in ionic liquids. *Physical Review Letters*, 115(10):106101, 2015a.

A. A. Lee, D. Vella, S. Perkin, and A. Goriely. Are room temperature ionic liquids dilute electrolytes? *Journal of Physical Chemistry Letters*, 6:159–163, 2015b.

A. Lenard. Exact statistical mechanics of a one-dimensional system with Coulomb forces. *Journal of Mathematical Physics*, 2(5):682–693, 1961.

I. Leontyev and A. Stuchebrukhov. Electronic continuum model for molecular dynamics simulations. *Journal of Chemical Physics*, 130(8):085102, 2009.

R. Leote de Carvalho and R. Evans. The decay of correlations in ionic fluids. *Molecular Physics*, 83(4):619–654, 1994.

Y. Levin and M. E. Fisher. Criticality in the hard-sphere ionic fluid. *Physica A: Statistical Mechanics and its Applications*, 225(2):164–220, 1996.

R. Lin, P. Huang, J. Segalini, C. Largeot, P.-L. Taberna, J. Chmiola, Y. Gogotsi, and P. Simon. Solvent effect on the ion adsorption from ionic liquid electrolyte into sub-nanometer carbon pores. *Electrochimica Acta*, 54(27):7025–7032, 2009.

R. Lin, P.-L. Taberna, S. Fantini, V. Presser, C. R. Pérez, F. Malbosc, N. L. Rupesinghe, K. B. K. Teo, Y. Gogotsi, and P. Simon. Capacitive energy storage from 50 to 100 ^{o}c using an ionic liquid electrolyte. *Journal Physical Chemistry Letters*, 2:2396–2401, 2011.

V. Lockett, R. Sedev, J. Ralston, M. Horne, and T. Rodopoulos. Differential capacitance of the electrical double layer in imidazolium-based ionic liquids: Influence of potential, cation size, and temperature. *Journal of Physical Chemistry C*, 112(19):7486–7495, 2008.

M. Lu, F. Beguin, and E. Frackowiak. *Supercapacitors: Materials, Systems and Applications*. John Wiley & Sons, 2013.

R. Lynden-Bell. Screening of pairs of ions dissolved in ionic liquids. *Physical Chemistry Chemical Physics*, 12(8):1733–1740, 2010.

U. M. B. Marconi and P. Tarazona. Dynamic density functional theory of fluids. *Journal of Chemical Physics*, 110(16):8032–8044, 1999.

U. M. B. Marconi and P. Tarazona. Dynamic density functional theory of fluids. *Journal of Physics: Condensed Matter*, 12(8A):A413, 2000.

M. G. Martin. MCCCS towhee: a tool for Monte Carlo molecular simulation. *Molecular Simulation*, 39(14-15):1212–1222, 2013.

P. Mazur and S. R. de Groot. *Non-equilibrium Thermodynamics*. North-Holland, 1963.

C. Merlet, B. Rotenberg, P. A. Madden, P.-L. Taberna, P. Simon, Y. Gogotsi, and M. Salanne. On the molecular origin of supercapacitance in nanoporous carbon electrodes. *Nature Materials*, 11(4):306–310, 2012.

C. Merlet, C. Péan, B. Rotenberg, P. A. Madden, B. Daffos, P.-L. Taberna, P. Simon, and M. Salanne. Highly confined ions store charge more efficiently in supercapacitors. *Nature Communications*, 4, 2013a.

C. Merlet, B. Rotenberg, P. A. Madden, and M. Salanne. Computer simulations of ionic liquids at electrochemical interfaces. *Physical Chemistry Chemical Physics*, 15(38):15781–15792, 2013b.

M. Mezger, H. Schröder, H. Reichert, S. Schramm, J. S. Okasinski, S. Schöder, V. Honkimäki, M. Deutsch, B. M. Ocko, J. Ralston, M. Rohwerder, M. Stratmann, and H. Dosch. Molecular layering of fluorinated ionic liquids at a charged sapphire (0001) surface. *Science*, 322(5900):424–428, 2008.

J. Miller and P. Simon. Electrochemical capacitors for energy management. *Science*, 321 (5889):651–652, 2008.

I. Minami. Ionic liquids in tribology. *Molecules*, 14(6):2286–2305, 2009.

I. Minami, H. Kamimura, and S. Mori. Thermo-oxidative stability of ionic liquids as lubricating fluids. *Journal of Synthetic Lubrication*, 24(3):135–147, 2007.

J. N. Munday, F. Capasso, and V. A. Parsegian. Measured long-range repulsive Casimir–lifshitz forces. *Nature*, 457(7226):170–173, 2009.

A. Naji, M. Kanduč, J. Forsman, and R. Podgornik. Perspective: Coulomb fluids: Weak coupling, strong coupling, in between and beyond. *Journal of Chemical Physics*, 139 (15):150901, 2013.

K. Nakamura and T. Shikata. Systematic dielectric and NMR study of the ionic liquid 1-alkyl-3-methyl imidazolium. *ChemPhysChem*, 11(1):285–294, 2010.

W. Nernst. *Zeitschrift fur Physikalische Chemie*, 2:613, 1888.

W. Nernst. *Zeitschrift fur Physikalische Chemie*, 1889.

R. Netz. Electrostatistics of counter-ions at and between planar charged walls: from Poisson-Boltzmann to the strong-coupling theory. *European Physical Journal E*, 5(1): 557–574, 2001.

R. Netz and H. Orland. Variational charge renormalization in charged systems. *European Physical Journal E*, 11(3):301–311, 2003.

R. Ni, M. A. C. Stuart, and P. G. Bolhuis. Tunable long range forces mediated by self-propelled colloidal hard spheres. *Physical Review Letters*, 114(1):018302, 2015.

A. Noda, K. Hayamizu, and M. Watanabe. Pulsed-gradient spin-echo 1H and 19F NMR ionic diffusion coefficient, viscosity, and ionic conductivity of non-chloroaluminate room-temperature ionic liquids. *Journal of Physical Chemistry B*, 105(20):4603–4610, 2001.

H. Nyquist. Thermal agitation of electric charge in conductors. *Physical Reviews*, 32(1): 110–113, 1928.

H. Ohno. *Electrochemical aspects of ionic liquids.* John Wiley & Sons, 2011.

M. Oliveira, M. Dominguez-Pérez, M. Freire, F. Llovell, O. Cabeza, J. Lopes-da Silva, L. Vega, and J. Coutinho. Surface tension of binary mixtures of 1-alkyl-3-methylimidazolium bis (trifluoromethylsulfonyl) imide ionic liquids: experimental measurements and soft-saft modeling. *Journal of Physical Chemistry B*, 116(40):12133–12141, 2012.

L. Onsager. Electric moments of molecules in liquids. *Journal of the American Chemical Society*, 58(8):1486–1493, 1936.

J. Palacci, S. Sacanna, A. P. Steinberg, D. J. Pine, and P. M. Chaikin. Living crystals of light-activated colloidal surfers. *Science*, 339(6122):936–940, 2013.

C. Péan, C. Merlet, B. Rotenberg, P. A. Madden, P.-L. Taberna, B. Daffos, M. Salanne, and P. Simon. On the dynamics of charging in nanoporous carbon-based supercapacitors. *ACS Nano*, 8(2):1576, 2014.

S. Perkin, T. Albrecht, and J. Klein. Layering and shear properties of an ionic liquid, 1-ethyl-3-methylimidazolium ethylsulfate, confined to nano-films between mica surfaces. *Physical Chemistry Chemical Physics*, 12(6):1243–1247, 2010.

S. Perkin, L. Crowhurst, H. Niedermeyer, T. Welton, A. M. Smith, and N. N. Gosvami. Self-assembly in the electrical double layer of ionic liquids. *Chemical Communications*, 47(23):6572–6574, 2011.

S. Perkin, M. Salanne, P. Madden, and R. Lynden-Bell. Is a Stern and diffuse layer model appropriate to ionic liquids at surfaces? *Proceedings of the National Academy of Sciences*, 110(44):E4121–E4121, 2013.

E. Petrishcheva and R. Abart. Exsolution by spinodal decomposition in multicomponent mineral solutions. *Acta Materialia*, 60(15):5481–5493, 2012.

W. J. Pierson and L. Moskowitz. A proposed spectral form for fully developed wind seas based on the similarity theory of S. A. Kitaigorodskii. *Journal of Geophysical Research*, 69(24):5181–5190, 1964.

O. Pizio, S. Sokołowski, and Z. Sokołowska. Electric double layer capacitance of restricted primitive model for an ionic fluid in slit-like nanopores: A density functional approach. *Journal of Chemical Physics*, 137:234705, 2012.

M. Planck. *Annalen der Physik und Chemie*, 39:161, 1890.

M. Plapp and J.-F. Gouyet. Surface modes and ordered patterns during spinodal decomposition of an abv model alloy. *Physical Review Letters*, 78(26):4970, 1997.

M. Plapp and J.-F. Gouyet. Spinodal decomposition of an abv model alloy: Patterns at unstable surfaces. *European Physical Journal B*, 9(2):267–282, 1999.

R. Qiao, V. Meunier, and B. Sumpter. Voltage dependent charge storage modes and capacity in subnanometer pores. *Journal of Physical Chemistry Letters*, 3:1732–1737, 2012.

J. Qu, P. J. Blau, S. Dai, H. Luo, H. M. Meyer III, and J. J. Truhan. Tribological characteristics of aluminum alloys sliding against steel lubricated by ammonium and imidazolium ionic liquids. *Wear*, 267(5):1226–1231, 2009.

E. Raymundo-Piñero, K. Kierczek, J. Machnikowski, and F. Béguin. Relationship between the nanoporous texture of activated carbons and their capacitance properties in different electrolytes. *Carbon*, 44:2498–2507, 2006.

G. S. Redner, M. F. Hagan, and A. Baskaran. Structure and dynamics of a phase-separating active colloidal fluid. *Physical Review Letters*, 110(5):055701, 2013.

P. Richetti, P. Kékicheff, J. Parker, and B. Ninham. Measurement of the interactions between membranes in a stack. *Nature*, 346(6281):252–254, 1990.

F. W. Richey, C. Tran, V. Kalra, , and Y. A. Elabd. Ionic liquid dynamics in nanoporous carbon nanofibers in supercapacitors measured with *in operando* infrared spectroelectrochemistry. *Journal of Physical Chemistry C*, 118:21846, 2014.

R. A. Robinson and R. H. Stokes. *Electrolyte solutions.* Dover Publications, 2002.

C. C. Rochester, A. A. Lee, G. Pruessner, and A. A. Kornyshev. Interionic interactions in conducting nanoconfinement. *ChemPhysChem*, 14(18):4121–4125, 2013.

S. Saha, R. Golestanian, and S. Ramaswamy. Clusters, asters, and collective oscillations in chemotactic colloids. *Physical Review E*, 89(6):062316, 2014.

C. D. Santangelo. Computing counterion densities at intermediate coupling. *Physical Review E*, 73(4):041512, 2006.

M. Schmidt and H. Löwen. Freezing between two and three dimensions. *Physical Review Letters*, 76(24):4552, 1996.

M. Schmidt and H. Löwen. Phase diagram of hard spheres confined between two parallel plates. *Physical Review E*, 55(6):7228, 1997.

C. Schröder. Comparing reduced partial charge models with polarizable simulations of ionic liquids. *Physical Chemistry Chemical Physics*, 14(9):3089–3102, 2012.

C. Schröder, J. Hunger, A. Stoppa, R. Buchner, and O. Steinhauser. On the collective network of ionic liquid/water mixtures. ii. decomposition and interpretation of dielectric spectra. *Journal of Chemical Physics*, 129(18):184501, 2008.

W. Schröer. Generalization of the Kirkwood-Fr'́ohlich theory of dielectric polarization for ionic fluids. *Journal of Molecular Liquids*, 92(1):67–76, 2001.

W. Schröer. On the chemical and the physical approaches to ion association. *Journal of Molecular Liquids*, 164(1):3–10, 2011.

P. Simon and Y. Gogotsi. Materials for electrochemical capacitors. *Nature Materials*, 7 (11):845–854, 2008.

P. Simon and Y. Gogotsi. Capacitive energy storage in nanostructured carbon–electrolyte systems. *Accounts of Chemical Research*, 46(5):1094, 2013.

B. Skinner, T. Chen, M. S. Loth, and B. I. Shklovskii. Theory of volumetric capacitance of an electric double-layer supercapacitor. *Physical Review E*, 83(5):056102, 2011.

J. M. Slattery, C. Daguenet, P. J. Dyson, T. J. Schubert, and I. Krossing. How to predict the physical properties of ionic liquids: A volume-based approach. *Angewandte Chemie International Edition*, 119(28):5480–5484, 2007.

A. M. Smith, K. R. Lovelock, N. N. Gosvami, T. Welton, and S. Perkin. Quantized friction across ionic liquid thin films. *Physical Chemistry Chemical Physics*, 15(37):15317–15320, 2013.

A. P. Solon, Y. Fily, A. Baskaran, M. E. Cates, Y. Kafri, M. Kardar, and J. Tailleur. What is the pressure of an active particle fluid? *arXiv:1412.3952*, 2014.

P. Somasundaran. *Encyclopedia of surface and colloid science*, volume 1. CRC press, 2006.

R. Soto and R. Golestanian. Self-assembly of catalytically active colloidal molecules: tailoring activity through surface chemistry. *Physical Review Letters*, 112(6):068301, 2014.

H. Spohn. *Large scale dynamics of interacting particles*, volume 825. Springer, 1991.

J. Stenhammar, A. Tiribocchi, R. J. Allen, D. Marenduzzo, and M. E. Cates. Continuum theory of phase separation kinetics for active Brownian particles. *Physical Review Letters*, 111(14):145702, 2013.

A. Stoppa, R. Buchner, and G. Hefter. How ideal are binary mixtures of room-temperature ionic liquids? *Journal of Molecular Liquids*, 153(1):46–51, 2010.

B. D. Storey and M. Z. Bazant. Effects of electrostatic correlations on electrokinetic phenomena. *Physical Review E*, 86(5):056303, 2012.

A. Sushkov, W. Kim, D. Dalvit, and S. Lamoreaux. Observation of the thermal Casimir force. *Nature Physics*, 7(3):230–233, 2011.

Y. B. Tan and J.-M. Lee. Graphene for supercapacitor applications. *Journal of Materials Chemistry A*, 1(47):14814–14843, 2013.

I. Theurkauff, C. Cottin-Bizonne, J. Palacci, C. Ybert, and L. Bocquet. Dynamic clustering in active colloidal suspensions with chemical signaling. *Physical Review Letters*, 108(26): 268303, 2012.

H. Tokuda, K. Hayamizu, K. Ishii, M. A. B. H. Susan, and M. Watanabe. Physicochemical properties and structures of room temperature ionic liquids. 2. variation of alkyl chain length in imidazolium cation. *Journal of Physical Chemistry B*, 109(13):6103–6110, 2005.

L. Tonks. The complete equation of state of one, two and three-dimensional gases of hard elastic spheres. *Physical Review*, 50(10):955, 1936.

A. Triolo, O. Russina, H.-J. Bleif, and E. Di Cola. Nanoscale segregation in room temperature ionic liquids. *Journal of Physical Chemistry B*, 111(18):4641–4644, 2007.

M. Trulsson, J. Algotsson, J. Forsman, and C. E. Woodward. Differential capacitance of room temperature ionic liquids: the role of dispersion forces. *Journal of Physical Chemistry Letters*, 1(8):1191–1195, 2010.

K. Ueno, S. Nakamura, H. Shimotani, A. Ohtomo, N. Kimura, T. Nojima, H. Aoki, Y. Iwasa, and M. Kawasaki. Electric-field-induced superconductivity in an insulator. *Nature Materials*, 7(11):855–858, 2008.

B. Uhl, F. Buchner, D. Alwast, N. Wagner, and R. J. Behm. Adsorption of the ionic liquid [BMP][TFSA] on Au (111) and Ag (111): substrate effects on the structure formation investigated by STM. *Beilstein Journal of Nanotechnology*, 4(1):903–918, 2013.

J. Vatamanu, O. Borodin, and G. D. Smith. Molecular insights into the potential and temperature dependences of the differential capacitance of a room-temperature ionic liquid at graphite electrodes. *Journal of the American Chemical Society*, 132(42):14825–14833, 2010.

J. Vatamanu, Z. Hu, D. Bedrov, C. Perez, and Y. Gogotsi. Increasing energy storage in electrochemical capacitors with ionic liquid electrolytes and nanostructured carbon electrodes. *Journal of Physical Chemistry Letters*, 4(17):2829–2837, 2013.

J. Vatamanu, M. Vatamanu, and D. Bedrov. Non-Faradic energy storage by room temperature ionic liquids in nanoporous electrodes. *ACS Nano*, 2015. Article ASAP.

P. Walden. *Bulletin of the St Petersburg Academy of Science*, page 405, 1914.

H. Wang, G. Gurau, and R. D. Rogers. Ionic liquid processing of cellulose. *Chemical Society Reviews*, 41(4):1519–1537, 2012.

H. Wang, A. C. Forse, J. M. Griffin, N. M. Trease, L. Trognko, P.-L. Taberna, P. Simon, and C. P. Grey. In situ NMR spectroscopy of supercapacitors: insight into the charge storage mechanism. *Journal of the American Chemical Society*, 135(50):18968–18980, 2013.

H. Weingartner. The static dielectric constant of ionic liquids. *Zeitschrift fur Physikalische Chemie*, 220(10-11):1395–1406, 2006.

H. Weingärtner. Understanding ionic liquids at the molecular level: facts, problems, and controversies. *Angewandte Chemie International Edition*, 47(4):654–670, 2008.

H. Weingärtner. The static dielectric permittivity of ionic liquids. *Journal of Molecular Liquids*, 2013.

T. Welton. Room-temperature ionic liquids. solvents for synthesis and catalysis. *Chemical Reviews*, 99(8):2071–2084, 1999.

C. Wessells, R. Ruffo, R. A. Huggins, and Y. Cui. Investigations of the electrochemical stability of aqueous electrolytes for lithium battery applications. *Electrochemical and Solid-state Letters*, 13(5):A59–A61, 2010.

Wikipedia. http://commons.wikimedia.org/wiki/file:p1010480-1s.jpg. 2014.

H. W. Woolley. The representation of gas properties in terms of molecular clusters. *Journal of Chemical Physics*, 21(2):236–241, 1953.

P. Wu, J. Huang, V. Meunier, B. Sumpter, and R. Qiao. Complex capacitance scaling in ionic liquids-filled nanopores. *ACS Nano*, 5(11):9044, 2011.

D. Xiao, L. G. Hines Jr, S. Li, R. A. Bartsch, E. L. Quitevis, O. Russina, and A. Triolo. Effect of cation symmetry and alkyl chain length on the structure and intermolecular dynamics of 1, 3-dialkylimidazolium bis (trifluoromethanesulfonyl) amide ionic liquids. *Journal of Physical Chemistry B*, 113(18):6426–6433, 2009.

A. Yochelis. Spatial structure of electrical diffuse layers in highly concentrated electrolytes: A modified Poisson-Nernst-Planck approach. *Journal of Physical Chemistry C*, 118(11): 5716–5724, 2014a.

A. Yochelis. Transition from non-monotonic to monotonic electrical diffuse layers: impact of confinement on ionic liquids. *Physical Chemistry Chemical Physics*, 16(7):2836–2841, 2014b.

H. Yu and W. F. van Gunsteren. Accounting for polarization in molecular simulation. *Computer Physics Communications*, 172(2):69–85, 2005.

S. Zhang, X. Lu, Q. Zhou, X. Li, X. Zhang, and S. Li. *Ionic Liquids: Physicochemical Properties*. Elsevier, 2009.

X. Zhang, X. Zhang, H. Dong, Z. Zhao, S. Zhang, and Y. Huang. Carbon capture with ionic liquids: overview and progress. *Energy and Environmental Science*, 5(5):6668–6681, 2012.

H. Zhao. Diffuse-charge dynamics of ionic liquids in electrochemical systems. *Physical Review E*, 84(5):051504, 2011.

R. Zwanzig. *Nonequilibrium Statistical Mechanics*. Oxford University Press, 2001.